Title
Nanoscale Spatial Organization of Prokaryotic Cells Studied by Super-Resolution Optical Microscopy

Author
McEvoy, Andrea Lynn

Publication Date
2012

Peer reviewed|Thesis/dissertation

Nanoscale Spatial Organization of Prokaryotic Cells Studied by Super-Resolution Optical Microscopy

by

Andrea Lynn McEvoy

A dissertation submitted in partial satisfaction of the

requirements for the degree of

Doctor of Philosophy

in

Biophysics

in the

Graduate Division

of the

University of California, Berkeley

Committee in charge:

Professor Jan T. Liphardt, Chair
Professor Han Lim
Professor Daniel Fletcher
Professor John Coates

Spring 2012

Nanoscale Spatial Organization of Prokaryotic Cells Studied by Super-Resolution Optical Microscopy

by

Andrea Lynn McEvoy

Abstract

Nanoscale Spatial Organization of Prokaryotic Cells Studied by Super-Resolution Optical Microscopy

by

Andrea Lynn McEvoy

Doctor of Philosophy in Biophysics

University of California, Berkeley

Professor Jan T. Liphardt, Chair

All cells spatially organize their interiors, and this arrangement is necessary for cell viability. Until recently, it was believed that only eukaryotic cells spatially segregate their components. However, it is becoming increasingly clear that bacteria also assemble their proteins into complex patterns. In eukaryotic cells, spatial organization arises from membrane bound organelles as well as motor transport proteins which can move cargos within the cell. To date, there are no known motor transport proteins in bacteria and most microbes lack membrane bound organelles, so it remains a mystery how bacterial spatial organization emerges.

In hind-sight it is not surprising that bacteria also exhibit complex spatial organization considering much of what we have learned about the basic processes that take place in all cells, such as transcription and translation was first discovered in prokaryotic cells. Perhaps the fundamental principles that govern spatial organization in prokaryotic cells may be applicable in eukaryotic cells as well. In addition, bacteria are attractive model organism for spatial organization studies because they are genetically tractable, grow quickly and much biochemical and structural data is known about them.

A powerful tool for observing spatial organization in cells is the fluorescence microscope. By specifically tagging a protein of interest with a fluorescent probe, it is possible to examine how proteins organize and dynamically assemble inside cells. A significant disadvantage of this technology is its spatial resolution (approximately 250 nm laterally and 500 nm axially). This limitation on resolution causes closely spaced proteins to look blurred making it difficult to observe the fine structure

within the complexes. This resolution limit is especially problematic within small cells such as bacteria.

With the recent invention of new optical microscopies, we now can surpass the existing limits of fluorescence imaging. In some cases, we can now see individual proteins inside of large complexes or observe structures with ten times the resolution of conventional imaging. These techniques are known as super-resolution microscopes.

In this dissertation, I use super-resolution microscopes to understand how a model microbe, *Escherichia coli*, assembles complex protein structures. I focus on two spatially organized systems, the chemotaxis network and the cell division machinery. These assembly mechanisms could be general mechanisms for protein assembly in all organisms. I also characterize new fluorescent probes for use in multiple super-resolution imaging modalities and discuss the practicalities of using different super-resolution microscopes.

The chemotaxis network in *E. coli* is the best understood signal transduction network in biology. Chemotaxis receptors cluster into complexes of thousands of proteins located at the cell poles and are used to move bacteria towards favorable stimuli in the environment. In these dense clusters, the receptors can bind each other and communicate to filter out noise and amplify weak signals. It is surprising that chemotaxis receptors are spatially segregated and the mechanism for polar localization of these complexes remains unclear. Using data from PALM images, we develop a model to understand how bacteria organize their receptors into large clusters. The model, stochastic cluster nucleation, is surprising in that is generates micron-scale periodic patterns without the need for accessory proteins to provide scaffolding or active transport. This model may be a general mechanism that cells utilize to organize small and large complexes of proteins.

During cell division, *E. coli* must elongate, replicate its DNA and position its components properly prior to binary fission. Prior to septum formation, a ubiquitous protein called FtsZ, assembles into a ring at mid-cell (Z-ring) which constricts during cell division and recruits the remaining proteins necessary for cytokinesis. Though many details have been revealed about FtsZ, the detailed *in vivo* structure of the Z-ring is not well understood, and many questions remain about how ring constriction occurs. Using multiple super-resolution imaging modalities, in combination with conventional time-lapse fluorescence imaging, we show that the Z-ring does not form a long uniform filament around the circumference of the bacterium. We detail how this structure changes during division and how removal of proteins that help to position FtsZ affects the Z-ring as it proceeds through cytokinesis. Ultimately we present a simple model for Z-ring constriction during division.

For Mom and Dad

Contents

List of Figures

Acknowledgements

I would like to thank my advisor Jan Liphardt, who has been a pleasure to work for over the past six years. Thank you for being so generous with your time, advice and for letting me collect all those frequent flyer miles. I have always appreciated you allowing me to make my own decisions, choose my own directions and collaborators and for letting me take much of the credit. Thank you for teaching me how to give a good presentation, for always being positive, for always being there when I needed your help and for keeping me entertained.

I would also like to thank my thesis committee for their support and guidance. Dan Fletcher taught me the wonders of the cytoskeleton, and that it is important to take time to sample other career paths. I'd like to thank John Coates for all of those fun scientific discussions we've had and for telling me all those things I didn't want to hear. I have really appreciated being able to talk with you candidly over the years. And I would like to thank Han Lim for asking all those great difficult questions.

I have been blessed to work with some amazing collaborators who have adopted me over the years. Eric Betzig showed me how much fun PALM could be and gave me so great feedback. He really strives to maintain standards in the field and I have had the luxury of learning so much from him. Harald Hess and Gleb Shtengel have both been pleasures to work with. Not only have we produced some beautiful images of bacteria together, but we have had some great discussions and a lot of fun along the way. Maybe one day we can prove the 'pop and squish' model. Without the aid of Ned Wingreen, our chemotaxis paper would have never been as exciting to biologists. Thank you to Ned for all of your timely and keenly insightful feedback, for all of your patience and your ability to explain the most complex of ideas. Thank you to Paul Goodwin from applied precision (and the whole API team). Not only has Paul taught me a great deal about optics, but he has shown me the way of industry, and been so much fun to work with. It has always made me smile just hearing him laugh. Thank you to Robert Campbell for being dedicated to helping those of us in the imaging field by providing new fluorescent probes. Thank you for all of your timely feedback and advice, I have really enjoyed working with you. And finally, thank you to Stefan Hell, who has graciously allowed me to work in his lab over the past few months and learn from the very accomplished scientists in his lab. Thank you for all of your time and feedback, and for teaching me about German history.

Without the inspiration, support and encouragement of my fellow Biophysics colleagues, I would have never been where I am today. I would like to thank Gin and Dave Richmond, Ailey Crow, Aathi Karunakaran, Melania Strycharska,

Christina Baer, Katherine Miller, Joe Subotnik, Jeff Gore, Peter Pauzauskie, Phillip Elms, Merek Siu, Lisa Green, Nathan and Michele Clack, David Sivak and Jessica Walter for all of the fun memories, great scientific advice and adventures. A special thanks to Jesse Dill and Zain Dossani for all of the fabulous times together; to Courtney Hodges and Giao Hang for being some of the best friends I have ever had; and to Rocky Smith for being a constant source of inspiration and amusement. All you were always up for all the crazy things I wanted to do and I cherish all of the memories we've shared together.

I could not have asked for a better lab than the Liphardt Bees. Thank you to for all the lab trip adventures, "safety" hours, curry lunches, and general camaraderie. I owe special thanks to Jake Siegel, Phillip Jess, and Alan Lowe. Thank you for all the memories, the 'lady boys,' the tiki bars, the time we almost got thrown out of the Paragon, the hilarious comments and most of all for your advice. Lab wouldn't have been the same without all of you all. Thanks to Adam Politzer and Will Draper for many great conversations about bacterial chemotaxis, help with imaging, as well as all those discussion on generally bizarre topics.

I feel like I owe much of my success to Hari Shroff. Thank you for taking me under your wing and for your continuing guidance. You showed me the joys of PALM, climbing, curry, wild ponies that live on the beach and the Liphardt Lab. I feel grateful for your friendship, for your advice and for taking an interest in me. I appreciate you allowing me to tag along with you as a first year grad student, on talks and at Cold Spring Harbor. My life would have been very different without you.

I am very fortunate for having worked with Derek Greenfield. Derek has been a constant source of strength, encouragement and support since I met him. I cannot imagine my life without his friendship. Thank you for pushing me outside my comfort zone, for always challenging me to be a better person and for making me take time to appreciate my accomplishments. I have always appreciated your cleverness, ability to give great talks and all of your coding help. I could not have asked for a better lab partner or best friend. Thank you for all the wonderful memories, the parties we threw, the crazy conference trips we took, and for all of the joy you have brought to my life. Thank you for teaching me about the wonders of salsa dancing and slow cooking. And thank you for not getting me killed on our little escapade to the Orangutan Rehabilitation Center in Borneo ☺.

In addition to Hari and Derek, I owe much of my success to Mark Bates. Thank you for teaching me that STORM and PALM scientists can get along and for teaching me what a real croissant tastes like. I really appreciate that you opened your world to me, answered my stupid questions, broadened my view of our field and edited my papers. Thank you for letting me use your STORM microscope with a

focus lock and for letting me use your analysis software. Your brilliance and cleverness are an inspiration to me and I am continuously amazed by your accomplishments. Thank you for all the wonderful memories: the dog sledding, the trabi tour in Berlin, and the Michelin-star restaurants we tried. Thank you for being a great travel partner and for opening my world to the wonders of mini-cows, Slovenia, Bargain Hunt and Islay. Thank you for taking me to Stockholm twice, I will never forget the first time I saw a wild tufty-eared squirrel. I cherish these memories and our friendship and I am a better person for knowing you.

Finally, I could not have reached this point without the constant support of my family. Thank you to my Dad for all the emotional support, for always being there and for the family credit card ☺. You have always been there for me and I am so lucky to have you in my life. Thank you Mom for being there at all hours, for not getting mad if I have been super busy and forget to call and for taking time out of your schedule to accommodate mine. Your love and support has been one of the most dependable things in my life.

Chapter 1

Introduction

The information presented in this chapter is adapted with permission from McEvoy AL, Greenfield D, Bates, M, Liphardt J (2010). *BMC Biology* 2010, **8:**106 doi:10.1186/1741-7007-8-106

1.1 Prelude

Cells arrange their components in specific ways, and this arrangement is necessary to allow cells to thrive. Until recently, it was thought that only eukaryotic cells have complex arrangements of cellular components, which is made possible by organelles and proteins that transport cargos within the cell, termed motor transport proteins. We now know that prokaryotic cells, such as *E. coli*, also arrange their components in complex ways [1], yet bacteria do not contain any known internal membrane bound organelles or motor transport proteins. Therefore, it remains a mystery as to how bacteria organize and spatially segregate their interiors.

Light microscopy and electron microscopy (EM) have become useful tools to examine the spatial organization of biological samples. In the last decade, the development of new fluorescence microscopy methods has revolutionized how biologists use light microscopes to study cellular structure. However, a disadvantage of fluorescence microscopy is its spatial resolution. Although the structures of the protein complexes within the cell exist at length scales of micrometers to nanometers, the light microscope is unable to resolve structure smaller than approximately 250 nanometers. Features smaller than this size, appear blurred in the microscope image. This limit in resolution, termed the 'diffraction limit' make it difficult to see the fine details in any cell, especially small prokaryotic cells [2].

EM obtains much higher-resolution images than conventional light microscopy. However, unlike the light microscopy, which has the advantage of excellent fluorescence labeling specificity, EM lacks powerful and easy labeling strategies [3]. In addition, EM imaging can only be performed on fixed samples and often requires harsh sample preparation techniques that can disrupt native protein structures. Ideally we would use techniques that combine the specificity of labeled probes with the resolution of EM.

Recently, several optical imaging techniques have been invented that allow for imaging below the diffraction limit, and are termed 'super-resolution' imaging techniques. These techniques exploit certain properties of the label used to visualize the sample to obtain higher-resolution images [4–11]. In this dissertation, I utilize multiple imaging super-resolution imaging modalities to determine the localization and mechanisms for formation of protein complexes in *E. coli* cells. I investigate how proteins assemble by imaging the chemotaxis network using photoactivated localization microscopy (PALM). I examine the detailed structure and mechanism for assembly of the FtsZ ring using PALM, stochastic optical reconstruction microscopy (STORM) and linear-structured illumination (SIM). I also discuss and characterize a novel fluorescent probe which is useful in multiple imaging modalities.

1.2 Single-Molecule Localization Microscopy (SMLM)

Taking advantage of sensitive fluorescence detection methods, single-molecule imaging techniques have improved our understanding of the structure and function of proteins. Recently, these methods have been applied to high-resolution light microscopy, allowing light microscopes to take images with a spatial resolution far beyond the diffraction limit. It was discovered that by imaging individual fluorescent molecules one at a time, an image of a fluorescently labeled sample can be reconstructed at much higher resolution than previously possible. I will refer to this method as single-molecule localization microscopy (SMLM), since it is based principally upon single molecule detection and localization [12]. SMLM combines the benefits of both fluorescent light microscopy and EM, producing nanometer resolution images of structures that have been labeled with high specificity [4–6].

Various implementations of SMLM have been developed by different research groups, and as a result the technique is known by several names, including photoactivated localization microscopy (PALM), stochastic optical reconstruction microscopy (STORM), fluorescence photoactivation localization microscopy (fPALM), and others [4–6, 10, 11, 13].

A single fluorophore inside a cell behaves as a single point source of light. However, when viewed through a microscope, the size of the image of the fluorophore is much larger than the size of the fluorophore itself (Figure 1-1). The broadening of the image of a point source is due to diffraction, an optical effect resulting from the wave-like properties of light interacting with the optics of a microscope; this effect limits the spatial resolution of conventional optical microscopy to ~250 nm laterally, and ~500 nm along the optical axis. The broadened image of a point source produced is termed the point-spread function (PSF) of the microscope (Figure 1-1a right).

Although the image of the fluorophore is broadened by diffraction, the center of the observed image corresponds to the position of the fluorophore. When only a single fluorophore is emitting light, the position of the fluorophore can be found very precisely by measuring the center position of its image. Therefore, if only one tagged protein were present inside the sample, we would be able to know the position of the protein to high precision (Figure 1-1a).

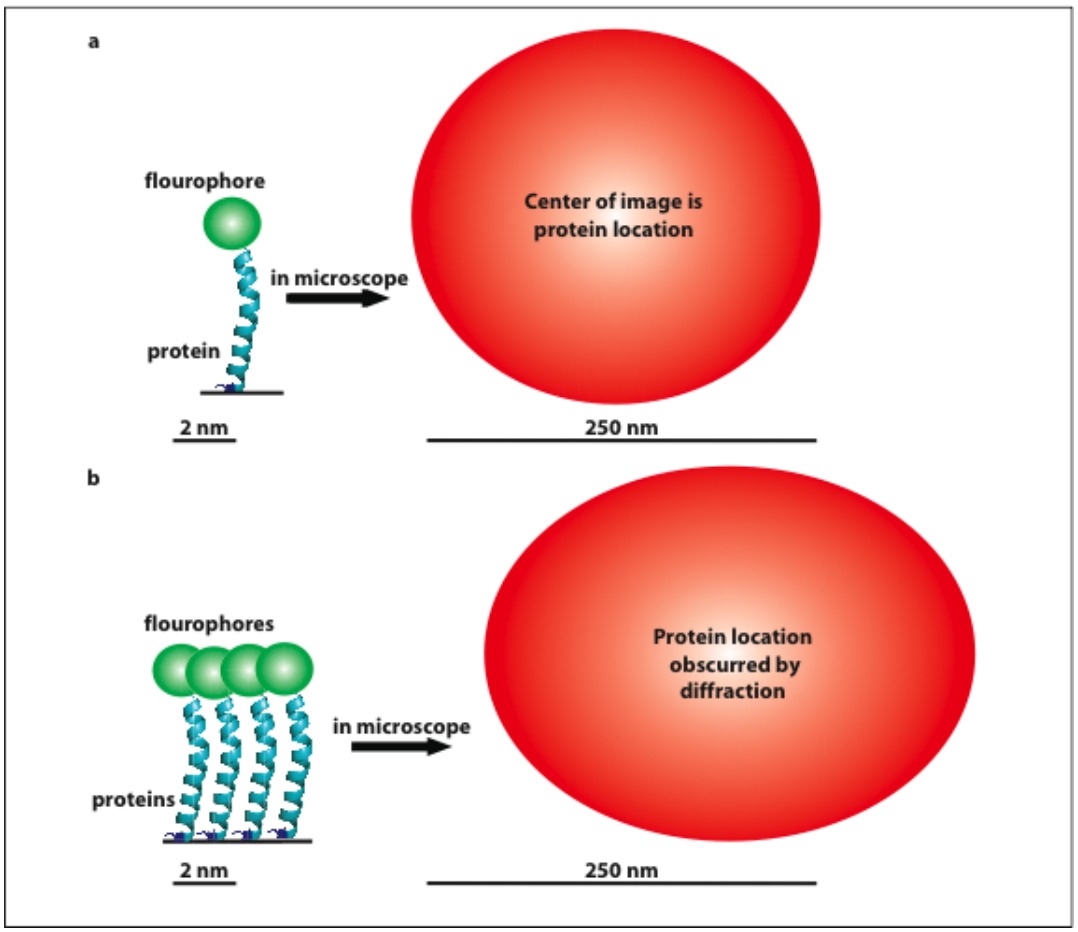

Figure 1-1. The images of fluorophores observed with a microscope are blurred by the wave-like properties of light. (a) The image of a single fluorophore (red circle) has a width greater than ~250nm when viewed with visible light, despite the fact that the fluorophore itself is only a few nanometers in size. The image of such a point emitter is called the point-spread function (PSF). The position of the fluorophore in this case can be determined by measuring the center position of the image, which is equivalent to the PSF in this case. **(b)** When multiple fluorophores are located in close proximity, their images overlap and it becomes difficult to distinguish the individual fluorophores from one another. It is the width of the PSF that limits the ability of the microscope to resolve closely spaced fluorophores. The fluorophore positions cannot be determined accurately in this case.

In cells, many proteins exist in dense complexes, such that the distance between each protein is less than the wavelength of the light used to image them. This means that closely spaced labeled proteins (closer than ~250 nm) appear as a single fluorescent entity when viewed through the microscope (Figure 1-1b). In this situation, it becomes difficult to distinguish the individual fluorophores, and it is impossible to observe the spatial organization of the sample for length scales smaller than several hundred nanometers. This is the reason that traditional fluorescence microscopy, which illuminates all fluorophores in the sample simultaneously (Figure 1-2a), is limited in its spatial resolution.

Since it is difficult to spatially resolve closely spaced fluorophores, SMLM uses the innovative approach of separating the fluorescence of each emitter in time. Instead of imaging all the fluorophores simultaneously, SMLM techniques image each individual fluorophore one at a time, making it possible to find the position of each molecule with high precision. Once all of the positions have been found, they are plotted as points in space to construct an image. The spatial resolution of this image is not limited by diffraction, but only by the precision of the localization process for each fluorophore [4–6, 14].

To observe each protein individually, photoactivatable fluorophores are used. These are fluorescent molecules for which the fluorescence emission can be switched on and off under the control of an external light source. The activation light source illuminates the entire sample but at such a low intensity that only one or a few fluorophores are activated at a time, and the fluorophores that are activated at a given time is random. This enables different photoactivatable fluorophores to be "turned on" at different times, and allows the image of each fluorescent label to be observed individually. Computer algorithms are used to find the locations of each molecule, and these fluorophore locations are then assembled into an image (Figure 1-2c). The location of the molecule is determined by finding the centroid of the image obtained from each molecule (to be discussed in detail later). The precision of the position measurement is dependent on how bright the fluorophore is over the background signal. The brighter the fluorophore, the easier it is to determine its location (Figure 1-2d) [14].

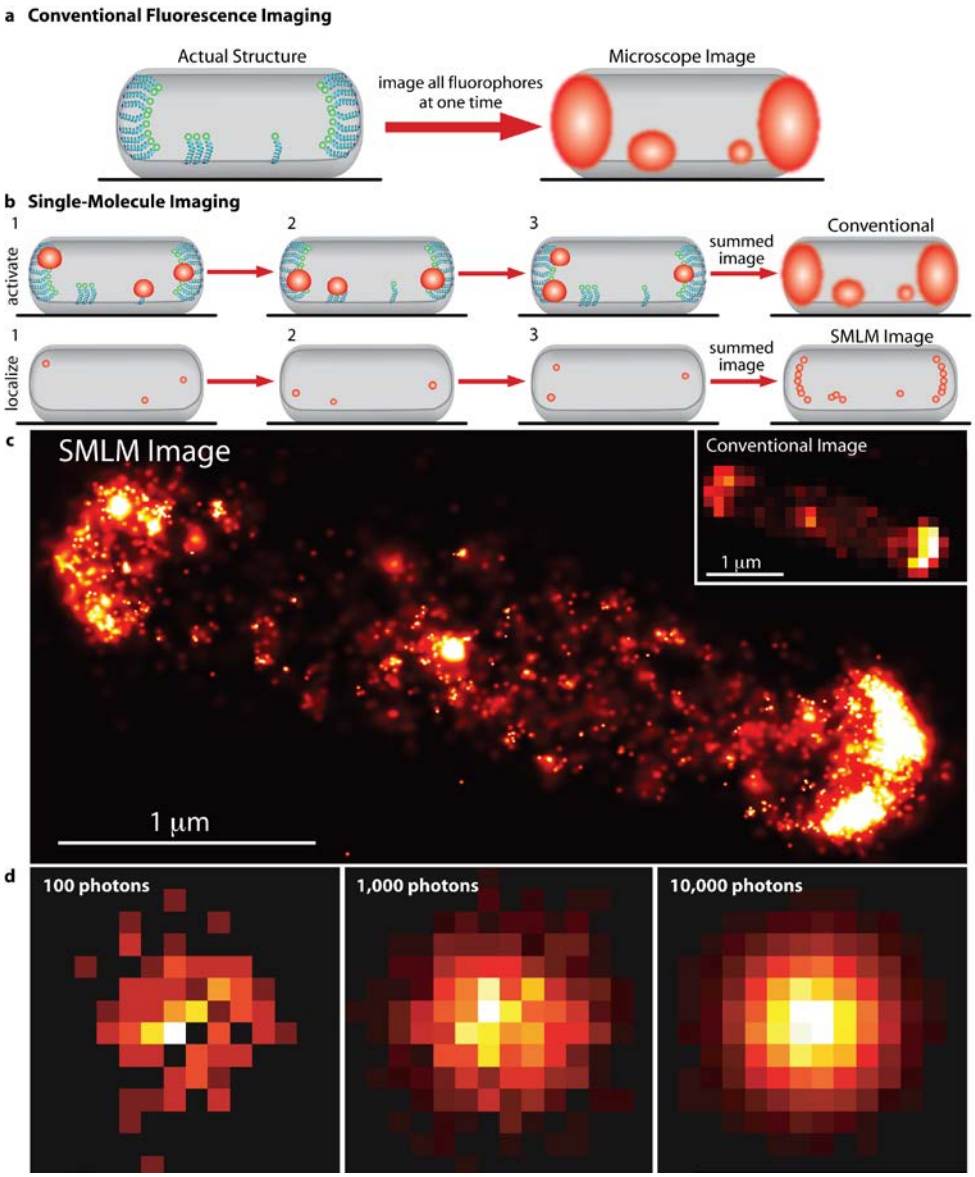

Figure 1-2. Principles of single molecule localization microscopy (SMLM). (a) Conventional fluorescence microscopy excites all fluorophores at once, and therefore the images of closely spaced fluorophores overlap. In this case the best possible image resolution is ~250 nm when using visible light. **(b)** Single molecule localization microscopy techniques activate and observe only a sparse subset of fluorophores at any given time. Since the images of each fluorophore no longer overlap, the location of each fluorophore can be determined precisely. The fluorophore positions can be used to create a super-resolution image of the sample. Instead of plotting the diffraction-limited image of the fluorophore **(top sequence)**, the measured location of each fluorophore is plotted **(bottom sequence)**. **(c)** SMLM image of tagged chemotaxis receptors in *E. coli*. Each small point is a single fluorophore with ~15nm localization precision. The SMLM image is much sharper

than the conventional image **(c inset)**. **(d)** The location of fluorophores can be determined more precisely if the fluorophore emits more photons. If the fluorophore only emits 100 photons **(left)** it becomes more difficult to locate the center of the PSF in comparison to 1,000 **(middle)** or 10,000 **(right)** photons.

Single-molecule imaging requires the use of photoactivable fluorophores of which there are two main categories; photoactivatable fluorescent proteins (paFPs) and photoactivatable synthetic fluorescent dye molecules, such as Cy5 (*11*, *13*, *15*). As with traditional fluorescent proteins like GFP, paFPs can be genetically encoded and fused to proteins of interest. Photoswitchable dyes can be conjugated directly to proteins of interest, or can be conjugated to antibodies that target the protein of interest. The use of dyes or paFPs depends on the biological application. paFPs have the advantage of labeling each protein of interest directly, so they are highly specific. However, paFPs are dimmer than dyes and multi-color imaging is more challenging because many paFPs have similar emission spectra. Some commonly used paFPs include mEos2, pamCherry, Dronpa and Dendra2. Synthetic dyes, by contrast, are very bright but it can be difficult to use dyes to label proteins, particularly in living samples. Immunofluorescence techniques are dependent on the quality of the antibodies used and often have higher background signal due to nonspecific staining. They also often have a lower density of labeling in comparison to paFPs. Samples labeled with paFPs can be imaged in any non-fluorescent media, while some synthetic dyes require the use of reducing agents in the imaging buffer to photoswitch properly [11, 16, 17].

To acquire an image of a sample labeled with paFPs, it is necessary to first grow the cells and express the fusion protein. Once the cells have been grown, they should be fixed and either placed on a coverslip for imaging, or imaged on the coverslip they were grown on. Alternately, if dyes are used, the cells should first be grown and then fixed. The cells are then permeabilized and labeled using a strategy such as immuno-fluorescent labeling which uses dyes that have been conjugated to antibodies [4, 5, 11, 13, 15, 16].

Since SMLM image acquisition may take a long time, any drift of the sample stage during data collection will need to be corrected. For this purpose it is often useful to include fluorescent particles on the surface of the sample or the glass substrate. These fluorescent particles, such as gold nanoparticles, allow you to track any lateral movements of the stage during image acquisition and correct for drift in software [4, 13].

Traditional fluorescent microscopes can easily be modified for single-molecule localization microscopy. In most cases, SMLM has been performed using total internal reflection (TIR) illumination, which limits the light to the bottom 100-150 nm of the sample, thus reducing out-of-focus light and making it easier to observe single molecules. It is convenient to use TIR imaging if you are imaging proteins close to the bottom of cells. However, for thin samples such as EM sections or small cells, it is possible to illuminate using epi-fluorescence [4].

It is necessary to add the proper laser lines to an existing microscope, and this is dependent on the choice of fluorophore. Lasers are frequently used because they deliver the necessary power to image quickly. Like all fluorescence microscopy, it is necessary to have proper excitation and emission filters to maximize your signal to noise ratio [4, 5, 11, 13, 18].

In addition to the lasers and microscope, it is beneficial to use an objective with a high numerical aperture (NA = 1.4 or higher) such that as many photons as possible are collected. To collect the data, a sensitive CCD camera (such as an electron-multiplying CCD) is also required to observe as many photons as possible. Since single-molecule imaging techniques are wide-field and it may take a long time to look at each fluorophore individually, the data files obtained can become quite large [11, 13], therefore an appropriately fast computer with sufficient storage space is essential.

Once you have acquired your single-molecule imaging data, you will typically have a stack of thousands to hundreds of thousands of single image frames. Each frame will have points of intensity corresponding to the light emitted from a fluorescent label. It is necessary to find the locations of each fluorophore in each frame and then computationally assemble those locations into a composite image. This composite image can be thought of as a map of the best estimation of where the fluorophores are located during imaging. I will consider the 2D imaging case for ease of discussion.

To find the location of each fluorophore, it is necessary to first identify each single molecule. This is done by choosing an appropriate threshold to distinguish the signal each molecule emits from the background [11, 13]. If the signal is high enough, it is considered to be a target fluorophore. If the switching event lasts longer than one image frame, signals can be combined across frames to increase the signal obtained from each fluorophore. Once a target fluorophore is found, the signal is fit to a 2D Gaussian (or the centroid of the signal is determined). How well a Gaussian can fit the signal is dependent on how bright the signal is above background (Figure 1-2d). In the SMLM image, the location of each fluorophore is represented as a small Gaussian intensity peak, whose width is scaled according to the precision of

"localizing" that fluorophore. In other words, the blurred image of the emitter is replaced with the best guess as to where the fluorophore is located.

Since it may be necessary to image the sample for a long time, it is also important to perform drift correction on the image using appropriate methods [4, 11, 13, 19]. Image processing is a challenging aspect of single-molecule imaging. Recently, a new ImageJ plug-in was developed to process single-molecule imaging data in both 2D and 3D [20]. The development of such processing tools will facitilate the use of single-molecule imaging techniques for the broader scientific community.

Since single-molecule imaging techniques look at each molecule individually, in principle, it is possible to count each photoactivation event as representing one fluorophore. If the fluorophore is an irreversibly photoactivatable protein (i.e. once the protein is observed, it is not capable of re-excitation), the number of excitation events corresponds to the number of proteins observed in the sample [21–23]. In addition to the number of proteins, you also obtain the location of each protein in the sample. Essentially, a "protein map" is obtained that can be used to determine the nearest neighbor distances for all the proteins. It is also possible to search for ordered protein structures, however, the error associated with each protein position may obscure any regular ordered structure depending on the dimensions of the structure [23].

It is important to keep in mind that there are many caveats associated with counting proteins as well as doing statistical analysis with single-molecule imaging data. It is important to ensure that only one fluorophore at a time in each diffraction-limited region (~250 nm) is excited, which requires very low activation power. This extends the time required to image the sample. Also, if you want to count absolute numbers of proteins, it is necessary to image the sample until all the proteins have been activated and then photobleached. Another concern is that there may be a population of paFPs that do not fold properly and are therefore not observable, or that are observable but emit too few photons to be identified as single molecules. Therefore, caution must be taken when making statements about the absolute numbers of proteins in a biological sample, and it is often more practical to draw conclusions about the relative number of proteins within a sample [21–23].

In addition to obtaining 2D fixed cell data, SMLM has been performed on live-cells and also in 3D [19, 21–26]. Live-cell imaging often utilizes paFPs, since sample preparation necessary for dye conjugation is more difficult to perform on living samples. Like fixed cell imaging, live-cell imaging still excites each fluorophore individually, therefore at any given time interval, only a few fluorophores will be observed. One caveat of live-cell SMLM is that it is relatively slow compared to other fluorescence imaging techniques. Since each fluorophore is localized at a different point in time, to create a time-lapse movie, the localizations have to be binned into

time windows and a series of SMLM images are reconstructed [24, 26]. With current techniques, these time windows are typically seconds in duration to obtain a sufficient number of localizations in each window. Additionally, care must be taken to avoid cellular damage by reducing laser power, which slows down image acquisition. Therefore, in many cases, the speed of most dynamic biological processes to too fast to be captured by live-cell SMLM movies. Instead, it may be more useful to use SMLM to track the individual movements of proteins inside live cells to nanometer precision [17].

3D single-molecule imaging has been performed using both dyes and paFPs [19, 25, 27–29]. 3D imaging can be performed using several methods. One approach is to break the axial symmetry of the PSF by adding a cylindrical lens to the imaging path, therefore causing the shape of each fluorophore's image to change depending on its z-position within the sample [19]. This allows the user to calibrate the change in the image depending on the height of the fluorophore inside the sample. This technique has a wide z-range, but altering the shape of the PSF complicates the localization algorithms and may decrease the lateral resolution of the image. A more precise way of getting 3D information is to use interferometry, which uses phase information from the light emitted by the fluorophore to obtain height information. This allows for 10 nm axial resolution, but due to the limitations of the current system, imaging is restricted to a relatively thin region at a depth of ~500 nm into the sample [25, 27, 28] . Interferometry requires the use of multiple objective lenses, significantly increasing the complexity of the system and making alignment and data processing more challenging.

Though SMLM imaging has challenges and can have limited applications, SMLM offers the highest resolution of all current fluorescence microscopy techniques. Additionally, SMLM is relatively easy to implement in comparison to other super-resolution techniques.

1.3 Structured Illumination (SIM), Stimulated Emission Depletion Microscopy (STED) and a Comparison to SMLM

Rather than using photoswitchable probes, it is also possible to obtain images with resolutions better than the diffraction limit using patterned illumination. Two such techniques are known as structured illumination (SIM) [7, 30] and stimulated emission depletion microscopy (STED) [8, 31]. SIM projects striped illumination to a sample, which is typically generated by passing excitation light through a grating. The fluorophores being illuminated are excited strongly, depleting the ground state in the regions that are illuminated by the pattern. Since the pattern only covers part of the field of view, the pattern is scanned across the sample and tilted to obtain three-dimensional information. The images collected are subjected to mathematical reconstructions that generate a reconstruction of the sample [30].

Though the patterned light can interact with structures finer than the diffraction limit, the light pattern itself is diffraction limited. The resulting SIM reconstructed images have twice the resolution of conventional imaging techniques in X, Y and Z. Additionally, since SIM produces high-resolution images using patterned illumination, no special fluorophores are required, and conventional probes like GFP or dyes can be imaged.

Alternatively, STED also used patterned illumination to obtain super-resolution images, but in this case, two beams are used to create the image. One laser is used to excite the fluorophore and a second beam is used to shape the excitation light by confining fluorophores to their ground state [8, 31]. This patterned illumination is implemented as a donut shape overlayed on the excitation beam such that only the small region in the center is capable of exciting fluorophores. These two beams are then scanned across the sample to obtain super-resolution images. By changing the size or intensity of the donut, the region in the center can be made arbitrarily small. Thus, STED has theoretically limitless resolution. Optically, both SIM and STED are more challenging to implement than SMLM, but commercial microscopes are available.

All three imaging modalities, SIM (Figure 1-3a), SMLM (Figure 1-3b), and STED (Figure 1-3c) have advantages and disadvantages and can be combined to understand biological systems. Therefore it is important to understand the differences of each technique and when to implement each one (Table 1-4.).

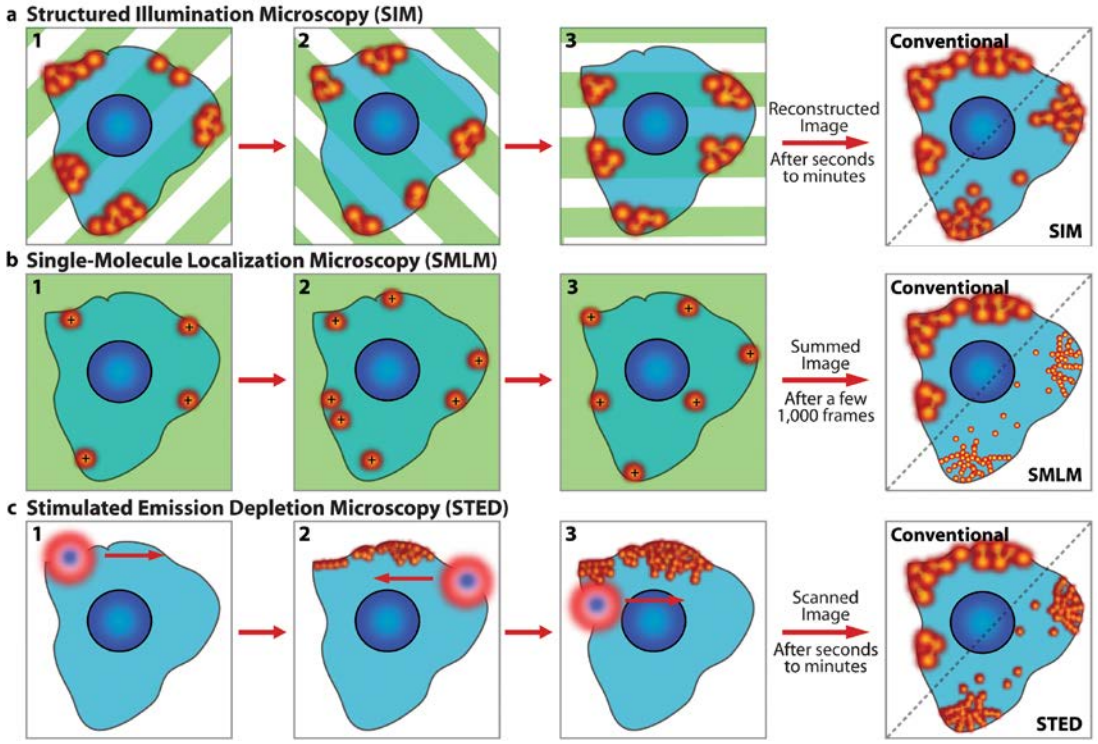

Figure 1-3. Sub-diffraction limited imaging techniques. (a) A cell labeled with conventional fluorophores is illuminated with patterned light. In subsequent frames, the phase and orientation of the pattern is changed. Using a series of images as well as mathematical algorithms, the sub-diffraction limited image is reconstructed with twice the resolution of conventional imaging (right). **(b)** A cell labeled with photoactivatable fluorophores is imaged with SMLM. In each frame, a sparse subset of fluorophores is imaged using wide-field illumination. The center of each fluorophore's image is found (denoted by +) and once all fluorophores have been located, the centers are plotted in a final image. The SMLM image has ten times the resolution of the conventional image (right). **(c)** Using STED, the sample is scanned with two overlapping lasers, one used for excitation of fluorophores, and the other is used to effectively narrow the radius of excitation so only a subset of the fluorophores are imaged at one time. STED images typically have 2-10 times the lateral resolution of conventional imaging (right).

Most protein complexes exist in three-dimensional structures; therefore to make meaningful statements about protein structure, 3D imaging is required. Additionally, many biological structures exist far from the coverslip deep into cells and tissues. For quite some time, three-dimensional imaging deep into cells and tissues has been a challenge for light microscopy. As one looks deeper into cells, the cellular autofluorescence and light scattering increases, which can obscure the signal obtained from the fluorescent labels.

3D-SIM images are attained using a 3D light patterned to excite fluorophores in a sample along all three axes [32]. Since the light pattern is projected into the sample in all three dimensions, the increased resolution exists axially as well as laterally. This two-fold resolution improvement in all three dimensions means that 3D-SIM provides an eight-fold resolution improvement in volume in comparison to conventional microscopy. Using 3D-SIM, it is also possible to obtain this increase in resolution relatively deep into intact whole cells (at least 10 μm [33]). Since 3D-SIM uses specialized light patterns to optically section samples rejecting some of the out-of-focus light, there is an increase of signal-to-noise obtained from a sample and depths of 20 μm into a sample have been reached [33].

Table 1-4. Comparison of sub-diffraction limited imaging techniques

Feature	SMLM	STED	3D-SIM
Basic principle	Localization of single molecules using wide-field illumination	An effective smaller excitation illumination is scanned across the sample to image a subset of fluorophores at a time	Patterned illumination excites the sample in many orientations to reconstruct the image
Lateral resolution	20 - 50 nm	20 - 100 nm	100 -130 nm
Axial resolution	10 - 75 nm Most typically performed with TIRF illumination	20 – 100 nm (isoSTED) 100 - 700 nm depending on the implementation	250 - 350 nm
z-depth range	100 nm (TIRF) to a few μm (Temporal-focusing and astigmatic lenses can extend the z-range)	> 20 μm	10-20 μm
Fluorophores	Photoswitchable dyes or proteins	Works with some conventional fluorophores, best with Atto 647, 655 dyes as well as mCitrine, EYFP	Conventional fluorophores

The patterned depletion beam used in STED can be used to shape the excitation light in all three dimensions [8, 35, 36, 37], however if the depletion beam is only applied in the focal plane there is limited benefit in the axial dimension (~600 nm resolution in z). To obtain the highest axial resolution with STED, the light pattern is made in all three dimensions and two opposing objectives are used [37]. While this technique can obtains images with resolutions of 20 -100 nm in all three dimensions the additional optics can be challenging to align and the large power intensity required to image the sample can induce photobleaching. Since STED optically sections the sample, it is possible to image deeply into cells (greater than 20 μm [33]).

Currently, there are several advanced approaches to 3D-SMLM. One method adds a cylindrical lens to the imaging path, which changes the image of the fluorophore observed based on its height in the sample [19]. This technique has a wide z-range (at least 3 μm [38]), but complicates the localization algorithms and may decrease the lateral resolution of the image [19]. An alternative approach uses interferometry, which uses phase information from the light emitted by the fluorophore to obtain height information. This allows for 10 nm axial resolution, but due to technical limitations of this approach, imaging is restricted to a relatively thin depth of ~500 nm to 1 μm [25, 27, 28] . Interferometry also requires the use of multiple objective lenses, significantly increasing the complexity of the system and making alignment and data processing more challenging.

In the case of SMLM, imaging deeply into cells is difficult because the increased autofluorescence background can obscure the light emitted from single fluorophores. Furthermore, added background may make it more difficult to determine the locations of each fluorophore because the image of the fluorophore may change unpredictably due to heterogeneity of the sample. Therefore, many SMLM implementations have used total internal reflection fluorescence (TIRF) illumination, which restricts the excitation to 100-150 nm into the sample. However, there are a few implementations that are capable of imaging deep into whole intact cells [29, 39]. Additionally, to circumvent these issues, it is possible to physically section samples using electron microscopy sample preparation techniques then perform serial section imaging and realignment [4].

One major consideration that applies to all three techniques is that the further away from the coverslip one images, the more likely that the sample will change in non-uniform ways introducing spherical aberration. In the case of SMLM and STED, this effect could cause a decrease in the resolution of the images. In the case of 3D-SIM, it could cause imaging artifacts known as moiré fringes that manifest themselves as striped patterns superimposed on the image. To help decrease the artifacts produced by imaging deep into a sample, it is critical to match the index of

refraction of the sample and imaging medium with that of the system optics regardless of which imaging technique is used.

Acquisition times using 3D-SIM can be relatively quick, 15-20 seconds to acquire a 2 um x 512 x 512 stack, (a total of 255 frames). Ultimately the total acquisition time is limited by the exposure time necessary to acquire an adequate signal to noise in the image. These frame rates are not limited by the number of channels used and four simultaneous channels are possible.

SMLM techniques image each fluorophore individually, therefore it is an inherently slow process. As the number of closely spaced fluorophores increases, the imaging time will also increase, potentially requiring hours to obtain the data necessary to form an image. For example, due to the high density of fluorophores inside of an *E. coli* cell (1000 per micron^2 for the labeled chemotaxis receptor shown in Figure 1-2a), this 2D image required 3 hours of acquisition time [23]. However, it does exhibit ten times the resolution of the conventional wide-field image (Figure 1-2b).

Since STED is a laser scanning technique, the speed of the imaging depends on the signal to noise within the sample and the image area scanned. The brighter the sample is, the easier it will be to image quickly and obtain axial information. Most STED images can be acquired in seconds to minutes. The first demonstration of video rate live cell imaging at sub-diffraction limit resolution was accomplished using this technique, achieving frame rates of 30 frames-per-second at a spatial resolution of 60 nm [35].

Post-acquisition processing is also an important concern when choosing an imaging modality. In addition to the 3 hours of acquisition time, the cell in figures 1-2a-b required an additional 3 hours of post-processing to generate the image [23]. Alternatively, the dual-color 3D-SIM image acquired on the DeltaVision OMX (Figure 1-2c), with twice the resolution of the conventional image (Figure 1-2d), was acquired in 30 sec with an additional 30 sec of processing time to reconstruct the image.

Sample preparations can add time and difficulty to any experiment and should be considered when choosing an imaging modality. Labeling protocols usually consist of either labeling proteins of interest with a genetically encoded fluorescent protein or by conjugating a fluorophore to an antibody that targets a protein of interest, as in the case of immunofluorescence.

Since 3D-SIM does not require special fluorophores or multiple-lasers for single-color acquisition, multi-color imaging is highly practical. This allows for ease of transition to higher resolution imaging with minimal sample prep changes. There is no need to use new labeling techniques to obtain 3D sub-diffraction limited images quickly.

SMLM requires the use of photoactivable fluorophores, which in most cases, means that the user is required to make new samples by either creating fusions to photoactivatable fluorescent proteins (paFPs) or by changing immunofluorescence protocols. Multicolor SMLM imaging has been demonstrated using different paFPs variants and photoswitchable dyes [15, 24, 28, 40] but multicolor SMLM imaging remains challenging due to the limited availability of suitable probes.

In principle, STED can be used with any fluorophore, however, some fluorophores are particularly well suited for STED imaging including EYFP and mCitrine, in addition to dyes Atto 647N and Atto 655. Multicolor imaging can also be done with STED [41], however the requirement for spectrally distinct excitation, emission and depletion bands has limited the technology to two colors.

Ultimately, each super-resolution technique has advantages and disadvantages, and should be used appropriately. However, like all techniques or assays, it is important to consider which methods are appropriate for a particular system. With the invention of new imaging modalities, it will be very exciting to see how they are adopted and applied to biological systems in the future.

1.4 Prokaryotes and *Escherichia coli*

Many cellular processes can be elucidated through higher-resolution optical imaging. Applying these tools to small cells, such as prokaryotes, is especially attractive because the added resolution obtained can resolve structures never observed before. I have focused on *Escherichia coli* because of there is a large amount of biochemical, structural and genetic data available. It is perhaps the best understood organism on the planet. *E. coli* was discovered in 1885 by Theodor Escherich, and it has become a model system due to ability to grow quickly on a variety of nutrients in aerobic conditions. It is now easier to manipulate the DNA inside *E. coli* than any other organism.

E. coli is a rod shaped bacterium approximately 2 μm long and 1 μm in diameter. They are able to sense their environment and move towards things they metabolize by rotating a series of helical propellers called flagella. These flagella dot the cell surface randomly, but on swimming cells they coalesce into a single bundle and propel the cell body forward up to 30 μm/sec [42].

E. coli is a prokaryote, meaning that it lacks a membrane bound nucleus. Since prokaryotic cells do not have membrane-bound organelles, they were thought to contain a homogeneous mixture of proteins and nucleic acids. However, recently it was discovered that prokaryotic cells spatially segregate their interiors. For example, the DNA is tightly packed into a structure that is actively segregated during cell division. Several proteins form helical filaments that may help to organize the cell or provide a scaffold for growth. Furthermore, some proteins are only found at specific locations within the cell, or form rings only at certain times in the cell cycle. The protein complexes are necessary for cell viability and for protein function.

Much of our understanding of the basic processes that take place in all cells – transcription, translation, DNA replication, glucose metabolism – was first discovered in the prokaryote *E. coli*. Perhaps the fundamental principles that govern spatial organization in prokaryotic cells may also be utilized in eukaryotic cells.

1.5 Super-Resolution Imaging of the Chemotaxis Network

All living things must find a suitable environment for growth and reproduction, and bacteria are no exception. *E. coli* are equipped with the ability to sense and respond to their environment such that they are able to swim toward favorable environments [42]. Their ability to sense and move towards things they metabolize is known as chemotaxis, and the *E. coli* chemotaxis network is the best understood signal transduction pathway in all of biology. Researchers have identified all the proteins in *E. coli* that interact to make chemotaxis possible and much biochemical and structural data is known. Receptors in the cytoplasmic membrane bind chemicals and communicate this information using a series of protein-protein interactions that transfer phosphate groups. During this process the signal from the binding of chemicals is eventually relayed to the flagellar motor which will switch direction based on the chemical concentrations it senses. As the flagellar motor switches direction, it causes the bundle of flagella to come apart, halting the swimming motion and causing the cell to tumble in place. By changing how often a cell swims or tumbles, the network of chemotaxis proteins is able to direct the cell toward a more suitable environment – swimming in a favorable direction is prolonged, whereas swimming in the wrong direction is quickly halted [42].

Perhaps non-intuitively, chemotaxis receptors are not spread evenly all over the cell, but are found in enormous sensory complexes located at the polar ends of the bacterium [42–44]. In these dense clusters, the receptors can bind each other and communicate to filter out noise and amplify weak signals [45–47].

Though we understand the benefits of chemotaxis receptor clustering, the mechanism for how these large clusters localize to the poles of the cell had yet to be elucidated. If it were possible to observe all the individual chemotaxis receptors inside single cells and continue to watch their motion as the receptors diffuse within the membrane, it might be easy to determine the mechanism that receptors use to localize to polar clusters. However, electron microscopy lacks powerful labeling strategies to see all receptors inside the cells and individual receptors are too small to observe in their native environment using traditional optical microscopy. Additionally, since the proteins are in high density clusters, the proteins are closer together than the wavelength of visible light and are therefore unresolvable.

To understand the mechanism of chemotaxis cluster localization, we used SMLM microscopy (also known as PALM) to observe the distribution of individual chemotaxis clusters inside of cells. We utilized a novel fluorescent protein, Eos, which can be sparsely photoactivated to see single proteins within the cells. In

chapter 2, we describe in detail how we imaged chemotaxis proteins using PALM. Using these images, we develop a model that explains how receptors localize to cell poles. In chapter 3, we derive this model. Surprisingly, the mechanism does not require other proteins to move receptors, nor does it require cytoskeleton tracks or anchoring sites to guide or hold receptors in certain locations.

1.6 Super-Resolution Imaging of the Cell Division Machinery

Cell division is a hallmark of life. All cells coordinate and regulate their protein complexes to produce viable offspring. During *E. coli* cell division, the cell must elongate, replicate its DNA and move each chromosome to the polar regions of the cell prior to binary fission. Prior to septum formation, a protein called FtsZ assembles into a ring structure at mid-cell (Z-ring). The Z-ring mediates cell division by recruiting other proteins necessary for cytokinesis and is thought to provide a force on the membrane which is used to constrict the midcell [48].

Though many details have been revealed about FtsZ, the detailed *in vivo* structure of the Z-ring is not well understood, and many questions remain about how the ring constricts as the cell proceeds through cell division. Using conventional optical microscopy, FtsZ has been shown to assemble into a dynamic spiral structure that oscillates within the cell until the cell approaches cytokineses, where FtsZ appears to assemble into a complete ring which constricts until cell division is complete [49, 50]. Contrary to this picture, recent cryotomography images of *Caulobacter crescentus* show that FtsZ assembles into a small number of isolated filaments in the middle of the cell which do not form a complete ring around the septum [51]. Since this structure is intimately related to how FtsZ performs force constriction, it is important to understand the nature of this structure. However, conventional fluorescence microscopy does not have sufficient resolution to see individual FtsZ filaments.

To obtain the *in vivo* structure of FtsZ, we utilized different super-resolution imaging modalities. As suggested by Li *et al.*, the Z-ring seems to be formed from a series of smaller filaments which forms a ring of non-uniform density around the circumference of the bacterium [51]. Consistent with this structure, the curvature of the membrane at mid-cell is also not symmetric around the entire cell.

Super-resolution images allow for characterization of the ring dimensions with unprecedented resolution. In chapter 4, we detail how the Z-ring changes throughout the cell cycle and how local concentration of FtsZ affects membrane curvature. We show how removing the localization mechanisms, which position FtsZ, effect the Z-ring during division. Ultimately, we present a simple model for Z-ring constriction and force generation throughout the cell cycle.

1.7 Novel Fluorescent Proteins for Use with Multiple Imaging Modalities

Current super-resolution imaging techniques all have advantages and disadvantages. Therefore, it can be beneficial to use multiple imaging modalities to image biological systems [12, 33]. This can be challenging because each imaging technique has different requirements for fluorophores.

SMLM requires photoactivatable fluorescent probes that "turn" on or off, usually in response to light. Ideally, these probes would be completely dark, and in response to 'activation' light, become infinitely bright. Once the fluorophore emits many photons, it would then photobleach quickly. These probes can be photoswitchable dyes, photoactivatable fluorescent proteins (paFPs), photoswitchable fluorescent proteins (psFPs) or photoconvertible fluorescent proteins (pcFPs). paFPs, psFPs and pcFPs have the benefit that they are genetically encodable, conducive for live cell imaging and exquisitely specific, however, many are dim and not photostable. Additionally, functional fusion proteins can be difficult to obtain.

In contrast, SIM and STED require bright fluorophores that are very photostable. Both SIM and STED are capable of using existing conventional fluorescent proteins such as GFP or YFP. pcFPs have a fluorescence state similar to GFP that does not require activation to fluoresce, known as an inactive state. If a pcFP had a very bright and/or photostable inactive state and yet could be photoconverted to a bright state that photobleaches relatively quickly, the protein would be useful in multiple super-resolution imaging modalities [12, 33].

As super-resolution imaging techniques become more widespread, it may be useful to use different imaging modalities on a given sample. In chapter 6, we describe and characterize two new pcFPs known as mMaple and mClavGR3, which exhibit properties that make them useful in multiple imaging modalities such as PALM and SIM. We characterize these proteins *in vitro* and *in vivo* and compare them to existing pcFPs.

1.8 References

1. Whitman, William, Coleman, David, Wiebe W: Prokaryotes: The unseen majority. *PNAS* 1998, 95:6578-6583.

2. Murphy D: *Fundamentals of Light Microscopy and Electronic Imaging*. John Wiley & Sons, Inc.; 2001.

3. Kuo J: *Electron Microscopy: Methods and Protocols*. 2nd edition. Humana Press Inc.; 2007.

4. Betzig E, Patterson GH, Sougrat R, Lindwasser OW, Olenych S, Bonifacino JS, Davidson MW, Lippincott-Schwartz J, Hess HF: Imaging Intracellular Fluorescent Proteins at Nanometer Resolution. *Science* 2006, 313:1642-1645.

5. Rust MJ, Bates M, Zhuang X: Sub-diffraction-limit imaging by stochastic optical reconstruction microscopy (STORM). *Nat Meth* 2006, 3:793-796.

6. Hess Girirajan T, Mason M S: Ultra-High Resoluion Imaging by Fluorescence Photoactivation Localization Microscopy. *Biophysical Journal* 2006, 91:4258-4272.

7. Gustafsson MG: Surpassing the lateral resolution limit by a factor of two using structured illumination microscopy. *Journal of microscopy* 2000, 198:82-7.

8. Klar TA, Hell SW: Subdiffraction resolution in far-field fluorescence microscopy. *Opt. Lett.* 1999, 24:954-956.

9. Dempsey GT, Wang W, Zhuang X: Handbook of Single-Molecule Biophysics. 2009:95-127.

10. Hell SW: Microscopy and its focal switch. *Online* 2008:1-9.

11. Patterson G, Davidson M, Manley S, Lippincott-Schwartz J: Superresolution imaging using single-molecule localization. *Annual review of physical chemistry* 2010, 61:345-67.

12. McEvoy AL, Greenfield D, Bates M, Liphardt J: Q&A: Single-molecule localization microscopy for biological imaging. *BMC biology* 2010, 8:106.

13. Dempsey GT, Wang W, Zhuang X: Fluorescence Imaging at Sub-Diffraction-Limit Resolution with Stochastic Optical Reconstruction Microscopy. In 2009:95-127.

14. Thompson Larson, D. R., Webb, W. RE: Precise nanometer localization analysis for individual fluorescent probes. *Biophysical Journal* 2002, 82:2775-2783.

15. Bates M, Huang B, Dempsey GT, Zhuang X: Multicolor Super-Resolution Imaging with Photo-Switchable Fluorescent Probes. *Science* 2007, 317:1749-1753.

16. Bates M, Huang B, Zhuang X: Super-resolution microscopy by nanoscale localization of photo-switchable fluorescent probes. *Current Opinion in Chemical Biology* 2008, 12:505-514.

17. Manley S, Gillette JM, Patterson GH, Shroff H, Hess HF, Betzig E, Lippincott-Schwartz J: High-density mapping of single-molecule trajectories with photoactivated localization microscopy. *Nat Meth* 2008, 5:155-157.

18. Hess ST, Gould TJ, Gudheti MV, Maas SA, Mills KD, Zimmerberg J: Cynamic clustered distribution of hemagglutinin resolved at 40 nm in living cell membranes discriminates between raft theories. *Proceedings of the National Academy of Sciences* 2007, 104:17370-17375.

19. Huang B, Wang W, Bates M, Zhuang X: Three-Dimensional Super-Resolution Imaging by Stochastic Optical Reconstruction Microscopy. *Science* 2008, 319:810-813.

20. Henriques R, Lelek M, Fornasiero EF, Valtorta F, Zimmer C, Mhlanga MM: QuickPALM: 3D real-time photoactivation nanoscopy image processing in ImageJ. *Nat Meth* 2010, 7:339-340.

21. Annibale, Paolo, Scarselli, M., Kodiyan, A., Radenovic A: Photoactivatable Fluorescen Protein mEos2 Displays Repeated Photoactivation after a Long-Lived Dark State in Red Photoconverted Form. *Journal of Physical Chemistry Letters* 2010, 1:1506-1510.

22. Annibale P, Vanni S, Scarselli M, Rothlisberger U, Radenovic A: Identification of clustering artifacts in photoactivated localization microscopy. *Nature Methods* 2011, 8:7-8.

23. Greenfield D, McEvoy AL, Shroff H, Crooks GE, Wingreen NS, Betzig E, Liphardt J: Self-organization of the Escherichia coli chemotaxis network imaged with super-resolution light microscopy. *PLoS biology* 2009, 7:e1000137.

24. Jones SA, Shim S-H, He J, Zhuang X: Fast, three-dimensional super-resolution imaging of live cells. *Nat Meth* , 8:499-505.

25. Shtengel G, Galbraith JA, Galbraith CG, Lippincott-Schwartz J, Gillette JM, Manley S, Sougrat R, Waterman CM, Kanchanawong P, Davidson MW, Fetter RD, Hess HF: Interferometric fluorescent super-resolution microscopy resolves 3D cellular ultrastructure. *Proceedings of the National Academy of Sciences* 2009, 106:3125-3130.

26. Shroff H, Galbraith CG, Galbraith JA, Betzig E: Live-cell photoactivated localization microscopy of nanoscale adhesion dynamics. *Nat Meth* 2008, 5:417-423.

27. Aquino D, Schonle A, Geisler C, Middendorff C v, Wurm CA, Okamura Y, Lang T, Hell SW, Egner A: Two-color nanoscopy of three-dimensional volumes by 4Pi detection of stochastically switched fluorophores. *Nat Meth* , 8:353-359.

28. Kanchanawong P, Shtengel G, Pasapera AM, Ramko EB, Davidson MW, Hess HF, Waterman CM: Nanoscale architecture of integrin-based cell adhesions. *Nature*, 468:580-584.

29. Vaziri A, Tang J, Shroff H, Shank CV: Multilayer three-dimensional super resolution imaging of thick biological samples. *Proceedings of the National Academy of Sciences* 2008, 105:20221-20226.

30. Gustafsson MGL: Extended resolution fluorescence microscopy. *Current Opinion in Structural Biology* 1999, 9:627-628.

31. Hell SW: Far-Field Optical Nanoscopy. *Science* 2007, 316:1153-1158.

32. Gustafsson MGL, Shao L, Carlton PM, Wang CJR, Golubovskaya IN, Cande WZ, Agard DA, Sedat JW: Three-Dimensional Resolution Doubling in Wide-Field Fluorescence Microscopy by Structured Illumination. *Biophysical Journal* 2008, 94:4957-4970.

33. Schermelleh L, Heintzmann R, Leonhardt H: A guide to super-resolution fluorescence microscopy. 2010, 190:165-175.

34. Harke B, Ullal CK, Keller J, Hell SW: Three-Dimensional Nanoscopy of Colloidal Crystals. *Nano Letters* 2008, 8:1309-1313.

35. Hein B, Willig KI, Hell SW: Stimulated emission depletion (STED) nanoscopy of a fluorescent protein-labeled organelle inside a living cell. *Proceedings of the National Academy of Sciences* 2008, 105:14271-14276.

36. Nagerl UV, Willig KI, Hein B, Hell SW, Bonhoeffer T: Live-cell imaging of dendritic spines by STED microscopy. *Proceedings of the National Academy of Sciences* 2008, 105:18982-18987.

37. Schmidt R, Wurm CA, Jakobs S, Engelhardt J, Egner A, Hell SW: Spherical nanosized focal spot unravels the interior of cells. *Nat Meth* 2008, 5:539-544.

38. Huang B, Jones SA, Brandenburg B, Zhuang X: Whole-cell 3D STORM reveals interactions between cellular structures with nanometer-scale resolution. *Nat Meth* 2008, 5:1047-1052.

39. York AG, Ghitani A, Vaziri A, Davidson MW, Shroff H: Confined activation and subdiffractive localization enables whole-cell PALM with genetically expressed probes. *Nat Meth* , 8:327-333.

40. Shroff H, Galbraith CG, Galbraith JA, White H, Gillette J, Olenych S, Davidson MW, Betzig E: Dual-color superresolution imaging of genetically expressed probes within individual adhesion complexes. *Proceedings of the National Academy of Sciences* 2007, 104:20308-20313.

41. Donnert G, Keller J, Wurm CA, Rizzoli SO, Westphal V, Schonle A, Jahn R, Jakobs S, Eggeling C, Hell S: Two-Color Far-Field Fluorescence Nanoscopy. *Biophysical Journal* 2007, 92:L67-L69.

42. Berg H: *E. coli in motion*. Springer-Verlag New York, Inc; 2004.

43. Maddock Shapiro, L. J: Polar localization of the chemoreceptor complex in the E. coli cell. *Science* 1993, 259:1717-1723.

44. Sourjik, V, Berg H: Localization of components of the chemotaxis machinery of E. coli using fluorescent protein fusions. *Molecular Microbiology* 2000, 37:740-751.

45. Sourjik, V, Berg H: Functional interactions between receptors in bacterial chemotaxis. *Nature* 2004, 428:437-441.

46. Bray D: Bacterial chemotaxis and the question of gain. *Proceeding of the National Academy of Science* 2002, 99:7-9.

47. Bray Levin, M., Morton-Firth, C. D: Receptor clustering as a cellular mechanism to control sensitivity. *Nature* 1998, 393.

48. Erickson HP, Anderson DE, Osawa M: FtsZ in Bacterial Cytokinesis: Cytoskeleton and Force Generator All in One. 2010, 74:504-528.

49. Ma X, Ehrhardt D, Margolin W: Colocalization of cell division proteins FtsZ and FtsA to cytoskeletal structures in living Escherichia coli cells by using green fluorescent protein. 1996, 93:12998-13003.

50. Thanedar S, Margolin W: FtsZ Exhibits Rapid Movement and Oscillation Waves in Helix-like Patterns in Escherichia coli. 2004, 14:1167-1173.

51. Li Z, Trimble MJ, Brun YV, Jensen GJ: The structure of FtsZ filaments in vivo suggests a force-generating role in cell division. 2007, 26:4694-4708.

Chapter 2

Self-organization of the *E. coli* Chemotaxis System Imaged with Super-resolution Light Microscopy

The information presented in this chapter is adapted with permission from Greenfield D, McEvoy AL, Shroff H, Crooks GE, Wingreen NS, Betzig E, Liphardt J (2009). PLoS Biology **7** (6) e1000137 doi: 10.1371/jounal.p.bio.1000137

2.1 Summary

The *Escherichia coli* chemotaxis network is a model system for biological signal processing. In *E. coli*, transmembrane receptors responsible for signal transduction assemble into large clusters containing several thousand proteins. These sensory clusters have been observed at cell poles and future division sites. Despite extensive study, it remains unclear how chemotaxis clusters form, what controls cluster size and density, and how the cellular location of clusters is robustly maintained in growing and dividing cells. Here, we use photoactivated localization microscopy (PALM) to map the cellular locations of three proteins central to bacterial chemotaxis (the Tar receptor, CheY, and CheW) with a precision of 15 nm. We find that cluster sizes are approximately exponentially distributed, with no characteristic cluster size. One-third of Tar receptors are part of smaller lateral clusters and not of the large polar clusters. Analysis of the relative cellular locations of 1.1 million individual proteins (from 326 cells) suggests that clusters form via stochastic self-assembly. The super-resolution PALM maps of *E. coli* receptors support the notion that stochastic self-assembly can create and maintain approximately periodic structures in biological membranes, without direct cytoskeletal involvement or active transport.

2.2 Introduction

Efficient biological signal processing often requires complex spatial organization of the signaling machinery. Understanding how this spatial organization is generated, maintained and repaired inside cells is a fundamental theme of biology. A well understood signaling network with complex spatial organization is the bacterial chemotaxis system, which directs the movement of cells towards or away from sugars, amino acids, and many other soluble molecules [1]. In *Escherichia coli*, five types of transmembrane chemoreceptors form trimers of dimers [2,3], which cluster into large complexes containing tens of thousands of proteins [4-7]. Receptor clustering enables cooperative interactions between receptors [8-11], contributing to a bacterium's ability to sense nanomolar concentrations of chemicals and small fractional changes in chemical concentrations over a wide range [12-14]. Chemotaxis clusters are stabilized by the adaptor protein CheW and the histidine kinase CheA, which bind receptors in a ternary complex. CheA transduces signals from membrane receptors to the cytoplasmic response regulator CheY, which diffuses to flagellar motors and modulates their direction of rotation (Figure 2-1A; for review see [5]).

A variety of imaging studies have advanced our understanding of how the spatial organization of the chemotaxis network arises and contributes to function [15]. Time-lapse fluorescence microscopy suggests that receptors are inserted randomly into the lateral membrane via the general protein translocation machinery and then diffuse to existing clusters [16]. Immunoelectron and fluorescence microscopy have shown that receptor clusters are found at the cell poles [4] and future division sites [17].

Despite much research, the fundamental mechanisms responsible for positioning chemotaxis clusters at specific sites in the membrane remain unclear [15]. Perhaps cells possess intracellular structures that anchor clusters to periodic sites along cell length [17]. However, fluorescence microscopy of cells over-expressing all chemotaxis proteins showed that the number of clusters per cell saturates well below the number of proposed cluster anchoring sites. Furthermore, the distance between chemotaxis clusters varies broadly within cells [18]. Based on those observations, Thiem *et al*. have proposed that cluster nucleation and growth is a stochastic self-assembly process, in which receptors freely diffuse in the membrane and then join existing clusters or nucleate new clusters [18]. In their model, clusters nucleate anywhere in the membrane and later become attached to anchoring sites [18]. Shortly thereafter, it was reported that anchoring sites may not be required for periodic positioning; surprisingly, simulations reveal that periodic positioning of clusters can emerge spontaneously in growing cells [19].

Direct tests of these stochastic nucleation models involve measuring, as accurately as possible, the relative spatial positioning of clusters and the distribution of cluster sizes. This requires (I) the high specificity of genetically encoded fluorescent tags and (II) spatial resolutions sufficient to count and localize single proteins, even when these proteins are densely packed. Electron microscopy has the required spatial resolution but the density of immunogold labeling is too low to visualize a significant fraction of receptors [4]. Cryo-EM tomography has provided detailed information on large polar clusters [20,21], but identification of individual receptors is not yet possible. Fluorescence microscopy does not have the required spatial resolution to observe individual receptors in dense clusters. Single-cell Förster resonance energy transfer (FRET) studies have been instrumental in measuring the dynamics of signaling within the chemotaxis network [12,13], but cannot obtain the distribution of receptors inside cells.

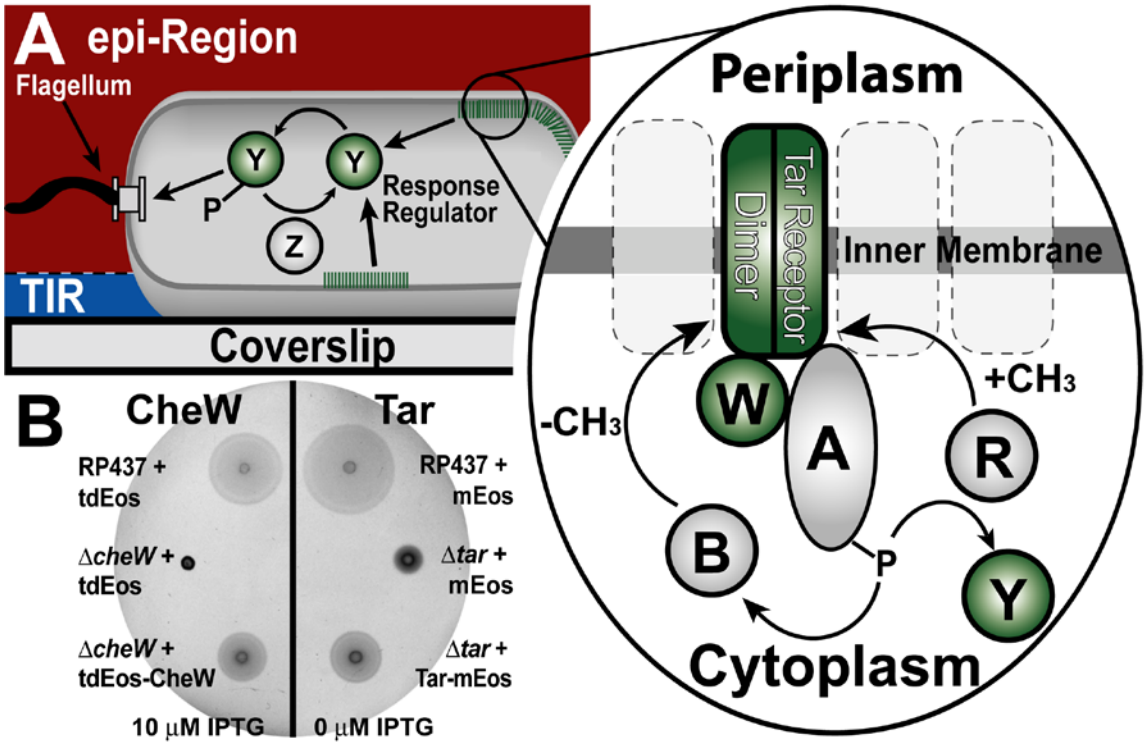

Figure 2-1. Membrane receptor clusters transduce chemotatic signals. (A) Schematic of *E. coli* cell imaged in PALM. Regions of the cell PALMed in TIR- and epi-illumination are shown. (zoom) Zoom of circled region denoted in (A) shows the chemotaxis signal transduction pathway. Proteins in green were labeled with Eos including a receptor dimer (Tar), CheW, and CheY. P denotes phosphate group and CH_3 is a methyl group. **(B)** Swarm plates show Eos-tagged chemotaxis proteins support chemotaxis. *E. coli* cells were spotted on minimal phosphate soft agar plates with 100 μM aspartate and ampicillin and allowed to swarm for 16-18 hours at 30 °C (Materials and Methods). Shown are wild-type RP437 cells containing only cytoplasmic Eos (positive control; top), knockout strains with cytoplasmic Eos (negative control; middle), and knockout strains complemented with Eos-tagged chemotaxis proteins (imaged cells; bottom). Complementation demonstrates that Eos-tagged proteins are partially functional, although not as efficient as the wild-type proteins. CheW (left) and Tar (right) fusion proteins support chemotaxis at 10 μM IPTG induction and no induction, respectively (Figure 2-2). Note that RP437 Δ*tar* cells are weakly chemotactic due to the presence of other receptors.

The optical super-resolution technique PALM combines high specificity with high resolution. In PALM, target proteins are genetically labeled with photoactivatable proteins, thus rendering them non-fluorescent until activated by near-UV light. By employing near-UV light of sufficiently low intensity, only one protein per diffraction-limited region (approximately 250 nm) is activated at a time. Following activation, each individual protein is then excited and imaged. Since only one protein is imaged at a time in each diffraction-limited region, the center of each molecular point spread function indicates the location of each protein [22]. Serial cycles of activation and excitation are repeated until all fusion proteins are bleached. Since individual proteins are imaged, we can count the number of proteins and computationally assemble the locations of all proteins into a composite, high-resolution image. The location of each protein can be determined to a precision of 2-25 nm, or 10-100x better than the diffraction limit [23-26]. The localization error in each protein location depends on the number of photons collected for that protein, as well as background noise, pixel size, sample drift, and whether cells are live or chemically fixed [22,23,26]. The highest optical resolution is obtained with chemically fixed cells [23]. Several other optical techniques including FPALM [27], STORM [28,29], STED [30-32], and SSIM [33] also image below the diffraction limit.

Here, we use PALM images to directly test stochastic nucleation models of chemotaxis cluster self-assembly in *E. coli*. We show that many receptors are part of small clusters not previously observed in EM or fluorescence microscopy, and that these small clusters provide direct evidence for a stochastic nucleation mechanism without anchoring sites.

2.3 Results and Discussion

PALM images of chemotaxis proteins.

Three main components of the bacterial chemotaxis network (Figure 2-1A) were visualized by constructing photoactivatable fluorescent protein fusions to Tar, CheW, and CheY (Figure 2-1A zoom). Tar is the high abundance aspartate receptor and makes up 30-45% of all receptors [34]. CheW is the adaptor protein, which binds all five types of chemotaxis receptors with variable stoichiometry. CheY is the chemotactic response regulator, which transduces signals from the receptors to flagellar motors. All fusion proteins were expressed from plasmids in strains lacking a genomic copy of the protein (Δ*tar* cells, Δ*cheW* cells, or Δ*cheY* cells) and therefore non-chemotactic unless complemented (with Tar, CheW, or CheY, respectively). Labeling several distinct components of the network and comparing their localization patterns ensures that there are no confounding effects of our tags on

clustering. All cells were cultured in H1, which is a defined minimal salts medium [35] that has been extensively characterized for its effects on chemotaxis protein expression [34].

Labeling of CheW and CheY.

CheW and CheY were labeled with tandem-dimer Eos (tdEos) [24,36], which is well characterized [24,26,37], bright [32], and has a contrast ratio between its on and off states sufficient to localize up to 10^5 proteins/μm^2 [26]. The addition of a fluorescent protein tag may affect the functionality of the original protein, therefore we measured the functionality of CheW and CheY fusions. Δ*cheW* cells expressing tdEos-CheW recover their chemotaxis ability in an inducer-dependent manner; at optimal induction, cells spotted on soft-agar swarm plates with attractant swarm to 77% of the diameter of wild-type cells (Figure 2-1B left; Figure 2-2). By contrast, Δ*cheY* cells expressing CheY-tdEos do not exhibit chemotaxis at any induction level, although the fusion protein does retain its ability to bind chemotaxis clusters (see below).

Labeling of Tar.

Tar was labeled with a new photoactivatable fluorescent protein, monomer Eos (mEos) [38]. Unlike the tdEos label, the mEos label does not abolish Tar function, perhaps due to its smaller size. Δ*tar* cells expressing Tar-mEos recover their chemotaxis ability toward aspartate; at optimal induction, cells spotted on soft-agar swarm plates with aspartate swarm to 55% of the diameter of wild-type cells (Figure 2-1B right; Figure 2-2).

Swarm plate assays of chemotaxis behavior suggest that the tdEos-CheW and Tar-mEos fusions retain some functionality, although they are not as efficient as wild-type CheW and Tar, respectively (Appendix I).

Microscopy.

Fields of fixed *E. coli* cells were imaged in four steps. First, we visualized the cells using differential interference contrast (DIC) microscopy (Figure 2-3A) and diffraction-limited epi-fluorescence (Figure 2-3B). To obtain a super-resolution PALM image, we photoactivated and individually localized single labeled proteins in total internal reflection (TIR) illumination (Figure 2-3C) until all proteins in the TIR volume (0-150 nm above the coverslip, Figure 2-1A) were bleached. To localize all remaining photoactivatable proteins, we used epi-illumination (Figures 2-1A and 2-3D). The use of epi-PALM in thin samples allows for imaging deeper into cells and discrimination between membrane and cytoplasmic structures. The TIR-PALM and epi-PALM data were superimposed to create a composite image (Figure 2-3E).

Unlike conventional microscopy (Figure 2-3B), PALM allowed us to see individual proteins (Figure 2-3F), count them (e.g. N = 241 Tar-mEos proteins, Figure 2-3G), and determine their location with a mean precision of 15 ± 9 nm (Appendix II). Given this spatial precision, we cannot discern an ordered molecular arrangement of receptor dimers (Appendix III). Overall, we detected on average 2770 Tar proteins, 1340 CheW proteins, and 6030 CheY proteins per cell (Figure 2-2A,E), consistent with native expression levels for all proteins.

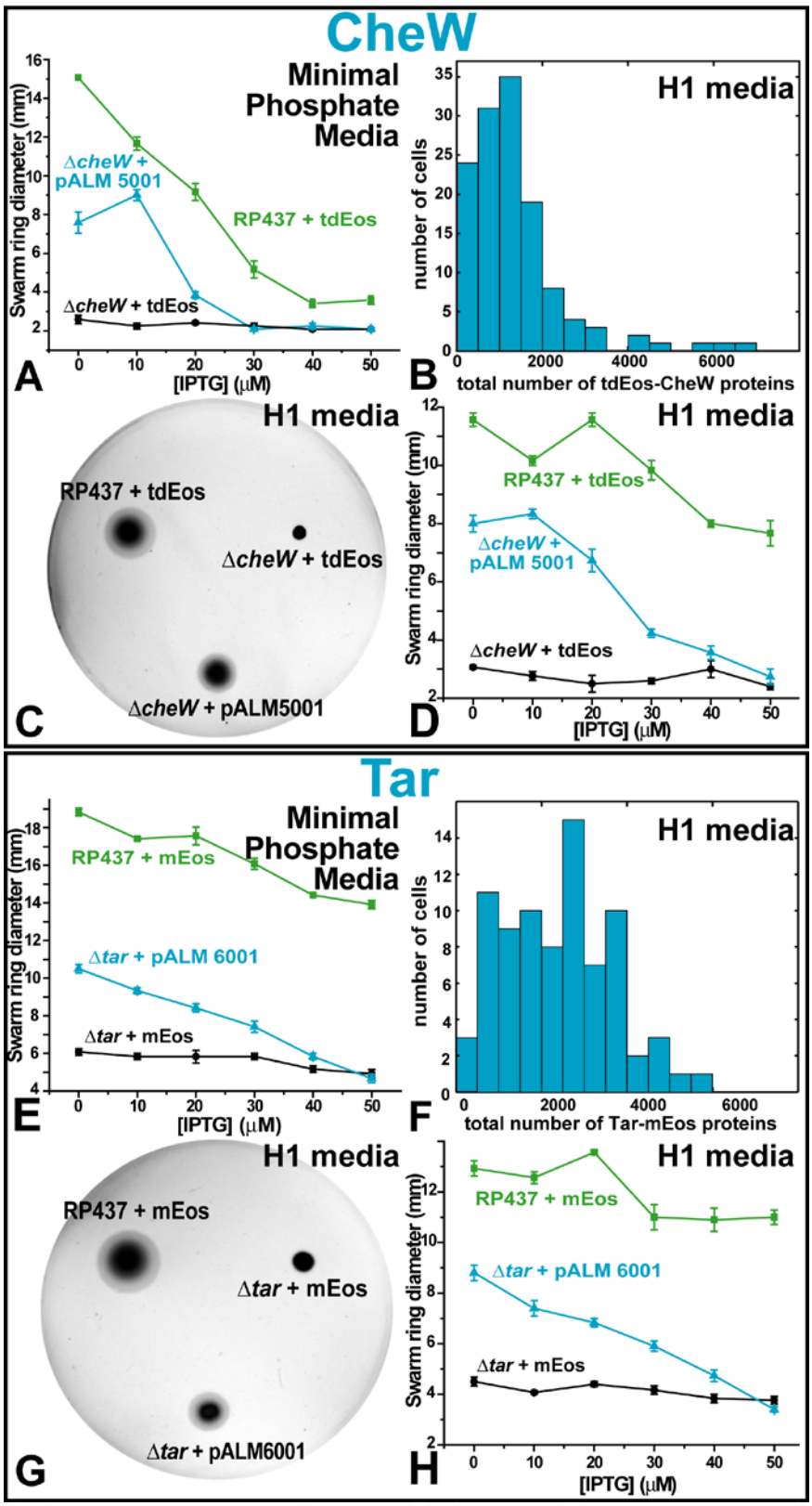
CheW
Minimal Phosphate Media
Swarm ring diameter (mm)
ΔcheW + pALM 5001
RP437 + tdEos
ΔcheW + tdEos
[IPTG] (μM)
A
H1 media
number of cells
total number of tdEos-CheW proteins
B
H1 media
RP437 + tdEos
ΔcheW + tdEos
ΔcheW + pALM5001
C
H1 media
RP437 + tdEos
ΔcheW + pALM 5001
ΔcheW + tdEos
[IPTG] (μM)
D
Tar
Minimal Phosphate Media
RP437 + mEos
Δtar + pALM 6001
Δtar + mEos
[IPTG] (μM)
E
H1 media
number of cells
total number of Tar-mEos proteins
F
H1 media
RP437 + mEos
Δtar + mEos
Δtar + pALM6001
G
H1 media
RP437 + mEos
Δtar + pALM 6001
Δtar + mEos
[IPTG] (μM)
H

Figure 2-2. Fluorescent fusion protein expression and functionality in *E. coli* cells. Shown are data for Eos-tagged CheW adaptor protein (top) and Eos-tagged Tar receptor (bottom). Cells were assayed in minimal phosphate media, a low ionic strength medium used for measuring chemotaxis on swarm plates [39], and also in H1 media, a high ionic strength medium previously used for quantifying chemotaxis protein expressions levels [34]. **(A and E)** To determine the optimal induction conditions for tagged CheW and Tar, cells were spotted on minimal phosphate swarm plates with aspartate, ampicillin, and varying concentrations of inducer IPTG. Chemotaxis fusion proteins (blue lines) complement chemotaxis in an inducer-dependent manner, with optimal induction 10 μM for CheW (A) and 0 μM for Tar (E), due to the leakiness of the *trc* promoter. **(B and F)** At optimal induction, the number of Eos-tagged CheW (B) and Tar (F) proteins per cell is similar to native expression level for both proteins [34]. Histograms were generated by counting proteins in PALM images of 130 CheW and 84 Tar cells. **(C and G)** Fusion proteins partially complement chemotaxis when grown on H1 imaging media plates supplemented with aspartate, ampicillin, and 10 μM IPTG (C) or 0 μM (G). **(D and H)** Optimal induction conditions for chemotaxis in H1 media are the same as in minimal phosphate media, demonstrating that cells are chemotactic when grown on imaging media. All errors are standard error of the mean for $N = 3$ plates. Swarm assays were performed according to Materials and Methods.

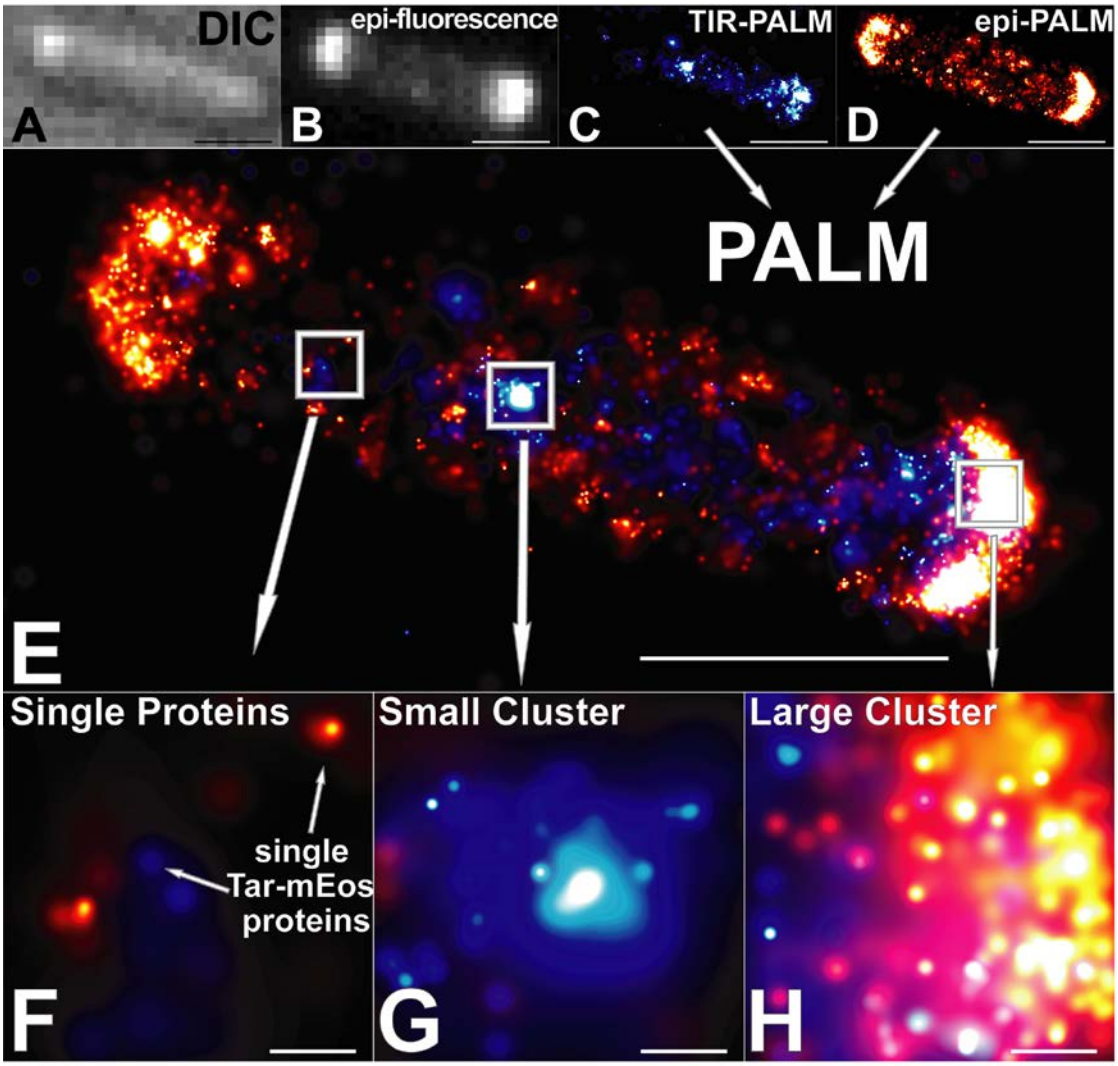

Figure 2-3. ***E. coli* Δ*tar* cell with mEos-labeled Tar. (A)** Differential Interference Contrast (DIC) image of a single cell. **(B)** Diffraction-limited epi-fluorescence. **(C)** PALM image in TIR-illumination. Each protein is represented as a 2D Gaussian distribution whose width is the positional error for that protein. **(D)** PALM image in epi-illumination, taken after Tar-mEos proteins in TIR region are bleached. **(E)** Superposition of C and D. **(F)** Zoom of single proteins (N = 44 Tar proteins) in left boxed region of (E). **(G)** Zoom of small cluster (N = 241 Tar proteins) in middle boxed region of (E). **(H)** Zoom of large polar cluster (N = 722 Tar proteins) in right boxed region in (E). Scale bar in (A-E) is 1 μm. Scale bar in (F-H) is 50 nm.

Like all other fluorescence techniques, PALM does not detect every labeled protein in a cell. For example, some fluorescent proteins will not fold properly, and consequently, PALM will not detect them. The fraction of detected labeled proteins depends on induction conditions, the cell strain, and fluorescence background, all of which are similar from cell to cell in a given experiment. In this paper, we report the number of labeled proteins that are photoactivatable, emit at least 100 photons, and can be localized to better than 40 nm (See Table 2-10 for image parameters). Despite our underestimate of the true number of proteins, the true number of the two functional constructs (Tar and CheW) in our cells must be within 2-3 times native copy numbers [20,40]. This is because over- or under-expression of Tar or CheW impairs chemotaxis, and these complemented cells are chemotactic.

Image analysis.

In total, we localized 1,069,281 individually labeled proteins from 326 *E. coli* cells (Figure 2-4). Unlike conventional microscopy, in which clusters are defined as the brightest features of an image, in PALM the location of each individual protein is known to within ~15 nm, and therefore the identification of clusters involves grouping based on interparticle separation. To objectively identify clusters, we used a tree-clustering algorithm, which groups closely spaced proteins (< 30 nm; twice the mean localization precision) into clusters in agreement with those identified by eye (Figure 2-5). We restricted our definition of clusters to 10 or more proteins to distinguish clusters from solitary receptors.

PALM images show numerous solitary Tar receptors (Figure 2-3F), small clusters consisting of tens or hundreds of receptors (Figure 2-3G), and also the large clusters with thousands of receptors (Figure2-3H) that are easily discerned in conventional fluorescence microscopy. Consistent with previous studies [4,17,41,42], the largest clusters are found predominantly at cell poles.

Strikingly, PALM images of all three strains (Tar, CheW, and CheY) revealed small lateral clusters and solitary receptors (Figure 2-6A-F) not previously observed. All cells contained a significant fraction of receptors within small clusters or as solitary receptors (Figure 2-6K). For example, 38% of labeled Tar receptors were found outside of large clusters (> 100 proteins). Most cells (~95%) contained between 1 and 48 small clusters (< 100 proteins) (Figures 2-6I-J). Small lateral clusters and solitary Tar receptors were observed in all expression conditions tested. When Tar-mEos was expressed at higher levels (1 mM IPTG induction), we saw banded patterns spanning the cell length (Figure 2-7) that may be helical structures reflecting the organization of the general protein translocation machinery, as previously observed [16]. Many small clusters and solitary receptors were present even at this higher level of expression.

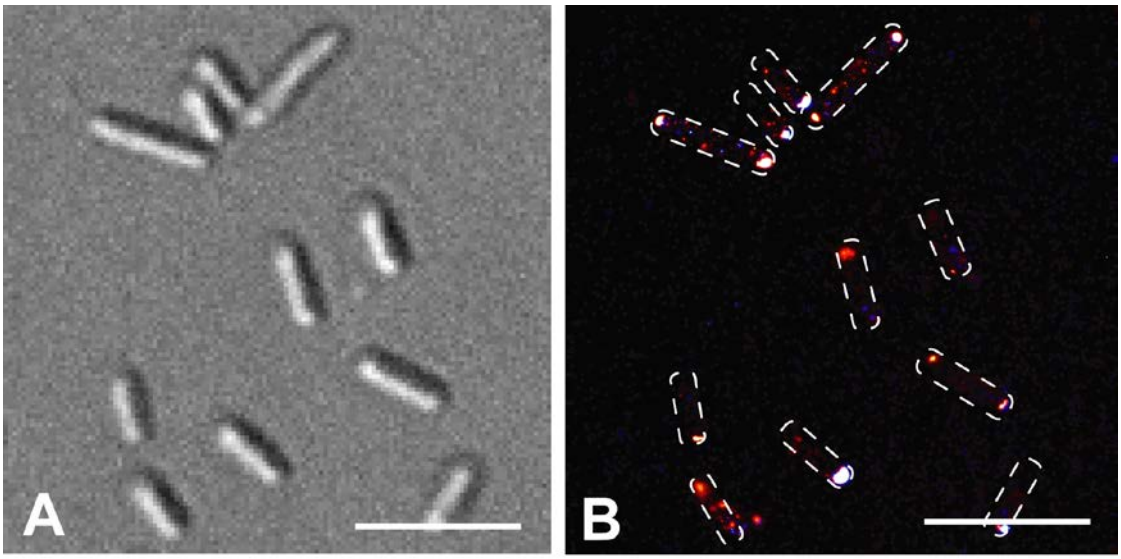

Figure 2-4. Many *E. coli* cells are imaged in one field of view using PALM. (A) DIC image of 11 cells attached to a poly-L-lysine coated sapphire coverslip. **(B)** Combined TIR- and epi-PALM image of *E. coli*. Dotted white lines are outlines of the cell bodies. Cells attached to the coverslip at both poles are stationary during imaging, therefore only these cells are used for analysis. White scale bars are 5 μm.

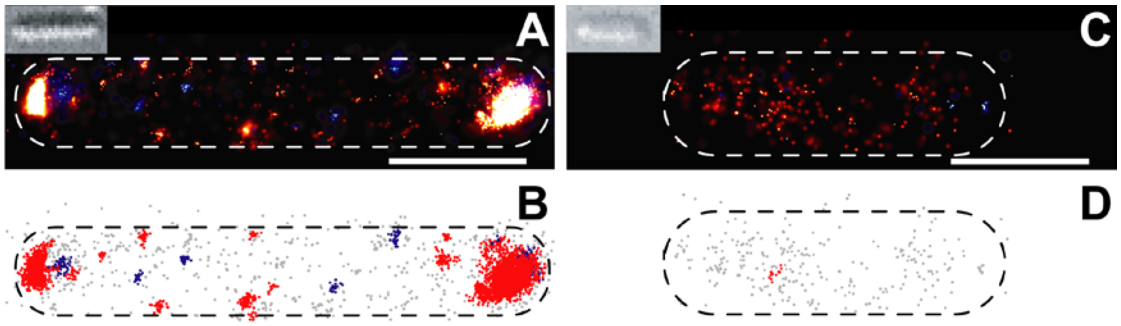

Figure 2-5. Clustering algorithm detects clusters in agreement with those detected by eye. (A) PALM image of single *E. coli* cell (RP437 Δ*cheW* + pALM5001) with a dotted white line representing the border of the cell body. Inset is a DIC image of the cell. **(B)** Demonstration of the clustering algorithm for the cell in (A). Clustering algorithm was used to segment clusters of fusion proteins within a cell. Individual fusion proteins determined to be less than 30 nm apart (twice the mean localization error) were grouped together into a cluster. Blue clusters are those in the TIR region, and red clusters are those in the epi-region. **(C)** PALM image of control cell (RP437 Δ*cheW* + pALM5000), which contains tdEos not fused to CheW. **(D)** Demonstration of the clustering algorithm for the cell in (C). Local high densities of proteins are occasionally grouped into false clusters (red), but these clusters are always < 100 proteins and comprise < 5% of total proteins within tdEos controls. Scale bars are 1 μm.

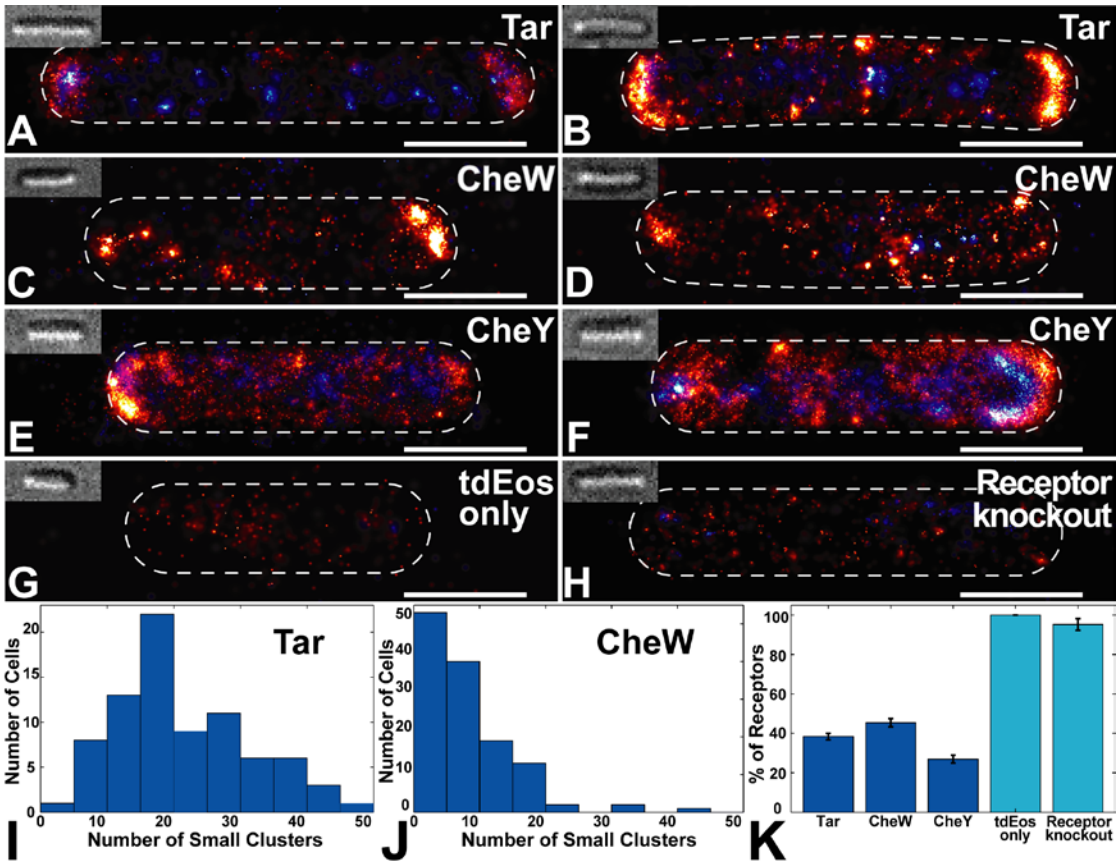

Figure 2-6. PALM images of single cells reveal small chemotaxis clusters. Single cell PALM images containing 3000-13000 labeled chemotaxis proteins per cell. Largest chemotaxis clusters are found at the poles, small lateral clusters are found in all cells. DIC images (inset) correspond to cell outlines (dashed lines). **(A-B)** Δ*tar* cells with pALM6001 (Tar-mEos). **(C-D)** Δ*cheW* cells with pALM 5001 (tdEos-CheW). **(E-F)** Δ*cheY* cells with pALM5003 (CheY-tdEos). Although CheY-tdEos does not support chemotaxis, its abundance in polar regions suggests it retains functional interactions with chemotaxis clusters. **(G)** Fluorescent reporter tdEos (pALM5000) does not form clusters without fusion to chemotaxis proteins. **(H)** tdEos-CheW does not form clusters in a receptor knockout strain. Scale bar in A-H is 1 μm. **(I-J)** Histograms of the number of small clusters (10-100 proteins) of Tar-mEos (I, N = 84 cells) or tdEos-CheW (J, N = 130 cells). **(K)** Percent of proteins that are found in small clusters (< 100 proteins) or as solitary receptors. Error is standard error of the mean.

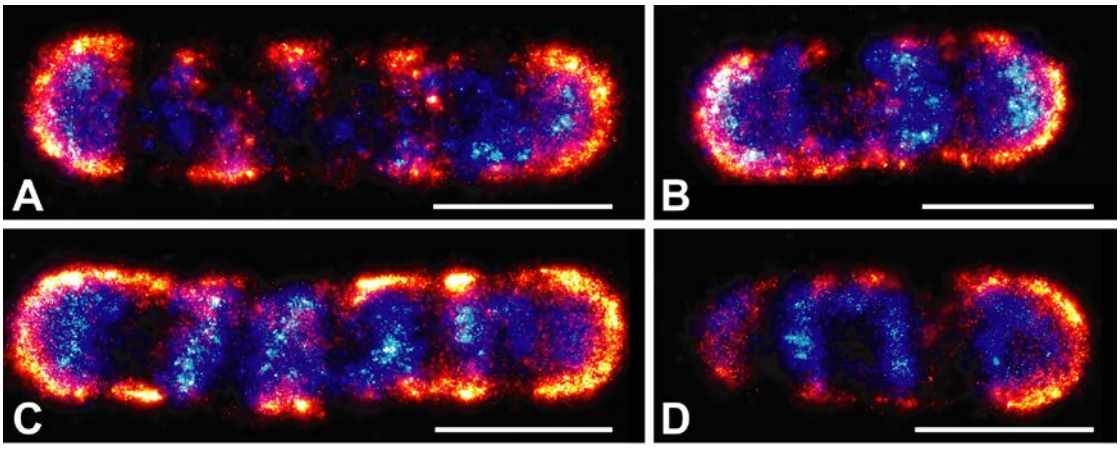

Figure 2-7. High levels of Tar-mEos expression show banded patterns. (A-D) Four single cells expressing Tar-mEos (RP437 Δ*tar* + pALM6001) exhibit putative helical structures with variable pitch. Structures may reflect a helical organization of the general protein translocation machinery. Cells were grown in H1 minimal media and induced with 1 mM IPTG for 3 hours. Cells contain high numbers of receptors (*N* = 31358, 30859, 47543, 15751 proteins for A-D, respectively). Scale bars are 1 μm.

The solitary receptors are not simply imaging artifacts, since our false-positive rate is only 1-10 proteins/μm^2; therefore 97 to 99.5% of observed signals are correctly labeled proteins (Appendix IV). Furthermore, the small clusters are not inclusion bodies or Eos aggregates, since tdEos alone exhibits no clustering (Figure 2-6G). Clustering of labeled CheW requires receptors since deletion of high-abundance chemotaxis receptors abrogated clustering of CheW (Figure 2-6H). Finally, a comparison between cells containing polarly localized fusion proteins (Figure 2-6A-F) and control cells (Figure 2-6G-H) indicates that observed clusters are not the result of proteolysis or degradation of fusion proteins that liberate the Eos tag.

The relative spatial positioning of clusters and the precise distribution of cluster sizes contain information about the mechanism of cluster formation. For example, the exponentially distributed sizes of rain drops reflect their spontaneous aggregation and growth [43]. By contrast, the Gaussian distribution of cell lengths in *E. coli* reflects the tightly regulated processes of growth and division [44].

We quantified the distribution of cluster sizes for both functional fusion proteins, Tar and CheW. Although labeled CheY appears to bind chemotaxis clusters (Figure 2-6E-F), we exclude it from further detailed analysis because it does not support functional chemotaxis, therefore its spatial organization may not reflect native CheY. Analysis of 225,016 individual CheW proteins in 1155 clusters and 313,937 individual Tar proteins in 2001 clusters revealed that cluster sizes were

distributed according to a stretched exponential (Figure 2-8A-B), consistent with stochastic self-assembly. This distribution is not an artifact of combining data from numerous cells, since individual cells feature the same distribution (Figure 2-9). Since the reported protein counts underestimate the true number of labeled proteins by a constant factor, the true distribution of cluster sizes is our measured distribution scaled by a constant factor. This scaling factor does not change the stretched exponential shape of the cluster-size distribution, merely the vertical scale. We note that the total number of receptors in each cluster is on average 2 to 3 times greater than the number of Tar receptors, because Tar comprises only 30-45% of the total number of receptors [34].

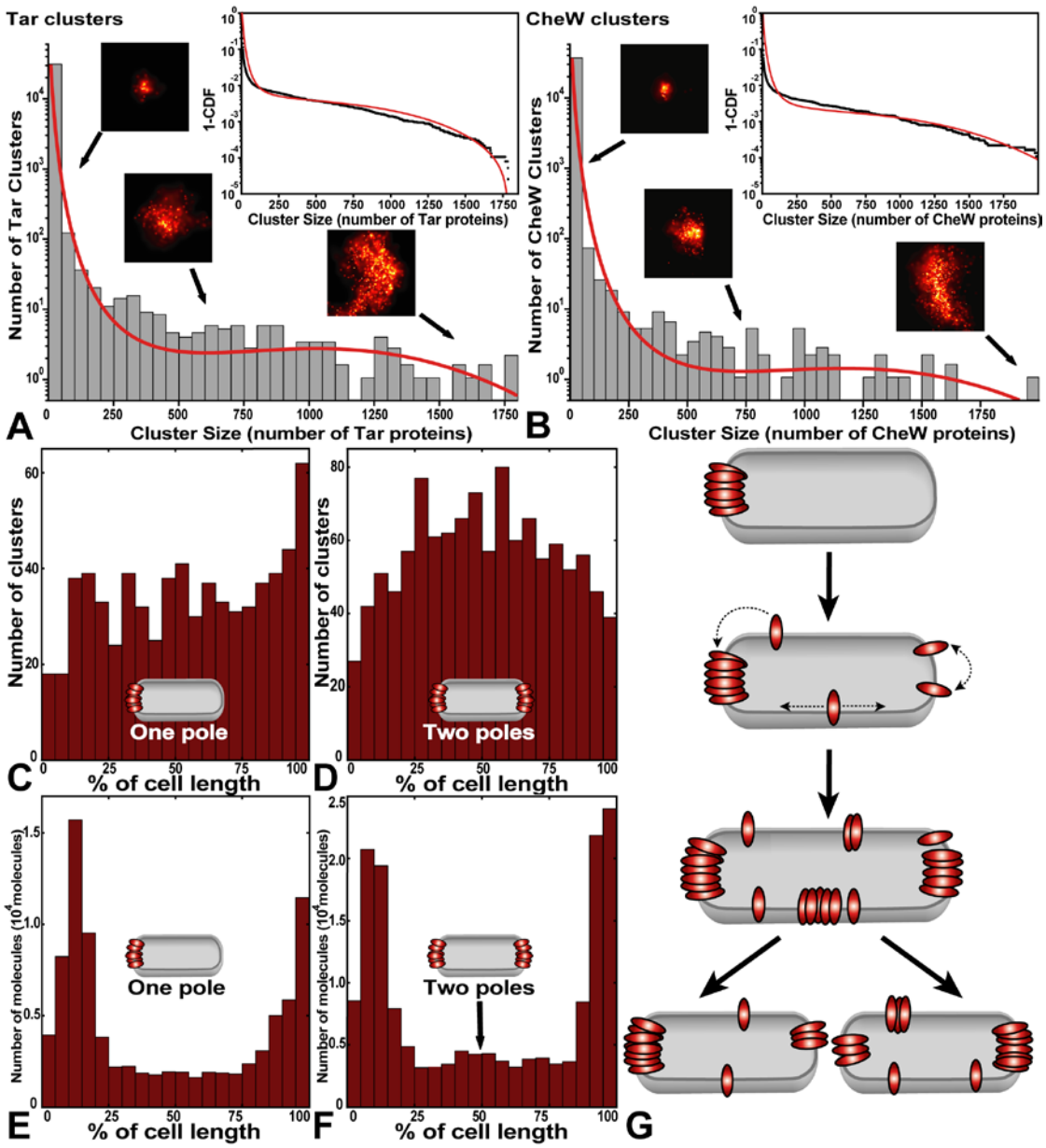
Tar clusters
Number of Tar Clusters
1-CDF
Cluster Size (number of Tar proteins)
A
CheW clusters
Number of CheW Clusters
Cluster Size (number of CheW proteins)
B
Number of clusters
One pole
% of cell length
C
Two poles
D
Number of molecules (10^4 molecules)
E
F
G

Figure 2-8. Chemotaxis cluster-size distribution and model. (A-B) Histograms of cluster size, measured by the number of closely spaced Eos-labeled Tar (A) and CheW (B) proteins. Smaller clusters occur much more frequently than larger clusters. Sample images of clusters are shown with arrows that indicate cluster size. To evaluate the fit in a bin-independent representation, we plot the cumulative distribution function (CDF) (insets). The fit of our self-assembly model to our data is shown in red. **(C-D)** Cells with one (C) or two (D) large polar clusters ($N \geq 400$ proteins) have the highest density of remaining smaller clusters ($N < 400$) furthest from the existing cluster(s). **(E-F)** Cells with two large polar clusters (F) exhibit higher Tar-receptor density at mid-cell (arrow) in comparison to cells with one polar cluster (E). $N = 31$ cells for (C, E) 38 cells for (D, F). **(G)** Model of receptor self-assembly in which cluster locations are maintained within a population of growing and dividing cells. Cluster nucleation is most likely to occur where receptor density is high, which occurs far from any existing cluster. Dotted arrows denote receptor diffusion within the membrane.

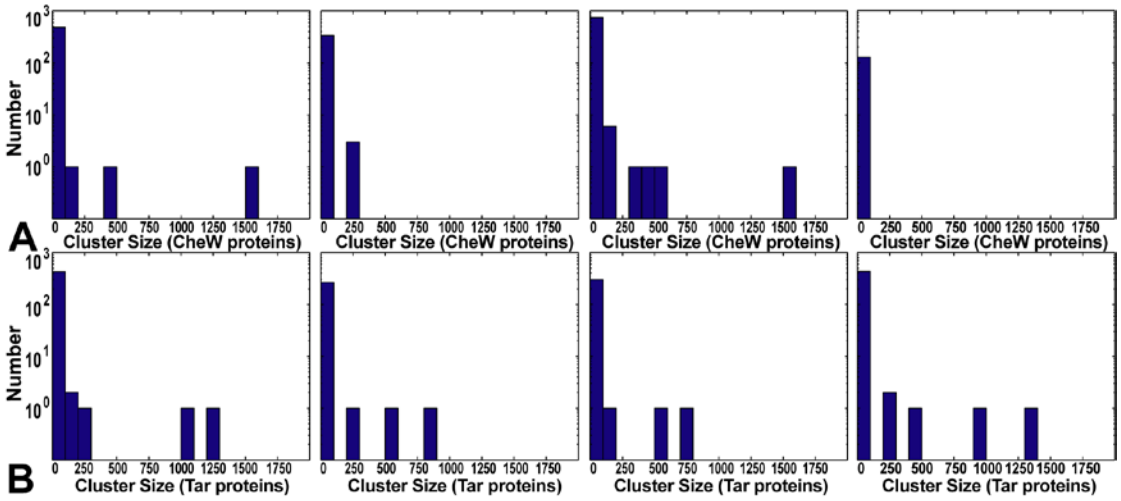

Figure 2-9. All cells contain more small clusters than large clusters. (A) Each panel shows the distribution tdEos-CheW cluster sizes in individual cells (4 cells total). **(B)** The Tar-mEos cluster-size distribution in individual cells (4 cells total). Each cell shows more single labeled proteins than large clusters, consistent with the distribution of the population (Figure 2-8A-B). Bins are 100 proteins.

2.4 An Extended Stochastic Nucleation Model

To understand how the distribution of cluster sizes may arise from a simple stochastic nucleation mechanism, we extended the cluster growth model of Wang *et al*. [19]. According to their model, receptors are inserted into the membrane at random locations and then diffuse until they are captured by a pre-existing cluster or nucleate a new cluster. The growth of a specific cluster depends on competition for receptors with nearby clusters. In our model, we treat the competing clusters as an absorbing barrier a distance R away from a pre-existing cluster of radius a, which is also absorbing (see also Chapter 5). The rate of growth of a cluster is given by $\frac{dN}{dt} = \pi\gamma\left[\frac{1}{2}\frac{(R^2-a^2)}{\ln(R/a)} - a^2\right]$, which depends only on R, a, and γ, the deposition rate of the receptors into the membrane. Integrating $\frac{dN}{dt}$ relates the size of a cluster with its age t_{age}. In an exponentially growing population of cells, the ages of the clusters will be exponentially distributed according to $P(t_{age}) = \frac{1}{\tau}e^{-t_{age}/\tau}$, where $1/\tau$ is the growth rate of the cells. Assuming that receptors diffuse freely in the membrane but clusters are stationary, we predict that the probability of a cell containing a cluster of size N is

$$P(N) \approx \frac{2}{\tau\alpha}\left[\ln(R) - \ln\sqrt{N\Delta A/\pi}\,\right]e^{-\left[(\beta+1)(N-N_0)-N\ln(N)+N_0\ln(N_0)\right]/\alpha\tau}, \quad (1)$$

where we have defined the constants $\alpha = \pi\gamma R^2$ and $\beta = 2\ln(R) - \ln(\Delta A/\pi)$, and where N is the number of receptors (or receptor dimers), N_0 is the number of receptors at nucleation, and ΔA is the area per receptor (see Chapter 5 for details).

In the cell membrane, small clusters would be expected to diffuse and occasionally combine with other clusters. To account for this attrition of small clusters, we modify $P(N)$ by multiplying it by a survival probability, such that the total probability of observing a cluster of size N receptors is $P_{tot}(N) = P(N)\,P_{surv}(N)$. We calculate the survival probability to be

$$P_{surv}(N) = e^{\frac{-kT}{8\pi\eta h R^2\alpha}\left[N(\ln N)^2+(c+\beta-2)(N\ln N - N_0\ln N_0)+(\beta c-\beta-c+2)(N-N_0)-N_0(\ln N_0)^2\right]}, \quad (2)$$

where η is the viscosity of the membrane, h is the thickness of the membrane, and c is a constant set by the dimensions of the cell and the area per receptor (see Chapter 3). Combining Eqs. 1 and 2 results in an expression with the functional form

$$P_{tot}(N) \approx c_1 e^{-c_2 N + c_3 N\ln(N) - c_4 N(\ln(N))^2}, \quad (3)$$

which we use to fit our cluster-size distributions with free parameters c_2, c_3, and c_4. Normalizing each cluster-size distribution fixes the constant c_1.

Eq. 3 fits our observed cluster-size distribution well (Figure 2-8A-B, red line), consistent with a stochastic cluster growth and nucleation mechanism. To evaluate the fit of our model to our data in a bin-independent manner, we compared the cumulative distribution function (CDF) of our cluster-size distribution with the CDF of our model (Figure 2-8A-B, insets). Importantly, our cluster growth model does not invoke cluster anchoring to cytoskeletal or pre-divisional structures, nor does it require active transport of receptors or clusters.

2.5 Additional Evidence for Stochastic Nucleation

To provide further, independent, support that receptors stochastically self-assemble into clusters, we analyzed another aspect of the data. In our model, proteins that happen to be inserted close to existing clusters will be absorbed by them, whereas those inserted far from existing clusters will nucleate new clusters [19]. Thus, our model predicts that the highest density of small clusters will be found predominantly at sites that are furthest from all existing large clusters.

We identified cells with one or two large polar clusters (≥ 400 proteins) and measured the locations of small clusters (< 400 proteins) within these cells. As predicted by our model, cells with one large polar cluster have the highest remaining cluster density at the opposite end of the cell (Figure 2-8C). Moreover, cells with two polar clusters have the highest cluster density in the middle of the cell, furthest from the two large clusters (Figure 2-8D). To ensure these results were not affected by our definition of clusters, we performed a similar analysis with receptor density. Cells with two polar clusters have significantly higher receptor density in the middle of the cells (Figure 2-8F arrow) in comparison to cells with only one polar cluster (Figure 2-8E) (two-sample Kolmogorov-Smirnov test, p = 0.00013, N = 9115, 19967 proteins, middle 25% of cell length). These results are robust to changes in the specific size cut-off for large polar clusters.

Our data and modeling (Figures 2-8A-F) directly support a stochastic nucleation mechanism of cluster assembly and positioning. In addition to explaining how the exponential distribution of cluster sizes arises, the model also sheds light on the mechanism for spatial self-organization along cell length, in the particular manner shown in Figure 2-8G and also detected by diffraction-limited imaging [17]. As cells grow, new clusters form primarily at locations that are furthest from large existing clusters. This is because the density of solitary receptors (or receptor dimers) is highest in regions furthest from existing clusters. A cell with one polar cluster will

tend to form the next large cluster at the opposite pole, yielding a cell with clusters at both poles. A cell with clusters at both poles will tend to form new clusters at the cell midline, the location furthest from both poles.

In addition to generating clusters, receptor self-assembly may maintain and repair the location of clusters inside cells. In the event that a daughter cell begins without a large cluster, the first new cluster will form at a random location, but subsequent clusters nucleate furthest from that first cluster, at one of the cell poles. Furthermore, new membrane and cell wall are inserted into lateral regions of the cell [45], so that cell growth and division will eventually reposition lateral clusters at the cell poles. In this way, cells that begin without clusters will generate periodic positioning of new clusters along cell length as well as the particular exponential distribution of cluster sizes detected by PALM (Figure 2-8A-B). The mechanism of stochastic cluster formation allows cells to recover from the loss of all clusters, as well as begin to correctly position clusters soon after growth in new media. We note that our model does not address the reported difference in diffusion rates between polar and lateral clusters [17]. It is possible that the difference in membrane curvature or membrane composition between polar and lateral regions affects cluster diffusion or cluster dynamics.

There may be multiple advantages to arranging a fixed number of receptors among a variety of cluster sizes, such as fine-tuning of signal processing [46]. Our PALM images of receptors are reminiscent of the model of Berg and Purcell [47] who theorized that for optimum detection sensitivity, membrane receptors should be dispersed widely over the surface of the cell rather than concentrated in one location. In addition, recent *in vitro* data suggest that different densities of receptors have different kinase and methylation rates [48] suggesting that the chemotaxis network may adjust its kinase activity based on the local concentration of receptors.

Recent *in vitro* evidence shows that purified membrane-associated proteins can spontaneously self-assemble into complex, dynamic structures [49,50]. Our super-resolution PALM maps of *E. coli* receptors support this notion that stochastic self-assembly can create and maintain dynamic patterns in biological membranes, without direct cytoskeletal involvement or active transport. Perhaps stochastic self-assembly is the simplest mechanism to produce robust patterns in membranes without additional machinery. Our model may apply to clustering of other proteins and to chemotaxis receptors in other organisms, however many details are expected to be organism-specific. Analysis of super-resolution images similar to those presented here will allow counting of proteins and complexes in individual cells, reveal new levels of cell organization, and allow mechanistic hypotheses to be directly tested.

Figure	F_{TIR}	P_{TIRF}	F_{epi}	P_{epi}	*pixelsize*	*gain*
2-3C	83498	1679	n/a	n/a	4	5×10^4
2-3D	n/a	n/a	83169	3936	4	5×10^4
2-3E	83498	113	83169	1187	1	5×10^4
2-3F	83498	22	83169	22	0.25	8×10^3
2-3G	83498	217	83169	24	0.25	8×10^3
2-3H	83498	229	83169	493	0.25	8×10^3
2-4B	59600	31493	79032	54910	10	40
2-5A	59600	662	79032	3982	2.5	3.2×10^3
2-5C	12335	25	35786	264	2.5	3.2×10^3
2-6A	83498	1779	83169	1478	2.5	8×10^3
2-6B	83498	1530	83169	5357	2.5	8×10^3
2-6C	59600	271	79032	1613	2.5	2.5×10^4
2-6D	64638	313	89917	1413	2.5	2.5×10^4
2-6E	125757	2450	100369	5344	2.5	8×10^3
2-6F	94808	5358	98755	7690	2.5	8×10^3
2-6G	12335	94	35786	331	2.5	8×10^4
2-6H	57986	289	102677	708	2.5	8×10^4
2-7A	183784	12881	122083	18477	2.5	5×10^3
2-7B	183784	16836	122083	14023	2.5	5×10^3
2-7C	183784	21087	122083	26456	2.5	5×10^3
2-7D	183784	7890	122083	7861	2.5	5×10^3
2-8A left	n/a	n/a	95706	s103	0.5	4×10^4
2-8A mid	n/a	n/a	83169	605	0.5	3×10^4
2-8A right	n/a	n/a	95706	1663	0.5	3×10^3
2-8B left	n/a	n/a	79032	137	0.5	3×10^3
2-8B mid	n/a	n/a	88903	673	0.5	2×10^3
2-8B right	n/a	n/a	102388	1814	0.5	2×10^3

Table 2-10. Parameters of merit for the acquisition and analysis of PALM images. F_{TIR} and F_{epi} = total number of acquired frames in the image stack in TIR and epi illumination, respectively; P_{TIRF} and P_{epi} = total number of proteins localized from the data in the image stack in TIR and epi illumination, respectively; *pixelsize* = size of each pixel (in nm) in the rendered image; *gain* = multiplies the value in the original probability density map ([0,1] for a single protein) to obtain a value suitable for display ([0,255] for a colormap with 256 intensities). Note that the gain is normalized for pixelsize before rendering.

2.6 Materials and Methods

Bacterial Strains and Plasmids.

All strains are derivatives of RP437, a chemotactic wildtype *E. coli* K-12 strain. Each chemotaxis protein was expressed in a strain lacking the genomic copy of that protein. All proteins were expressed from the inducible *trc* promoter on the medium-copy plasmid pTrc-His2 (Invitrogen, Carlsbad CA) containing a pBR322-derived origin, the ampicillin resistance gene (*bla*), and the lac repressor ($lacI^q$). The receptor knockout strain is HCB436 [51], which lacks all chemoreceptors except Aer and also lacks the adaptation enzymes CheR and CheB. pALM5000 contains the tandem dimer Eos (*tdEos*) gene only, and pALM6000 contains the monomer Eos (*mEos*) gene only. pALM5001, pALM5003, and pALM6001 contain *tdEos-cheW*, *cheY-tdEos*, and *tar-mEos* gene fusions, respectively.

Photoactivatable Proteins.

Eos is a photoconvertible protein that irreversibly switches its peak emission from green (516 nm) to red (581 nm) upon exposure to near-UV light [36]. Eos consists of 226 amino acids with a molecular mass of 26 kDa. Tandem dimer Eos (tdEos) consists of two copies of wild-type Eos [36] connected by a 15 residue linker SRGHGTGSTGSGSSE (Nucleotide sequence TCTCGAGGTCACGGTACTGGTTCTACTGGTTCTGGTTCTTCTGAG). Monomer Eos (*mEos*) is the improved monomeric photostable "mEos2" from McKinney *et al.* [38].

Fusion Proteins.

The tandem dimer Eos (*tdEos*) gene on plasmid pALM5000 is followed by the residues ENSGS (nucleotides GAGAATTCGGGATCC) containing a BamHI site. The *tdEos-cheW* gene on plasmid pALM5001 consists of *tdEos*, a five residue linker (ENSGS), the entire *cheW* gene (residues 1-167), and a terminal Gly-Ser encoding a BamHI site. The *cheY-tdEos* gene on plasmid pALM5003 consists of the entire *cheY* gene (residues 1-129), a one residue linker Ala encoding part of a NcoI site, *tdEos*, and ENSGS. The monomer Eos gene (*mEos*) on plasmid pALM6000 is followed by Gly-Ser. The *tar-mEos* gene on plasmid pALM6001 consists of the entire *tar* gene (residues 1-553) joined to *mEos* with no linker, followed by Gly-Ser. The *tar* gene second codon was mutated from ATT (Ile) to GTA (Val) to introduce a NcoI site.

Plasmid Construction.

Plasmid pALM5000 was constructed by PCR amplification of the tandem dimer *Eos* gene from the plasmid ptdEos-Vinculin [26] using primers 5'-

ACCATGGTGGCGATTAAGC-3′ and 5′-TTAGGATCCCGAATTCTCTCGTCTGGCATTGTC-3′ containing underlined NcoI and BamHI sites, respectively. This PCR product was inserted into plasmid pTrc-His2 (Invitrogen) according to the manufacturer's instructions. The N-terminal plasmid leader sequence was removed by digestion with NcoI and re-ligation. pALM5001 (tdEos-CheW) was constructed by PCR amplification of *cheW* from strain RP437 using primers 5′-AAAGGTGGATCCATGACCGGTATGACGAATGTAAC-3′ and 5′-TCGGGAGGATCCCGCCACTTCTGACG-3′ and cloned into the BamHI site of pALM5000, immediately after the *tdEos* gene. pALM5003 (CheY-tdEos) was constructed by PCR amplification of *cheY* from strain RP437 using primers 5′-AGTGTGCCATGGCGGATAAAG-3′ and 5′-AGTCGCCCATGGCCATGCCCAGTTTC-3′ and cloned into the NcoI site in pALM5000, immediately before the *tdEos* gene. pALM6000 was constructed by PCR amplification of the monomeric *Eos* gene from plasmid pRSETa_mEos2 (Addgene plasmid 20341) using primers 5′- GGATCCATGGGGGCGATTAAGCCAGAC-3′ and 5′-CAAGCTTCTTAGGATCCTCGTCTGGCATTGTCAGGC-3′ containing underlined NcoI and BamHI sites, respectively. This PCR product was cloned into pALM5000, replacing *tdEos* with *mEos*. pALM6001 (Tar-mEos) was constructed by cloning a 2345 bp synthesized DNA (DNA 2.0, Menlo Park CA) into the NcoI and BamHI sites of pALM5000, replacing *tdEos* with *tar-mEos*. The synthetic DNA coded for the *tar* gene of wild-type strain MG1655 immediately followed by the monomer *Eos* gene, and the entire sequence was flanked by appropriate restriction sites. These restriction sites added a terminal Gly-Ser to the *Eos* gene.

Strain Construction.

RP437 Δ*cheW* and RP437 Δ*tar* were made by P1 transduction from the Keio collection strains JW1876 (Δ*cheW::kan*) and JW1875 (Δ*tar::kan*), respectively. The deletions in these strains were constructed to minimize polar effects on downstream gene expression by retaining the native start codon and the last 18 C-terminal nucleotides [52]. When cured of kanamycin resistance, the Keio deletion strains retain a translatable scar sequence in-frame with the deleted gene initiation codon and its C-terminal 18-nt coding region. This scar sequence is expected to produce a 34-residue scar peptide with an N-terminal Met, 27 scar-specific residues, and six C-terminal gene-specific residues. RP437 Δ*cheY* was made according to Datsenko and Wanner [53] using primers that exactly removed the entire cheY gene and replaced it with a 1.1 kb DNA from pKD3 encoding the chloramphenicol resistance gene. Strains were cured of resistances using plasmid pCP20 as described in Cherepanov and Wackernagel [54].

Media.

Tryptone broth (T-broth) contains 1% w/v Difco Bacto-Tryptone (Becton Dickinson and Company, Sparks, MD), and 0.5% w/v NaCl (Fisher-Scientific), pH 7.0. H1 minimal media [35] contains 100 mM potassium phosphate pH 7.0 (11.2 g/L K_2HPO_4 anhydrous, 4.8 g/L KH_2PO_4), 15 mM $(NH_4)_2SO_4$, 1 mM $MgSO_4$, 2 μM $Fe_2(SO_4)_3$, with 0.5% glycerol and 1 mM required amino acids (histidine, leucine, methionine, and threonine). Minimal phosphate media [39] contains 10 mM potassium phosphate (pH 7.0), 1 mM $(NH_4)_2SO_4$, 1 mM $MgSO_4$, 1 mM glycerol, and 0.1 mM required amino acids. Media were supplemented with 50 μg/mL ampicillin (Shelton Scientific, Shelton, CT).

Cell Culture.

Cultures were grown overnight in T-broth at 30 °C with aeration. Day cultures were inoculated to an optical density (OD) at 600 nm of ~0.01 into H1 minimal media with appropriate antibiotics at 30 °C with aeration until they reached an OD600 0.1 – 0.3. Protein expression, when indicated, was induced by adding 10 μM IPTG for 3 hours. Media and temperature were chosen to obtain the highest expression levels of properly folded proteins [36,55].

Swarm Plate Assay.

To determine functionality of chemotaxis fusion proteins, 2 μL of stationary phase cells were spotted on soft-agar swarm plates and incubated at 30 °C for 16-18 hours. Wild-type cells containing cytoplasmic Eos (positive control) were compared with appropriate deletion strains containing cytoplasmic Eos (negative control) and deletion strains with Eos-tagged chemotaxis fusions (cells used for imaging). All cells contain plasmids derived from pTrc-His2 which confers ampicillin resistance. Swarm plates contain 0.3% agar (Becton-Dickinson) in 10 mM minimal phosphate media (or H1 media) supplemented with 100 μM aspartate, 50 μg/mL ampicillin, and varying concentrations of IPTG. Aspartate was added to the plates to ensure that complemented mutants display chemotaxis toward aspartate, since RP437 Δ*tar* still contains the remaining four receptors which are capable of chemotaxis toward serine and oxygen. Cells were grown in tryptone broth with ampicillin at 30 °C prior to spotting on swarm plates.

Sapphire Coverslip Cleaning.

Sapphire coverslips used for their high refractive index (Olympus APO100X-CG) were placed in a 5:1:1 solution of Milli-Q filtered water, ammonium hydroxide and hydrogen peroxide overnight at 75 °C. They were subsequently rinsed with filtered water, sonicated in acetone for 20 minutes, rinsed again with water, rinsed

with methanol, dried quickly under air flow, passed through a flame, and stored dry until use.

Sample Preparation.

Clean sapphire coverslips were covered in 0.05% w/v poly-L-lysine for 30 minutes then rinsed with water. Cells were added and allowed to settle for 30 minutes at room temperature in the dark or spun onto coverslips at 2000 g for 10 minutes. Cells were fixed with 4% paraformaldehyde in 10 mM PBS (pH 7.4) for 15 minutes at room temperature. Fixative solution was prepared daily by mixing 0.8 g paraformaldehyde, 18 mL water, and 20 uL of 10 N NaOH, then dissolved by heating to ~50 °C for several minutes with stirring, buffered to pH 7.4 with the addition of 2 mL 10x PBS solution and 140 uL 1 N HCl, and finally filtered. After fixation cells were rinsed with PBS. To compensate for drift during imaging [26], a 40x dilution of 40 nm and 100 nm Au beads (Microspheres-Nanospheres, 790114-010 and 790122-010) were added.

PALM Instrumentation.

PALM imaging was performed according to Shroff et al. [24] on an Olympus IX81 inverted microscope equipped with DIC optics and a 100x, 1.65 NA objective. Laser light was delivered to the microscope through free space from a platform where 405 nm, 488 nm, and 561 nm lasers were combined. Single-molecule tdEos and mEos fluorescence signals generated during acquisition were separated from the activation and excitation light using appropriate filter sets [24] within the microscope and passed to an electron-multiplying CCD camera running at ~20 Hz (50 ms exposures). Movie acquisition times were dependent on the region of highest labeled-protein density, which are the largest chemotaxis clusters. Activation intensity was increased slowly such that a given diffraction-limited spot contained no activated proteins > 90% of the time. This is necessary to ensure that only one protein is activated at a time in a single diffraction-limited spot. Image generation and data analysis were done using custom Matlab scripts (Mathworks, Natick, MA). Acquisition times were 30-180 minutes for TIR, and 90-240 minutes for epi illumination.

PALM Analysis.

Localization and image-rendering algorithms have been described [26]. Briefly, images were filtered and proteins were identified as signals that contained counts larger than 4 standard deviations above background. Proteins which became dark but reappeared within 5 frames were counted as the same protein. Only proteins which emitted at least 100 photons and had localization errors less than 40

nm were counted, and these thresholds were chosen to maximize the signal to noise for our images and minimize false positives (Figure 2-10). Sample drift was corrected by tracking the motion of fiducial nanoparticles, which were localized at ~1 Hz to better than 1 nm precision. Images from the TIR, epi, DIC and bright field channels were aligned by recording the position of fiducial nanoparticles common to all channels. All epi-PALM images were rendered with the 'hot' colormap in Matlab that varies smoothly from black through shades of red, orange, and yellow to white, and TIR-PALM images were rendered with a variation of the same colormap with red and blue channels switched.

2.7 References

1. Adler J (1975) Chemotaxis in bacteria. Annual Reviews of Biochemistry 44: 341-356.

2. Ames P, Studdert C, Reiser R, Parkinson J (2002) Collaborative signaling by mixed chemoreceptor teams in *Escherichia coli*. Proceeding of the National Academy of Science 99: 7060-7065.

3. Kim KK, Yokota H, Kim S-H (1999) Four-helical-bundle structure of the cytoplasmic domain of a serine chemotaxis receptor. Nature 400: 787-792.

4. Maddock J, Shapiro L (1993) Polar localization of the chemoreceptor complex in the *E. coli* cell. Science 259: 1717-1723.

5. Baker M, Wolanin P, Stock J (2006) Signal transduction in bacterial chemotaxis. BioEssays 28: 9-22.

6. Martin A, Wadhams G, Armitage J (2001) The roles of the multiple CheW and CheA homologues in chemotaxis and in chemoreceptor localization in Rhodobacter sphaeroides. Molecular Microbiology 40: 1261-1272.

7. Gestwicki J, Lamanna A, Harshey R, McCarter L, Kiessling L, et al. (2000) Evolutionary conservation of methyl-accepting chemotaxis protein location in *Bacteria* and *Archaea*. Journal of Bacteriology 182: 6499-6502.

8. Lybarger S, Maddock J (1999) Clustering of the chemoreceptor complex in *E. coli* is independent of the methyltransferase CheR and the methylesterase CheB. Journal of Bacteriology 181: 5527-5529.

9. Skidmore J, Ellefson D, McNamara B, Couto M, Wolfe A, et al. (2000) Polar clustering of the chemoreceptor complex in *E. coli* occurs in the absences of complete CheA function. Journal of Bacteriology 182: 967-973.

10. Vaknin A, Berg H (2006) Osmotic stress mechanically perturbs chemoreceptors in *E. coli*. Proceeding of the National Academy of Science 103: 592-596.

11. Vaknin A, Berg H (2007) Physical responses of bacterial chemoreceptors. Journal of Molecular Biology 366: 1416-1423.

12. Sourjik V, Berg H (2002) Receptor sensitivity in bacterial chemotaxis. Proceeding of the National Academy of Science 99: 123-127.

13. Sourjik V, Berg H (2004) Functional interactions between receptors in bacterial chemotaxis. Nature 428: 437-441.

14. Mesibov R, Ordal GW, Adler J (1973) The range of attractant concentrations for bacterial chemotaxis and the threshold and size of response over this range. Weber law related phenomena. Journal of General Physiology 62: 203-223.

15. Kentner D, Sourjik V (2006) Spatial organization of the bacterial chemotaxis system. Current Opinion in Microbiology 9: 619-624.

16. Shiomi D, Yoshimoto M, Homma M, Kawagishi I (2006) Helical distribution of the bacterial chemoreceptor via colocalization with the Sec protein translocation machinery. Molecular Microbiology 60: 894-906.

17. Thiem S, Kentner D, Sourjik V (2007) Positioning of chemosensory clusters in *E. coli* and its relation to cell division. EMBO Journal 26: 1615-1623.

18. Thiem S, Sourjik V (2008) Stochastic assembly of chemoreceptor clusters in *Escherichia coli*. Molecular Microbiology 68: 1228-1236.

19. Wang H, Wingreen NS, Mukhopadhyay R (2008) Self-Organized Periodicity of Protein Clusters in Growing Bacteria. Physical Review Letters 101: 218101.

20. Zhang P, Khursigara C, Hartnell L, Subramaniam S (2007) Direct visualization of *E. coli* chemotaxis receptor arrays using cryo-electron microscopy. Proceeding of the National Academy of Science 104: 3777-3781.

21. Briegel A, Ding HJ, Li Z, Werner J, Gitai Z, et al. (2008) Location and architecture of the *Caulobacter crescentus* chemoreceptor array. Molecular Microbiology 69: 30-41.

22. Thompson RE, Larson DR, Webb W (2002) Precise nanometer localization analysis for individual fluorescent probes. Biophysical Journal 82: 2775-2783.

23. Shroff H, Galbraith CG, Galbraith JA, Betzig E (2008) Live-cell photoactivated localization microscopy of nanoscale adhesion dynamics. 5: 417-423.

24. Shroff H, Galbriath C, Galbraith J, White H, Gillette J, et al. (2007) Dual-color supperresolution imaging of genetically expressed probes within individual adhesion complexes. Proceeding of the National Academy of Science 104: 20308-20313.

25. Biteen JS, Thompson MA, Tselentis NK, Bowman GR, Shapiro L, et al. (2008) Super-resolution imaging in live Caulobacter crescentus cells using photoswitchable EYFP. 5: 947-949.

26. Betzig E, Patterson G, Sourgrat R, Lindwasser OW, Olenych S, et al. (2006) Imaging intracellular fluorescent proteins at nanometer resolution. Science 313: 1642-1645.

27. Hess ST, Girirajan TPK, Mason MD (2006) Ultra-High Resolution Imaging by Fluorescence Photoactivation Localization Microscopy. Biophysical Journal 91: 4258-4272.

28. Huang B, Wang W, Bates M, Zhuang X (2008) Three-dimensional super-resolution imaging by stochastic optical reconstruction microscopy. Science 319: 810-813.

29. Bates B, Huang G, Dempsey T, Zhuang X (2007) Multicolor super-resolution imaging with photoswitchable fluorescent probes. Science 317: 1749-1753.

30. Egner A, Geisler C, Middendorff Cv, Bock H, Wenzel D, et al. (2007) Fluorescence nanoscopy in whole cells by asynchronous localizations of photoswitching emitters. Biophysical Journal 93: 3285-3290.

31. Hell S (2003) Toward fluorescence nanoscopy. Nature Biotechnology 21: 1347-1355.

32. Shaner NC, Patterson GH, Davidson MW (2007) Advances in fluorescent protein technology. J Cell Sci 120: 4247-4260.

33. Gustafsson MGL (2005) Nonlinear structured-illumination microscopy: wide-field fluorescence imaging with theoretically unlimited resolution. Proceeding of the National Academy of Science 102: 13081-13086.

34. Li M, Hazelbauer G (2004) Cellular stoichiometry of the components of the chemotaxis signaling complex. Journal of Bacteriology 186: 3687-3694.

35. Hazelbauer GL, Mesibov RE, Adler J (1969) *Escherichia coli* mutants defective in chemotaxis toward specific chemicals. Proceeding of the National Academy of Science 64: 1300-1307.

36. Wiedenmann J, Ivanchenko S, Oswald F, Schmitt F, Rocker C, et al. (2004) EosFP, a fluorescent marker protein with UV-inducible green-to-red fluorescence conversion. Proceeding of the National Academy of Science 101: 15905-15910.

37. Manley S, Gillette JM, Patterson GH, Shroff H, Hess HF, et al. (2008) High-density mapping of single-molecule trajectories with photoactivated localization microscopy. 5: 155-157.

38. McKinney SA, Murphy CS, Hazelwood KL, Davidson MW, Looger LL (2009) A bright and photostable photoconvertible fluorescent protein. 6: 131-133.

39. Hedblom ML, Adler J (1980) Genetic and biochemical properties of *Escherichia coli* mutants with defects in serine chemotaxis. J Bacteriol 144: 1048-1060.

40. Sanders DA, Mendez B, Jr. DK (1989) Role of the CheW protein in bacterial chemotaxis: overexpression is equivalent to absence. Journal of Bacteriology 171: 6271-6278.

41. Sourjik V, Berg H (2000) Localization of components of the chemotaxis machinery of *E. coli* using fluorescent protein fusions. Molecular Microbiology 37: 740-751.

42. Janakiraman A, Goldberg M (2004) Evidence for polar positional information independent of cell division and nucleoid occlusion. Proceeding of the National Academy of Science 101: 835-840.

43. Marshall JS, Palmer WM (1948) The distribution of raindrops with size. Journal of Meteorology 5: 165-166.

44. Cullum J, Vicente M (1978) Cell growth and length distribution in *Escherichia coli*. J Bacteriol 134: 330-337.

45. de Pedro M, Quintela J, Holtje J, Schwarz H (1997) Murein segregation in *Escherichia coli*. J Bacteriol 179: 2823-2834.

46. Bray D, Levin M, Morton-Firth C (1998) Receptor clustering as a cellular mechanism to control sensitivity. Nature 393.

47. Berg H, Purcell E (1977) Physics of chemoreception. Biophysical Journal 20: 193-219.

48. Besschetnova TY, Montefusco DJ, Asinas AE, Shrout AL, Antommattei FM, et al. (2008) Receptor density balances signal stimulation and attenuation in membrane-assembled complexes of bacterial chemotaxis signaling proteins. Proceedings of the National Academy of Sciences 105: 12289-12294.

49. Osawa M, Anderson DE, Erickson HP (2008) Reconstitution of Contractile FtsZ Rings in Liposomes. Science 320: 792-794.

50. Loose M, Fischer-Friedrich E, Ries J, Kruse K, Schwille P (2008) Spatial Regulators for Bacterial Cell Division Self-Organize into Surface Waves in Vitro. Science 320: 789-792.

51. Wolfe AJ, Berg HC (1989) Migration of bacteria in semisolid agar. Proceedings of the National Academy of Sciences of the United States of America 86: 6973-6977.

52. Baba T, Ara T, Hasegawa M, Takai Y, Okumura Y, et al. (2006) Construction of *Escherichia coli* K-12 in-frame, single-gene knockout mutants: the Keio collection. Molecular Systems Biology 2: 2006.0008.

53. Datsenko KA, Wanner BL (2000) One-step inactivation of chromosomal genes in *Escherichia coli* K-12 using PCR products. Proceedings of the National Academy of Sciences of the United States of America 97: 6640-6645.

54. Cherepanov PP, Wackernagel W (1995) Gene disruption in *Escherichia coli*: TcR and KmR cassettes with the option of Flp-catalyzed excision of the antibiotic-resistance determinant. Gene 158: 9-14.

55. Iafolla MAJ, Mazumder M, Sardana V, Velauthapillai T, Pannu K, et al. (2008) Dark proteins: Effect of inclusion body formation on quantification of protein expression. Proteins: Structure, Function, and Bioinformatics.

Chapter 3

Stochastic Cluster Nucleation

The information presented in this chapter is adapted with permission from Greenfield D, McEvoy AL, Shroff H, Crooks GE, Wingreen NS, Betzig E, Liphardt J (2009). PLoS Biology **7** (6) e1000137 doi: 10.1371/jounal.p.bio.1000137 © 2009 The Authors.

3.1 Summary

We derive an analytic model to explain the observed distribution of chemotaxis cluster sizes in a growing population of bacteria. We begin by assuming that clusters are stationary and that diffusing receptors are captured by existing clusters or nucleate new clusters. This leads naturally to the idea of "basins of attraction," or regions surrounding each cluster that become depleted of receptors. This concept allows us to calculate the growth rate of a cluster as a function of size. We combine this growth of clusters with the steady-state properties of a growing population of bacteria to arrive at an estimate of the distribution of clusters sizes. Finally, we correct this expression by considering the diffusion and coalescence of small clusters. The derived model fits the data and demonstrates that a stochastic mechanism based on receptor diffusion is sufficient to explain the images captured by PALM.

3.2 Derivation of Stochastic Cluster Nucleation Model

To understand how the distribution of cluster sizes arises within a genetically identical population of cells, we constructed a simple model. We assume that receptors are inserted into the membrane at random locations, form dimers (or trimers of dimers), and diffuse in the membrane until they are captured by a pre-existing cluster (Figure 3-1A). At any moment, a given cell has a particular arrangement of clusters with various sizes, and the growth of a given cluster will depend on the competition for receptors with other nearby clusters. Initially, we will assume that the clusters within a cell are stationary and do not diffuse. We would like to determine how the radius of a cluster affects the probability that a newly expressed receptor diffusing inside the membrane will be captured by that cluster.

Consider the rate of growth of a particular compact cluster of radius a. For simplicity, we treat the surrounding clusters as an absorbing boundary at radius R (Figure 3-1B), where R is the typical distance between clusters within the cell. Receptors (or receptor dimers) will be deposited in the annulus between a cluster of radius a and the effective absorbing boundary at radius R. Each receptor will diffuse until it is absorbed, either by the inner absorbing boundary at a or by the outer absorbing boundary at R (representing the surrounding clusters). The rate of growth of the cluster with radius a is therefore determined by the total rate at which receptors are deposited in the annulus times the fraction of receptors absorbed by the inner boundary. To solve for this fraction, consider the diffusion equation for

receptors, $\frac{\partial C(r)}{\partial t} = D\nabla^2 C(r) + \gamma = 0$ (at steady-state) where $C(r)$ is the concentration of receptors at radius r within the annulus, D is the diffusion coefficient of the receptors, and γ is the insertion rate per unit area of the receptors into the membrane.

Solving the differential equation for $C(r)$ at steady state, one obtains $C(r) = -\frac{1}{4}\frac{\gamma}{D}r^2 + \frac{c_1}{D}\ln(r) + c_2$, where c_1 and c_2 are constants. After applying the appropriate boundary conditions, $C(a) = C(R) = 0$, the solution is $C(r) = -\frac{1}{4}\frac{\gamma}{D}(r^2 - a^2) + \frac{1}{4}\frac{\gamma}{D}(R^2 - a^2)\frac{\ln(r/a)}{\ln(R/a)}$. The total current onto the circular cluster of radius a is given by $J = 2\pi r D \left.\frac{\partial C(r)}{\partial r}\right|_{r=a} = 2\pi a D\left[-\frac{1}{2}\frac{\gamma}{D}a + \frac{\gamma(R^2 - a^2)}{4Da\ln(R/a)}\right]$ which simplifies to $J = \pi\gamma\left[\frac{1}{2}\frac{(R^2 - a^2)}{\ln(R/a)} - a^2\right]$. Note that the current, J, is independent of the diffusion coefficient D but rather depends on the radius a of the cluster and the typical distance R to the surrounding clusters. These two parameters define a "basin of attraction" for a given cluster, which determines whether new receptors inserted near a given cluster will diffuse onto that cluster and be captured, or instead diffuse away to be captured by one of the surrounding clusters. When the distance between clusters is large compared to the cluster size, $R >> a$, the current is approximately $J \approx \frac{\pi\gamma}{2}\frac{R^2}{\ln(R/a)}$. If receptors are added to clusters but do not leave clusters, the growth rate of a cluster is simply the current of receptors onto that cluster,

$$\frac{dN}{dt} = J \approx \frac{\pi\gamma}{2}\frac{R^2}{\ln(R/a)}. \qquad (1)$$

From the above instantaneous rate of growth of a cluster we can learn how clusters grow over time. The number N of receptors in a cluster is related to the cluster radius by $N = \pi a^2/\Delta A$, where ΔA is the area per receptor. We can therefore use $a = \sqrt{N\,\Delta A/\pi}$ to obtain the following expression for the growth rate of a cluster,

$$\frac{dN}{dt} = \frac{\pi\gamma R^2}{2\ln(R) - \ln(\Delta A/\pi) - \ln(N)} = \frac{\alpha}{\beta - \ln(N)}, \qquad (2)$$

where we have defined constants $\alpha = \pi\gamma R^2$ and $\beta = 2\ln(R) - \ln(\Delta A/\pi)$. Integrating $\frac{dN}{dt}$, we obtain the expression $\int_{N_0}^{N}\left[\beta - \ln(N)\right]dN = \int_{t_0}^{t}\alpha\,dt$, which has the solution

$\alpha(t-t_0) = (\beta+1)(N-N_0) - N\ln(N) + N_0\ln(N_0)$. The term $(t-t_0)$ is simply the age of a cluster, $t(N)$, which we can rewrite as

$$t(N) = \frac{1}{\alpha}\left[(\beta+1)(N-N_0) - N\ln(N) + N_0\ln(N_0)\right]. \quad (3)$$

This expression relates the age of a cluster with its size; the relevant parameters are the typical distance between clusters R, the area of a receptor ΔA, the rate of insertion of new receptors into the membrane γ, and the number of receptors at nucleation N_0.

From the above relation between cluster age and cluster size, we can now estimate the distribution of cluster sizes in growing cells. In an exponentially growing population of cells, the number of cells at time *t* is $N_{cells}(t) \propto e^{t/\tau}$, where $1/\tau$ is the growth rate, and the total membrane surface area grows with the same exponential dependence as well. New clusters continuously nucleate such that the average number of clusters per cell is constant at steady state. Therefore, the total number of clusters also grows exponentially, such that $N_{clusters}(t) \propto e^{t/\tau}$. At a particular time t_0 the number of clusters with a given age t_{age} is the number of clusters produced at time t_0 -t_{age}, or $N_{clusters}(t_0 - t_{age}) \propto e^{(t_0 - t_{age})/\tau}$. Thus, there are more young clusters than old clusters. The probability that a given cluster is t_{age} old is $P(t_{age}) \propto e^{-t_{age}/\tau}$, since $e^{t_0/\tau}$ is constant. We write this as

$$P(t) = \frac{1}{\tau}e^{-t/\tau}, \quad (4)$$

where $P(t)$ is the probability that a cluster is of age *t* and $1/\tau$ is the growth rate. The distribution of cluster sizes, measured by the number of proteins in a cluster, is

$$P(N) = \frac{dt}{dN}P(t(N)), \quad (5)$$

where $t(N)$ is the age of a cluster of size N receptors. Substituting Eq. 1 and 4 into Eq. 5 results in

$$P(N) \approx \frac{2}{\tau}\frac{\ln(R/a)}{\pi\gamma R^2}e^{-t(N)/\tau}. \quad (6)$$

Finally, substituting Eq. 3 into Eq. 6 results in an expression for the distribution of cluster sizes as a function of N, the number of receptors in a cluster,

$$P(N) \approx \frac{2}{\tau\alpha}\left[\ln(R) - \ln\sqrt{N\Delta A/\pi}\right]e^{-\left[(\beta+1)(N-N_0) - N\ln(N) + N_0\ln(N_0)\right]/\alpha\tau}, \quad (7)$$

where the approximation holds when the distance between clusters is large compared to the size of a cluster, and for clusters large enough to not diffuse appreciably.

However, small clusters in particular would be expected to diffuse within the cell membrane, leading to the attrition of some clusters of size N as they aggregate with other clusters. To account for this loss of clusters by diffusion and aggregation, Eq. 6 is modified by a survival probability, P_{surv}, such that

$$P_{tot}(N) = P(N)\, P_{surv}(N). \tag{8}$$

If a cluster of size N has an attrition rate of $\mu(N)$, then

$$P_{surv} = e^{-\int_0^{t(N)} \mu\left(N(t')\right)dt'} = e^{-\int_{N_0}^{N} \mu(N')\left(\frac{dN'}{dt'}\right)^{-1} dN'}. \tag{9}$$

Substituting the expression for dN/dt (Eq. 2) into Eq. 9, we obtain

$$P_{surv}(N) = e^{-\int_{N_0}^{N} [\mu(N')(\beta - \ln N')/\alpha]\, dN'}. \tag{10}$$

To determine the attrition rate $\mu(N)$, we assume that the rate of attrition via cluster diffusion and aggregation is the inverse of the typical time for a cluster of size N to diffuse to the boundary at R, so that $\mu(N) = D(N)/R^2$, where $D(N)$ is the diffusion coefficient for a cluster of size N. For diffusion in a two-dimensional membrane, $D = kTb$, where k is the Boltzmann constant, T is temperature, the motility is $b = \frac{1}{4\pi\eta h}(l_c - \ln(a))$ (see [1]), η is the viscosity of the membrane, h is the thickness of the membrane, a is the cluster radius, and l_c is a cutoff set by the dimensions of the cell. Therefore,

$$\mu(N) = \frac{D(N)}{R^2} = \frac{kT}{4\pi\eta h R^2}\left(l_c - \ln\sqrt{N\Delta A/\pi}\right). \tag{11}$$

Substituting Eq. 11 into Eq. 10,

$$P_{surv}(N) = e^{-\int_{N_0}^{N} \frac{kT}{8\pi\eta h R^2}(c - \ln N')[(\beta - \ln N')/\alpha]\, dN'}, \tag{12}$$

where $c = 2l_c - \ln(\Delta A/\pi)$. Performing the integral in the exponent yields

$$P_{surv}(N) = e^{\frac{-kT}{8\pi\eta h R^2 \alpha}\left[N(\ln N)^2 + (c+\beta-2)(N\ln N - N_0 \ln N_0) + (\beta c - \beta - c + 2)(N - N_0) - N_0(\ln N_0)^2\right]}. \tag{13}$$

Recall that the probability, $P_{tot}(N)$, of observing a cluster of size N is given by the product of $P(N)$ and $P_{surv}(N)$. While some of the parameters in $P_{tot}(N)$ are not known, from the above analysis the functional dependence of $P_{tot}(N)$ on N is known to be

$$P_{tot}(N) \approx c_1 e^{-c_2 N + c_3 N \ln(N) - c_4 N(\ln(N))^2}, \tag{14}$$

where we neglect a weak (logarithmic) N dependence of c_1. We can use Eq. 14 to fit our histograms of cluster sizes. Normalizing the distribution fixes the constant c_1. We

fit $P_{tot}(N)$ to our normalized distribution using unconstrained nonlinear optimization with the free parameters c_2, c_3, and c_4.

The good fit of our model (Figure 2-8A-B) to the data strongly suggests that cluster growth is the result of simple receptor aggregation, not complex biological regulation. Importantly, the distribution of sizes does not result from an equilibrium partitioning of receptors among clusters, but rather from the continuous growth and aggregation of clusters in an exponentially growing and dividing population of bacteria.

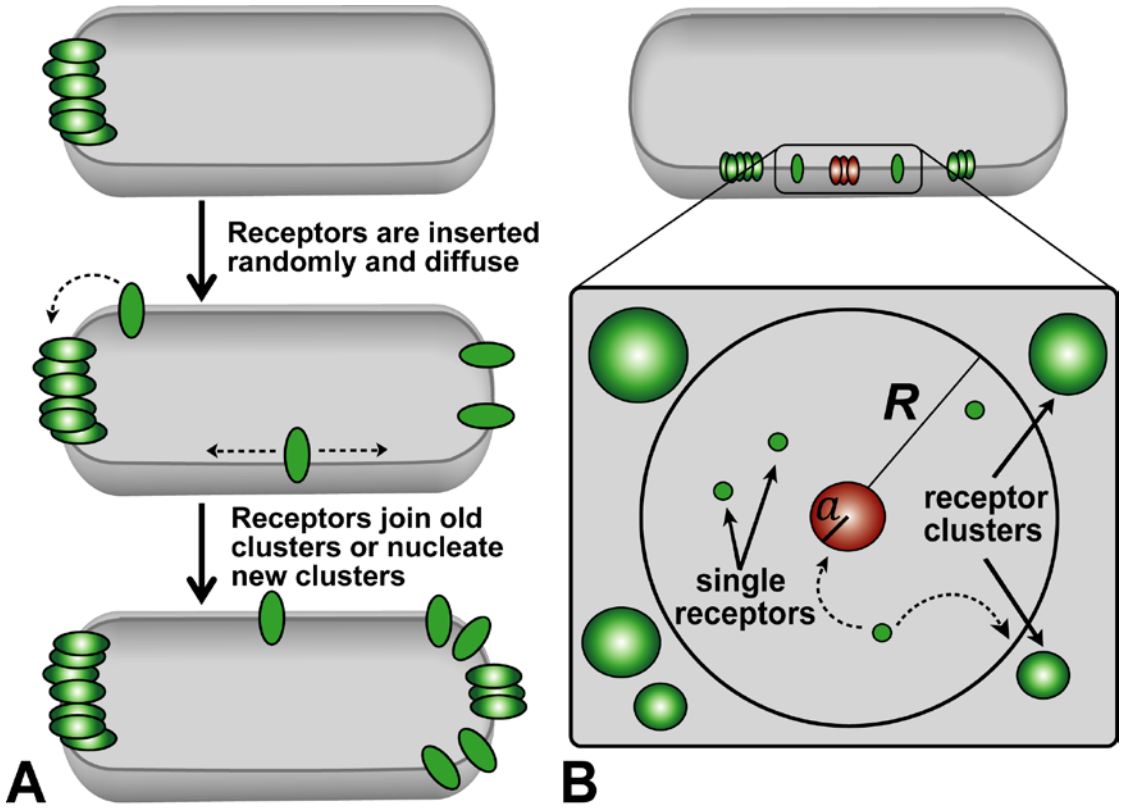

Figure 3-1. Model of how membrane receptor clusters grow. (A) Receptors are inserted randomly into the membrane and then diffuse and join existing clusters or nucleate new clusters. Cluster nucleation is most likely to occur where single receptor dimer (or trimers of dimers) density is high, which occurs far from any existing cluster. **(B)** We model the process of chemotaxis cluster growth in (A) by considering a cluster of radius a a distance R from other clusters. Receptors are inserted into the region between a and R and can either join the cluster of radius a or they can join one of the clusters at the boundary of R. Dotted arrows denote diffusing receptors.

3.3 References

1. Saffman PG, Delbrück M (1975) Brownian motion in biological membranes. Proc Natl Acad Sci 72: 3111-3113.

Chapter 4

The *E. coli* Cell Division Machinery Imaged with Super-resolution Light Microscopy

4.1 Summary

Force generation in biological systems is important for cellular functions such as cell division, motility and transport. In prokaryotic cells, the ubiquitous protein, FtsZ assembles into a ring structure (Z-ring) at mid-cell generating a force which constricts the membrane, initiating cell division. Additionally, FtsZ recruits all other accessory proteins necessary for cell wall remodelling. Though many biochemical and structural details about FtsZ are known, little is known about the *in vivo* structure of the Z-ring and how this structure leads to constriction. Here, we use a combination of super-resolution imaging and conventional time-lapse fluorescence imaging to examine the *in vivo* structure of the Z-ring. We show that Z-rings do not assemble into structures of uniform intensity around the circumference of the bacterium. As the cell proceeds through cytokinesis, the intensity of the Z-ring remains mostly constant, until the ring completely disassembles. Removal of the Min system, which is used to position the Z-ring to mid-cell, dramatically affects Z-ring intensities during cytokinesis, increasing intensity fluctuations within the ring and decreasing FtsZ density within the ring. However, removal of the Min system does not affect the duration of cytokinesis once septation has begun, suggesting that large fluctuations in Z-ring concentration still lead to robust cell division. Ultimately, we provide a simple model for Z-ring assembly and constriction in cytokinesis.

4.2 Introduction

E. coli cell division occurs through binary fission, which requires cell growth, DNA replication and concerted membrane invagination leading to two identical daughter cells each with an identical chromosome (for reviews on this topic see [1–4]). Prior to cytokinesis, a large complex comprised of approximately fifteen proteins, known as the 'divisome,' forms at mid-cell [5]. This assembly process is initiated by the essential protein, FtsZ, which assembles into a ring structure (Z-ring) and recruits all remaining proteins required for cell wall remodelling [5, 6].

FtsZ, like its tubulin homolog, is a self-activating GTPase [7–9]. *In vitro*, FtsZ assembles into short 100-200 nm protofilaments that are one subunit wide and are capable of GTP hydrolysis [6, 10–12]. Using atomic force microscopy, these short protofilaments have been shown to be capable of annealing into longer filaments [13] and under some conditions, FtsZ protofilaments coalesce into rings, bundles, tubules and sheets[14–19].

When purified, membrane-associated FtsZ assembles into Z-rings around lipid vesicles which are capable of bi-lateral movements along the liposome [20]. Strikingly, these Z-rings are capable of constricting membranes without the addition of accessory proteins. However, it is not known how this force is generated. GTP hydrolysis facilitates protofilament disassembly, but does not itself generate a force of constriction [21].

In vivo, conventional fluorescence imaging of FtsZ labelled with GFP reveals Z-ring structures that form rings [22, 23], short-pitch helices [24, 25], as well as long filamentous spirals that extend across the long-axis of the bacterium (Figure 4-1a) [24, 25]. These structures are highly dynamic, with long filaments oscillating from one side of the bacterium to the other side on the minute timescale. These spiral structures then coalesce into rings prior to cytokinesis. [22, 25]. The ring itself is also highly dynamic, with fluorescence recovery after photobleaching (FRAP) studies measuring FtsZ subunit turnover times to be approximately 8-9 sec [15, 26]. Contrary to the long continuous filamentous structures observed by conventional fluorescence imaging, recent cryotomography images of *Caulobacter crescentus* reveal Z-ring structures comprised of isolated short protofilaments (Figure 4-1b) [27]. Super-resolution optical imaging of the Z-ring show ring phenotypes similar to conventional fluorescence techniques [28–30]. Fu *et al.* measured FtsZ density from photoactivated localization microscopy (PALM) images of the Z-ring to conclude that FtsZ assembles into bundles of filaments, rather than two-dimensional sheets of protofilaments [28]. However, individual protofilaments were not resolvable, even with ~35 nm resolution.

Two principal models exist for how Z-rings generate forces (reviewed in [31]). The first is based on the observations that FtsZ-GTP bound protofilaments prefer a straight conformation, whereas upon GTP hydrolysis, FtsZ-GDP bound protofilaments adopted a curved configuration [16, 32]. If straight filaments are attached to the membrane, once GTP-hydolysis occurs, the filaments will bend, which could generate a force that curves the membrane (Figure 4-1c). The other model proposes lateral bonds between the FtsZ protofilaments, which produce mechanical work as they interact and slide along each other [21, 33, 34]. Increasing the number of lateral interactions thereby increases the forces generated (Figure 4-1d). However, if lateral interactions exist, they are not traditional lateral bonds like those in a microtubule wall, rather, they may be due to electrostatic interactions between subunits (discussed in [17]; reviewed in [6]).

Though much biochemical and structural data about FtsZ is known, the detailed *in vivo* structure of the Z-ring is not well understood. Many questions remain about how the Z-ring generates the force of constriction. Gaining insight into

the *in vivo* structure of the Z-ring will lead to an improved understanding of how cell division occurs.

To obtain the *in vivo* structure of FtsZ, we utilized different super-resolution imaging modalities, including localization based methods (PALM, STORM, etc., collectively referred to hereafter as (f-)PALM/STORM) [35–37] and linear structured-illumination microscopy (SIM) [38, 39]. Both optical techniques obtain higher resolution images by limiting the population of excited molecules in a particular spatial region of the sample. In the case of (f-)PALM/STORM, this is done by stochastically activating photoactivatable probes, and in the case of SIM, this is performed through patterned illumination (reviewed in [40]).

As revealed by Li *et al.*, FtsZ seems to assemble into a Z-ring of non-uniform intensity around the circumference of the bacterium [27]. FtsZ initiates membrane constriction; therefore we expected that a non-uniform localization pattern around the circumference of the cell would produce asymmetric curvature of the membrane at mid-cell. Consistent with this hypothesis, membrane curvature is not uniform around the bacterium, and is not correlated with FtsZ intensity.

Using 3D-SIM, and conventional time-lapse imaging of the Z-ring, we show that FtsZ concentration within the Z-ring remains approximately constant throughout cell division. At septation, the FtsZ concentration in the ring begins to decrease until the Z-ring completely disassembles. Removal of the Min system, which localizes FtsZ to mid-cell (for reviews see [41, 42]), dramatically affects Z-ring intensities during division. Cells lacking the Min system show dramatic fluctuations in Z-ring intensity during division, gradually losing subunits throughout cytokinesis.

In chapter 4, we combine super-resolution imaging with conventional time-lapse imaging to examine how Z-rings change throughout the cell cycle. We show how Z-rings are affected by the removal of two regulators of FtsZ localization. Ultimately, we present a simple model for Z-ring constriction and force generation throughout the cell cycle.

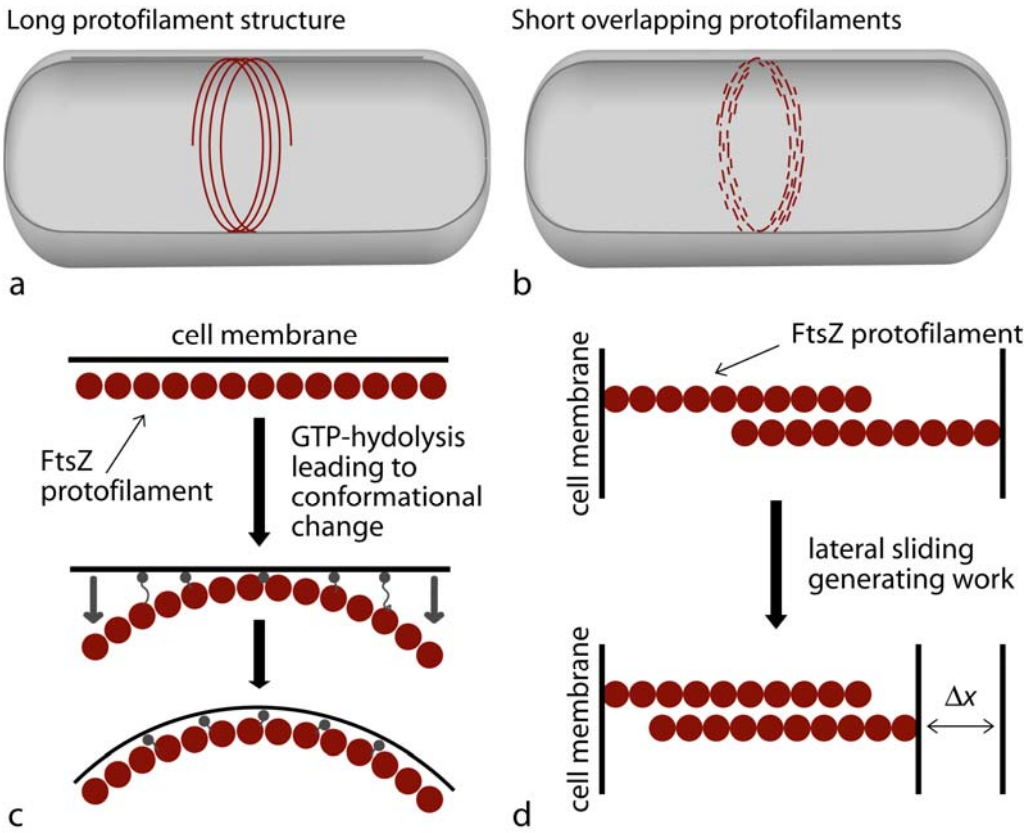

Figure 4-1. Current models for Z-ring assembly and force generation. (a) A model of the *in vivo* structure of the Z-ring. Short protofilaments (80-200 nm long) anneal into a long protofilament encircling the circumference of the bacterium. **(b)** An alternative model, in which short FtsZ protofilaments arrange in a staggered overlap configuration. Possible mechanisms of Z-ring force generation. **(c)** Straight protofilaments, anchored to the membrane (gray dots), hydrolyze GTP, changing their preferred organization to the curved conformation. The bending of the protofilament may create a force (gray arrows) on the membrane. **(d)** An alternative model for force generation. Short protofilaments attached to the membrane overlap and interact laterally. As the protofilaments slide along each other, they perform mechanical work that brings the anchored sites closer together.

4.3 Results and Discussion

Super-resolution imaging of FtsZ and FtsZ binding proteins.

To examine the *in vivo* structure of FtsZ in more detail, we first imaged live whole *E. coli* cells with linear-structured illumination microscopy (SIM). SIM is a useful technique to examine the finer structural details within cells because it generates 3D, multi-color reconstructions quickly [38, 43–45]. We imaged FtsZ-GFP in a previously described *E. coli* strain (EC448 [46]), which expresses endogenous levels of unlabeled FtsZ and FtsZ-GFP from a single chromosomal copy under the control of the lac promoter. We stained the outer membrane of the bacterium with FM4-64, a live-cell membrane stain and imaged fields of bacteria growing under an agar plug (Figure 4-2a).

3D-SIM reconstructions of hundreds of cells induced at 10 μM IPTG, showed a variety of Z-ring structures (Figure 4-2a). Shorter cells often exhibited one bright spots on one side of the cell, or a partial Z-ring (Figure 4-2a, Figure 4-3a). Longer cells often had Z-rings with more uniform intensity around the circumference of the bacterium (Figure 4-3). Many cells appeared to have spiral structures at mid-cell, or partial spiral structures (Figures 4-3a,b). These structures were independent of induction level (Figure 4-3b). Long continuous filamentous structures which extend from one end of the cell to the other end along the long axis were not observed under our imaging conditions. These architectures are not a consequence of FtsZ dynamics during imaging, as similar phenotypes were observed in fixed cells (Figure 4-3c). To determine if these structures were produced by unlabeled endogenous FtsZ, we expressed a GFP-tagged FtsZ binding protein in a knockout background. We labeled the non-essential ZapA protein, which binds directly to FtsZ to promote FtsZ protofilament bundling [47, 48]. Tagging ZapA with GFP did not disrupt mid-cell localization or cause growth defects in Δ*zapA* cells. 3D-SIM images of ZapA in live and fixed Δ*zapA* cells produced Z-ring structures similar to those of FtsZ-GFP (Figure 4-3d,e).

A limitation of 3D-SIM imaging is the resolution, which is limited to twice that of diffraction limited imaging (approximately 125 nm laterally, 250 nm axially). To obtain higher-resolution images of the *in vivo* structure of the Z-ring we used localization-based super-resolution methods ((f-)PALM/STORM) [35, 36, 49], to image fixed whole cells. Using a primary antibody targeting FtsZ and a secondary antibody labeled with both Cy3 and Alexa647, we obtained 2D (f-)PALM/STORM images using a custom built microscope [50]. Consistent with 3D-SIM reconstructions, Z-ring structures were not of uniform intensity around the

bacterium (Figure 4-2b). To ensure these structures were not an artifact of poor antibody labeling, we genetically expressed mMaple-ZapA fusion proteins in Δ*zapA* cells. mMaple is a photoconvertible protein discussed in Chapter 5. Δ*zapA* cells expressing mMaple-ZapA did not exhibit growth defects and mMaple-ZapA localized properly to mid-cell. Like all other imaging methods, (f-)PALM/STORM images of mMaple-ZapA fusion proteins show similar non-uniform distributions of intensity in 2D (Figure 4-2c).

Taken together, our results are consistent with the cryo-EM results of Li *et al.* [27] and suggest that the Z-ring is assembled from protofilaments in a staggered-overlap configuration (Figure 4-1b), rather than short filaments that anneal into a long filamentous structure (Figure 4-1a). Since FtsZ guides the insertion of new cell wall material [51], we hypothesized that if the ring does not have uniform intensity around the bacterium, that perhaps the curvature at the mid-cell may also be asymmetric. Consistent with this hypothesis, we examined 3D-SIM reconstructions of the membrane of dividing cells and observed 30% had noticeable differences in curvature on one side in comparison to the other side (> 160 nm in 3D-SIM images, > 80 nm in (f-)PALM/STORM images) (Figure 4-2d arrow). (f-)PALM/STORM images of an anti-GFP antibody labeled with Cy3 and Alexa 647 that non-specifically stained E. coli membranes, showed similar asymmetric curvature in 26% of the cells (Figure 4-2e). Dual-labeled (f-)PALM/STORM images reveal similar ring and membrane geometries (Figure 4-2f). Surprisingly, we noticed that increases in local FtsZ concentration did not necessarily correlate with increases in local curvature.

To understand how FtsZ intensity correlates with curvature, we first examined each cell individually. We defined curvature as the distance from the tangent line drawn parallel to the long-axis of the bacterium to the most curved region at mid-cell (Figure 4-4a gray line). We measured the intensity of FtsZ on both sides of the cell and asked if the side with larger curvature also has more FtsZ. We measured the curvature on both sides of the cell in 65 cells (43 cells imaged by 3D-SIM, 22 cells imaged with (f-)PALM/STORM). Measuring the corresponding FtsZ intensity at those constriction sites revealed that the side of the mid-cell with larger curvature is just as likely to have higher local concentration of FtsZ as the other side (55.8% for 3D-SIM; 54.5% for (f-)PALM/STORM imaging). Quantifying the intensity of 21 cells imaged with 3D-SIM (42 constriction sites) showed no correlation with local curvature at that point (Figure 4-4b). However, since FtsZ is highly dynamic, it is possible that static images obscure a correlation between local FtsZ concentration and curvature.

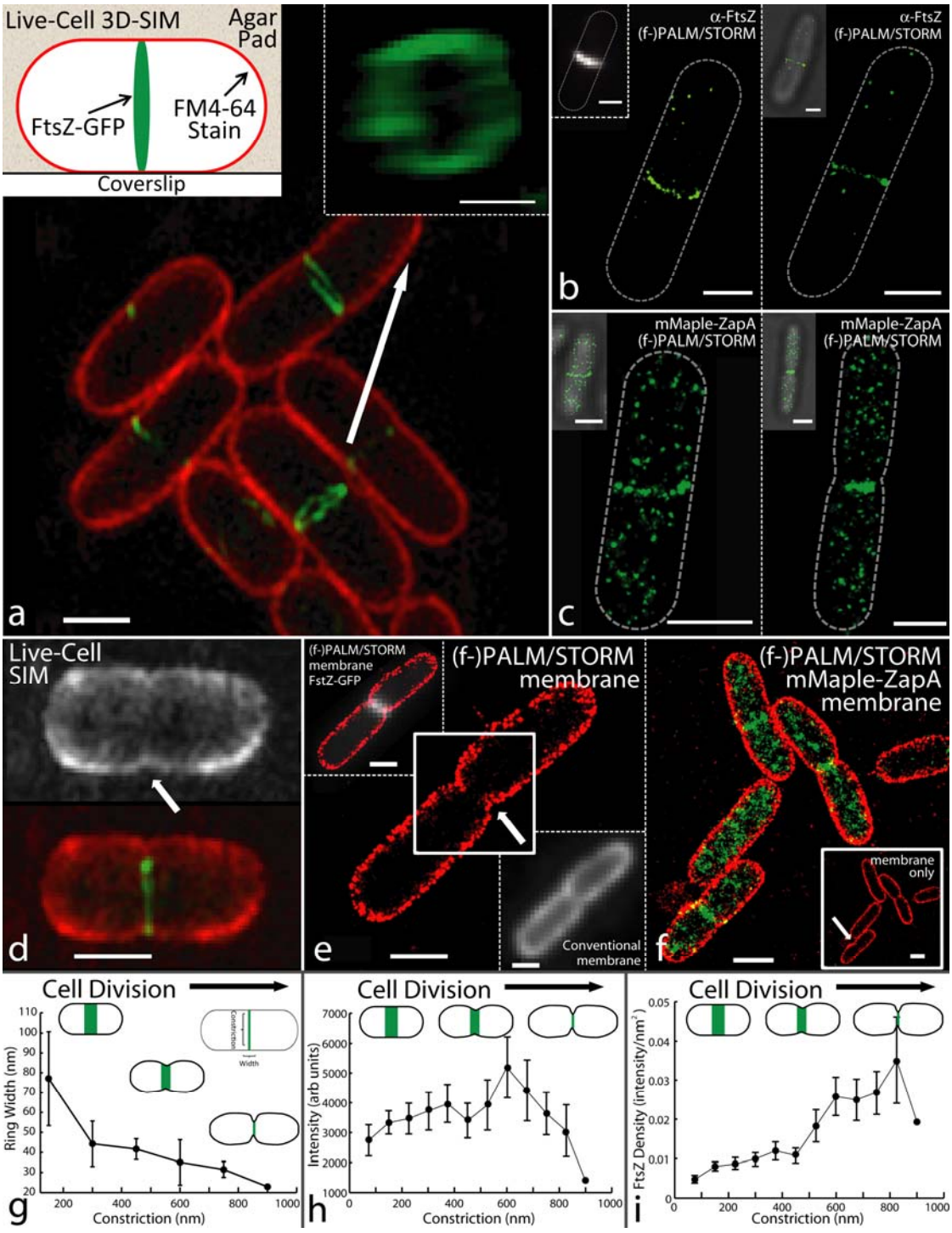

Figure 4-2. Super-resolution images of the Z-ring and cell membrane. (a) 2D projection of a 3D-SIM reconstruction of several live *E. coli* growing under an agar plug (experimental geometry shown in left inset). Cells expressing FtsZ-GFP

induced with 10 μM IPTG and stained with FM4-64 (a live membrane stain). Several cells show rings of non-uniform intensity around the circumference of the bacterium. The most complete ring in the field of view is rotated 90° around the y-axis (right inset). **(b)** 2D (f-)PALM/STORM images of immunolabeled FtsZ. Conventional fluorescence (left inset) and bright-field (right inset) images are shown for comparison. **(c)** 2D (f-)PALM/STORM images of mMaple-ZapA induced with 0.01% arabinose, in a Δ*zapA* strain background. The corresponding bright-field images combined with the super-resolution image (insets). **(d)** 2D projection of 3D-SIM reconstruction of the membrane (top) and the Z-ring image combined with membrane image (bottom). At mid-cell, the curvature on one side of the cell is not the same as the other side (arrow pointing to region of larger curvature). **(e)** 2D (f-)PALM/STORM image of immunolabeled outer membrane. Once again the mid-cell curvature is not symmetric (arrow denotes side of larger curvature). The super-resolution image overlayed on the FtsZ-GFP conventional image, as well as the conventional membrane image is shown for comparison (insets). **(f)** Dual-labelled (f-)PALM/STORM image of mEos2-ZapA and the outer membrane. The membrane only (f-)PALM/STORM image is also shown, with an example of asymmetric curvature (arrow, inset). **(g)** Measured ring dimensions obtained from immunolabeled FtsZ imaged with (f-)PALM/STORM. The width of the ring decreases as the cell proceeds through cell division. **(h)** Z-ring intensity, as measured by 3D-SIM, stays mostly constant during cell division. This corresponds to an increase of FtsZ density as the ring constricts **(i)**. All scale bars are 1 μm, except in panel **(a)** (right inset) which has a 500 nm scale bar.

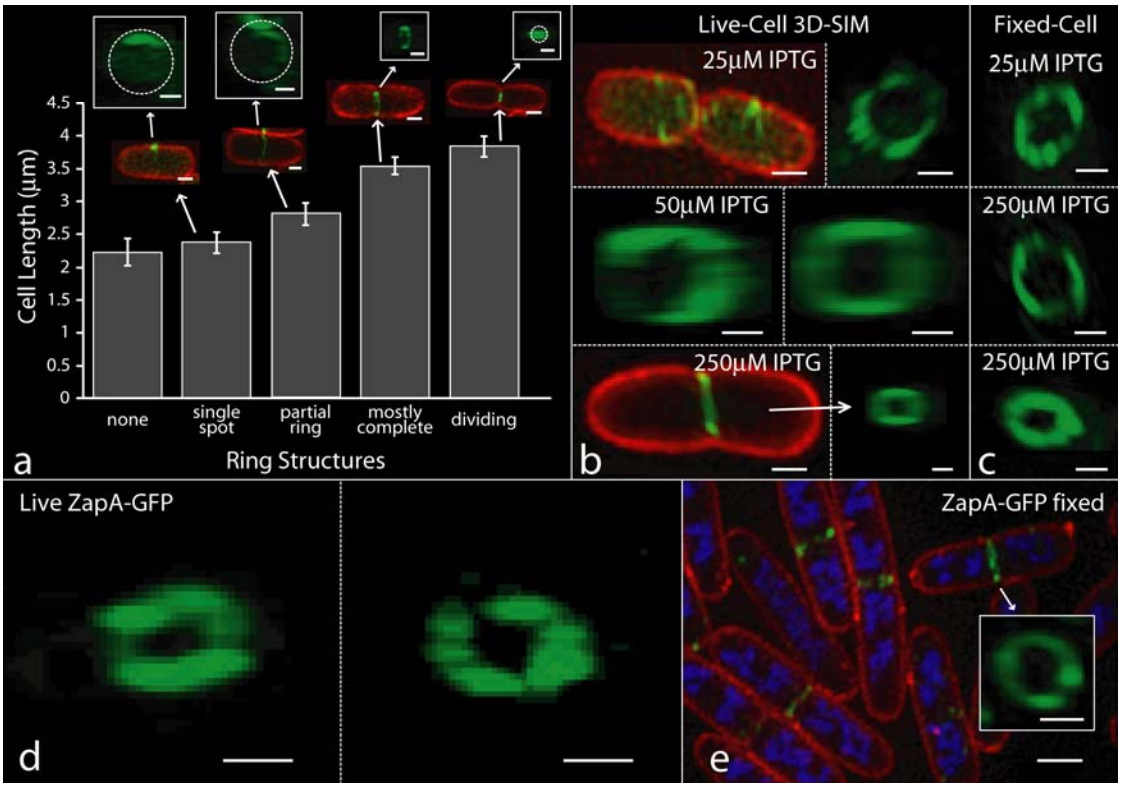

Figure 4-3. 3D-SIM reconstruction show non-uniform Z-ring intensities. (a) Z-rings obtained by 3D-SIM imaging of cells induced with 10 μM IPTG were categorized based on localization of FtsZ intensity. Shorter cells often had single spots of FtsZ on one side, or partial rings. Longer cells often had rings with more uniform distributions of ring intensity. Insets show examples of each phenotype (FtsZ-GFP in green, FM4-64 membrane stain in red). Partial rings were observed at higher induction levels (25 μM IPTG, and 50 μM IPTG **(b (top)** and **(b, middle-left)**). Partial rings are not an artifact of SIM imaging since rings of more uniform density were also observed at higher induction (50 μM IPTG **(b, middle-right)** and 250 μM IPTG **(b-bottom)**). Fixed cells also show Z-rings of non-uniform ring intensity **(c)**. GFP-ZapA, an FtsZ binding protein, shows similar ring geometries in live **(d)** and fixed cells **(e)**. Δ*zapA* cells expressing GFP-ZapA were induced with 0.001% arabinose. Fixed Δ*zapA* cells were labelled with DAPI (blue) and FM4-64 (red). Scale bars are 500 nm.

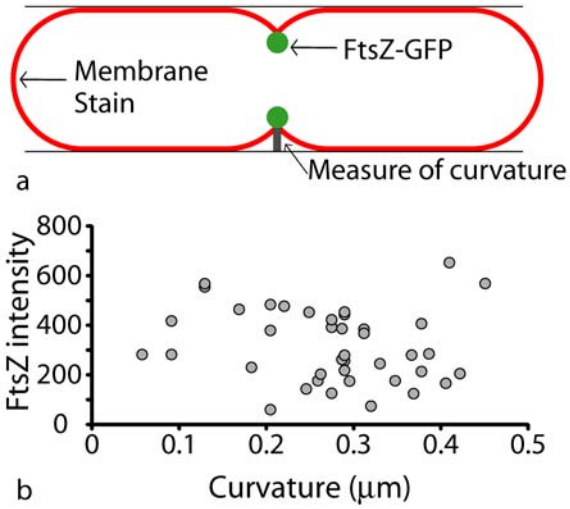

Figure 4-4. Ring intensity is not correlated with degree of mid-cell curvature. (a) Curvature was defined as the distance from a line drawn parallel to the long-axis of the cell (thin black lines) to the most curved region at mid-cell (gray line). **(b)** 3D-SIM images were used to measure the local FtsZ intensity on either side of the cell and the corresponding membrane curvature. Local FtsZ concentration does not seem to correlate with constriction distance.

Ring properties during cell division.

To obtain a better understanding of how Z-ring intensity contributes to mid-cell constriction, we observed how Z-ring properties change during cell division. First, we examined the immunolabeled (f-)PALM/STORM images as they have the highest resolution of any of the direct FtsZ labeling methods we attempted. To estimate how the Z-ring constricts in a fixed population of cells, we use the diameter of the ring as an indicator of cell cycle. As the cell divides, the ring constricts, therefore we quantified the degree of constriction as the width of the cell at the ¼ or ¾ position minus the ring diameter. The (f-)PALM/STORM images revealed that as the cell proceeds through cell division, the ring gets thinner (Figure 4-2f). The average width of the Z-ring was measured to be 58 ± 23 nm (N = 40 cells).

We hypothesized that the decrease in Z-ring width could be caused by either decreases in FtsZ concentration during cell division, or lateral interactions between the protofilaments compacting the FtsZ subunits. Previous epi-fluorescence studies have shown that GFP-FtsZ concentration within Z-rings decreases during cell division [23, 52, 53]. Contrary to these studies, a recent study showed that the intensity of FtsZ remains constant during cell division [21]. To understand what happens to the FtsZ subunits in the ring during cell division we measured the fluorescence intensity of the ring of the 3D-SIM images. A disadvantage of SIM is that it requires highly photostable fluorophores. In our measurements, after one image acquisition, the Z-ring intensity was no longer detectable due to photobleaching. Therefore, we once again used the ring diameter as an indication of cell cycle. Pseudo-time courses of 140 cells show that the intensity of FtsZ within the ring remains mostly constant over time (Figure 4-2g). Therefore, the density of FtsZ within the Z-ring must increase as the ring diameter shrinks during division (Figure 4-2h).

Using conventional time-lapse fluorescence imaging, Lan *et al.* showed similar results as those presented in Figures 4-2g and 4-2h. They suggested that the increase of FtsZ density within the Z-ring, increases lateral interactions between the subunits, thus generating a force that drives constriction (Figure 4-1d). However, we hypothesized that the increase in FtsZ density during cell division may be attributed to the Min system, a negative regulator of FtsZ position, which through pole-to-pole oscillations leads to FtsZ localization at mid-cell (reviewed in [41, 42]).

To examine the effects of the Min system on Z-ring assembly, we removed the Min system from EC448 (EC448 Δ*minCDE*) and imaged FtsZ-GFP using 3D-SIM (Figure 4-5). Consistent with previous studies, removal of the Min generates long cells and minicells [54]. The long cells often had multiple FtsZ rings, producing multiple constriction sites simultaneously (Figure 4-5a arrows). We saw many

regions with FtsZ that looked like short filaments or partial spirals distributed over the entire length of the bacteria (Figure 4-5b). These small bands could be FtsZ traveling in a spiral pattern (as observed by Thanedar *et al*. [25]), or it could be short protofilaments that have not formed complete rings.

Surprisingly, we observed regions of the membrane that were constricted yet lacked Z-rings (Figure 4-5c). We observed 54 constrictions sites in Δ*minCDE* without Z-rings (13.9% of the total number of constriction sites). Whereas, 'wildtype' cells only had 2 constriction sites without Z-rings (1.1% of the total number of constriction sites). This result suggests that removing the Min system decreases local FtsZ concentration which may depolymerize Z-rings that were in the process of division causing an 'aborted constriction.'

To gain greater insight into how removing the Min system affects the FtsZ ring, we imaged live bacteria using conventional wide-field epi-fluorescence time-lapse microscopy. We imaged both the wildtype strain as well as the Δ*minCDE* strain growing under a rich-defined media (RDM) agar plug at 30 degrees. The cells were grown in RDM and induced with IPTG for one hour before addition to the agar plug. Δ*minCDE* cells were induced at a higher IPTG concentration to ensure Z-ring intensities were approximately similar to the wildtype intensities at the beginning of imaging (Δ*minCDE* starting intensity levels of 11383 ± 3522 au, wildtype starting intensity levels of 11901± 3503 au). The agar plug contained 2% glucose so that cells were not able to produce FtsZ-GFP after addition to the agar plug. To minimize photodamage, the cells were imaged every 30 seconds using a YFP filter-cube, which allowed us to image the FtsZ-GFP with no noticeable phenotypic change on the cells.

We used bright-field images to examine the degree of membrane constriction and followed the Z-rings in fluorescence. We examined 95 wildtype cells, each with their own Z-ring which proceeded to full constriction over time. Consistent with the SIM data, we found no evidence of regions of mid-cell curvature that lacked FtsZ rings. In Δ*minCDE* cells, we observed 11 'aborted constrictions' (10.7% of 103 total constriction sites in 38 cells) (Figure 4-5d). In each case, the rings would start to constrict, then disassemble and on the timescale of our experiment, the region would not complete cytokinesis. Instead, the ring that began septation, would form a helical structure or would split into two rings, the first ring would stop dividing and disassemble, while the second ring would then complete cytokinesis. This suggests that the consequence of the Min system localizing FtsZ to the mid-cell is that it helps to maintain Z-ring structures during division.

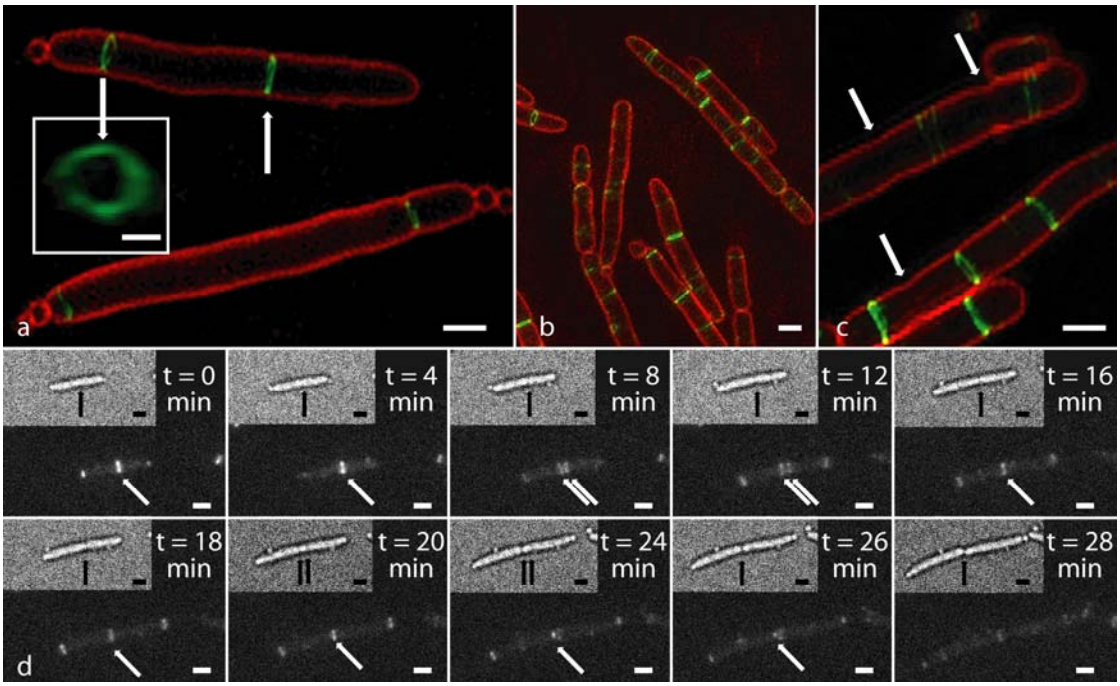

Figure 4-5. 2D projections of 3D-SIM reconstructions and time-lapse imaging of FtsZ-GFP in Δ*minCDE* cells. (a) SIM images of FtsZ-GFP (induced at 10 μM IPTG) in Δ*minCDE* show multiple ring in long cells and multiple constriction sites (denoted by arrows) as well as minicells. (inset) One of the rings is rotated 90° around the y-axis. Scale Bar is 500 nm. **(b)** Field of view of a number of Δ*minCDE* cells reveals many bright Z-rings and regions of FtsZ distributed throughout the cell length. **(c)** Regions of membrane constriction lacking Z-rings (denoted by arrows). **(d)** Conventional time-lapse imaging of Δ*minCDE* cells showing an 'aborted constriction' (corresponding bright-field images in top left of each panel). At 8 minutes, the Z-ring in the middle splits into two rings. The ring on the right starts to constrict (black arrow, bright-field), but disappears at t = 16 min. At t = 20 min, a second region of curvature develops, corresponding to the location of the second ring which then completely constricts. Scale bars are 1 μm.

Consistent with previous studies, conventional time-lapse imaging of wildtype cells expressing FtsZ-GFP, have a single ring localized to mid-cell that decreases in diameter as the cell divide [6, 23, 52, 53] (Figure 4-6a). Prior to complete disassembly of the mid-cell ring, two rings assemble at the ¼ and ¾ positions of the new daughter cells (Figure 4-6a). All Δ*minCDE* cells had multiple Z-rings. These rings are highly dynamic, assembling and disassembling on the 30 second timescale. Over the course of an experiment, these rings may or may not lead to cytokinesis, with some Z-rings varying widely in intensity from frame to frame.

To understand how Z-ring intensity changes during divison, we measured the intensity in a small region of interest (ROI) for each frame of the time-lapse movie. Figure 4-6c shows the resulting 'intensity trajectories' for Z-rings within three different wildtype cells. Consistent with the pseudo time-courses produced by the 3D-SIM reconstructions, we see that the intensity in the Z-rings remains approximately constant for the majority of cell division. We normalized the Z-ring intensity trajectories and aligned the traces such that complete disassembly of the ring occurred at the same timepoint (Figure 4-6e, black curve) (N = 95 wildtype cells (45 parent cells and 50 daughter cells)).

Removal of the Min system resulted in Z-ring intensities that would often gradually decrease during division (94.5% traces showed gradual decline in FtsZ intensity) (Figure 4-6d (N = 3 cells); Figure 4-7a) Other Z-rings in Δ*minCDE* cells would start at low intensity values, increase and then gradually decrease again. Normalizing the Z-ring intensity trajectories from Δ*minCDE* cells and aligning the traces such that complete disassembly of Z-rings occurred at the same point revealed that Z-ring intensity decreased approximately twice as fast as in wildtype cells in comparison to Δ*minCDE* cells (Figure 4-6e; N = 95 wildtype cells, N = 90 Δ*minCDE* cells).

Since removal of the Min system delocalizes FtsZ concentration, we hypothesized that this would lead to increases in fluctuations in Z-ring intensity during division. At each point in time, we measured the deviation of Z-ring intensity from the mean intensity of the entire trajectory. Consistent with our hypothesis, the distribution of Z-ring intensity fluctuations for Δ*minCDE* cells was twice as large as wildtype cells (Figure 4-6f; σ = 1227 ± 48 au wildtype cells, σ = 2569 ± 65 au Δ*minCDE* cells)

We suspected that increases in Z-ring intensity fluctuations would lead to dramatic changes in ring lifetimes for the Δ*minCDE*. We defined ring-lifetime as the time the ring first appeared in fluorescence until it completely disassembled. As expected, Δ*minCDE* ring lifetimes (μ = 1698 ± 96 sec) were approximately twice that of wildtype cells (μ = 883 ± 30 sec).

We then asked whether the differences in ring lifetime gave rise to differences in the 'septation time.' Septation time was defined as the time from when the first noticeable membrane constriction occurred (as judged by bright-field imaging) until Z-ring disassembly. Though the ring lifetimes for Δ*minCDE* cells are much longer than wildtype cells, the time from the beginning of septation until the end of cytokinesis was approximately the same (Figure 4-6h, $\mu = 296 \pm 8$ sec for wildtype cells; $\mu = 401 \pm 12$ sec for Δ*minCDE* cells). Though removal of the Min system leads to large fluctuations in Z-ring intensity and ring lifetime, once membrane separation has begun, removing the Min system has little effect on the completion of cytokinesis.

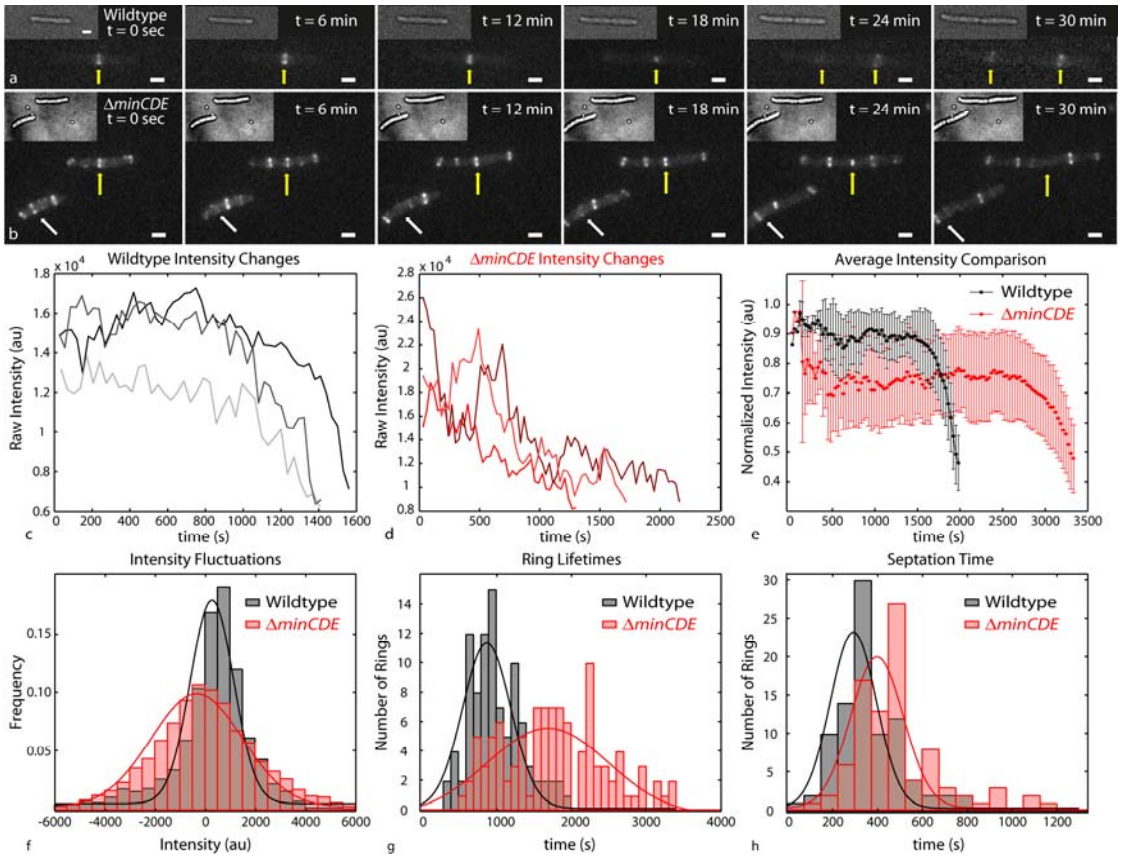

Figure 4-6. Conventional time-lapse imaging of wildtype and Δ*minCDE* cells. (a) Each wildtype cell has a single Z-ring that constricts during cell division leading to daughter cells each with their own Z-ring (yellow arrows). **(b)** Δ*minCDE* cells have multiple rings in each cell. On the timescale of imaging, some Z-rings lead to cell division (yellow arrow). Some Z-rings assemble and disassemble on short timescales (white arrow). Corresponding bright-field images are shown in the top-left of each panel in (a, b). **(c)** Example of Z-ring intensity trajectories for three different wildtype cells **(c)** and three different Δ*minCDE* cells **(d)**. **(e)** Intensity trajectories were normalized and aligned such that Z-ring disassembly occurs at the same point in time (N = 95 wildtype cells, N = 90 Δ*minCDE* cells, error is standard deviation). Z-rings in Δ*minCDE* cells show a more gradual decline in FtsZ intensity (red lines) in comparison to wildtype cells (black lines). Δ*minCDE* cells have larger fluctuations in Z-ring intensity (σ = 2569 ± 65 au) **(f)** and longer ring-lifetimes (μ = 1698 ± 95 sec) than wildtype cells (σ = 1227 ± 48 au and μ = 883 ± 30 sec respectively) **(g)**. Septation time is very similar between the two populations of cells (μ = 296.9 ± 8 sec for wildtype cells; μ = 401 ± 12 sec for Δ*minCDE*) **(h)**. Wildtype and Δ*minCDE* strain induction was chosen such that Z-ring intensities were similar at the beginning of imaging (50 μM IPTG for wildtype, 100 μM IPTG for Δ*minCDE* cells). Scale bars are 1 μm.

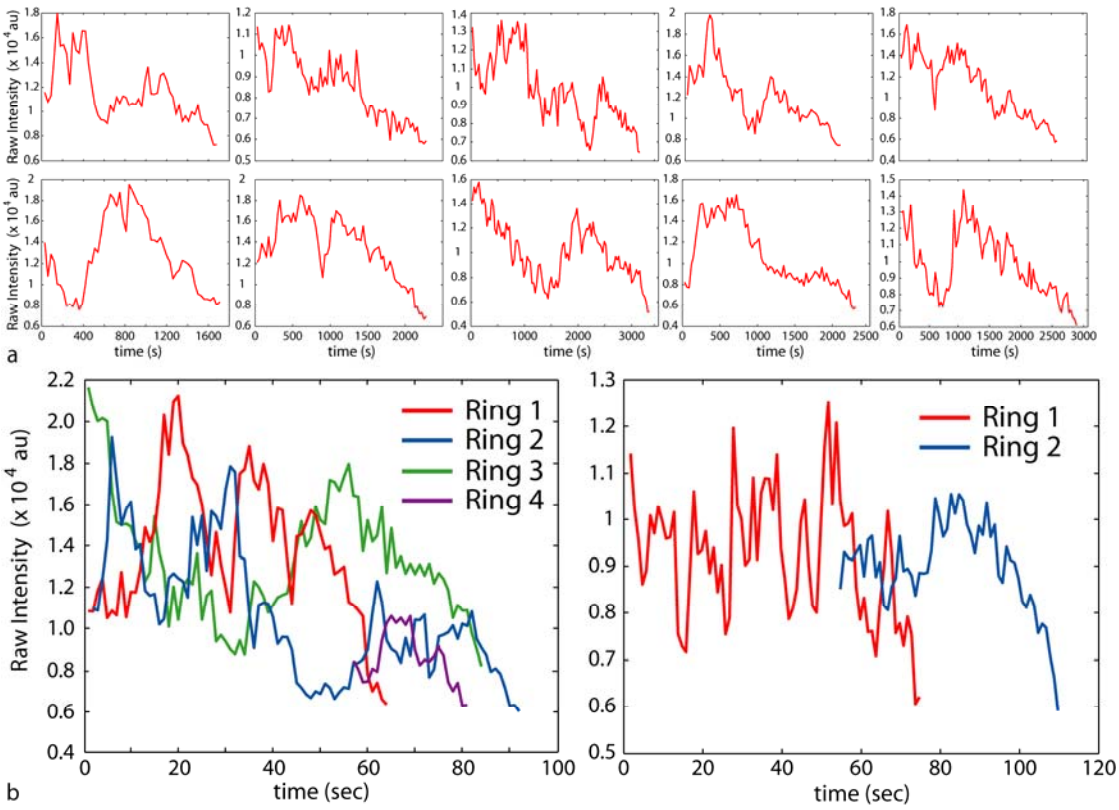

Figure 4-7. *ΔminCDE* Z-ring intensity trajectories. (a) Examples of individual Z-ring intensity trajectories for ten different *ΔminCDE* cells. **(b)** Multiple Z-ring intensity trajectories for rings within the same cell. As one ring decreases in Z-ring intensity, another ring increases in intensity (left), or another ring forms (right).

The Min system is one of two systems that *E. coli* uses to FtsZ localization. Nucleoid occlusion, regulated by the DNA binding protein SlmA [55–57], impedes Z-ring assembly around unsegregated nucleoids. We hypothesized that removal of SlmA may also act to delocalize FtsZ concentration causing changes in Z-ring intensity trajectories. Loss of SlmA results in a synthetic lethal phenotype with removal of the Min system [55], therefore, we restricted our experiments to single knockout cases.

Conventional time-lapse imaging of 58 Δ*slmA* cells (23 parent cells and 35 daughter cells) expressing FtsZ-GFP show no obvious phenotypic differences as wildtype cells (Figure 4-8a). Z-ring intensity trajectories also had similar distributions as wildtype cells (Figures 4-8b,c). Intensity fluctuations (Figure 4-8d; $\sigma = 1225 \pm 53$ au) and Z-ring lifetimes (Figure 4-8e; $\mu = 926 \pm 66$ s) in Δ*slmA* cells were also similar to the wildtype case. The septation time of Δ*slmA* cells was similar to both the wildtype and Δ*minCDE* strains ($\mu = 377 \pm 24$ s). These results suggest that of the two systems used to localize FtsZ, that the Min system has the largest effect on mid-cell FtsZ concentration.

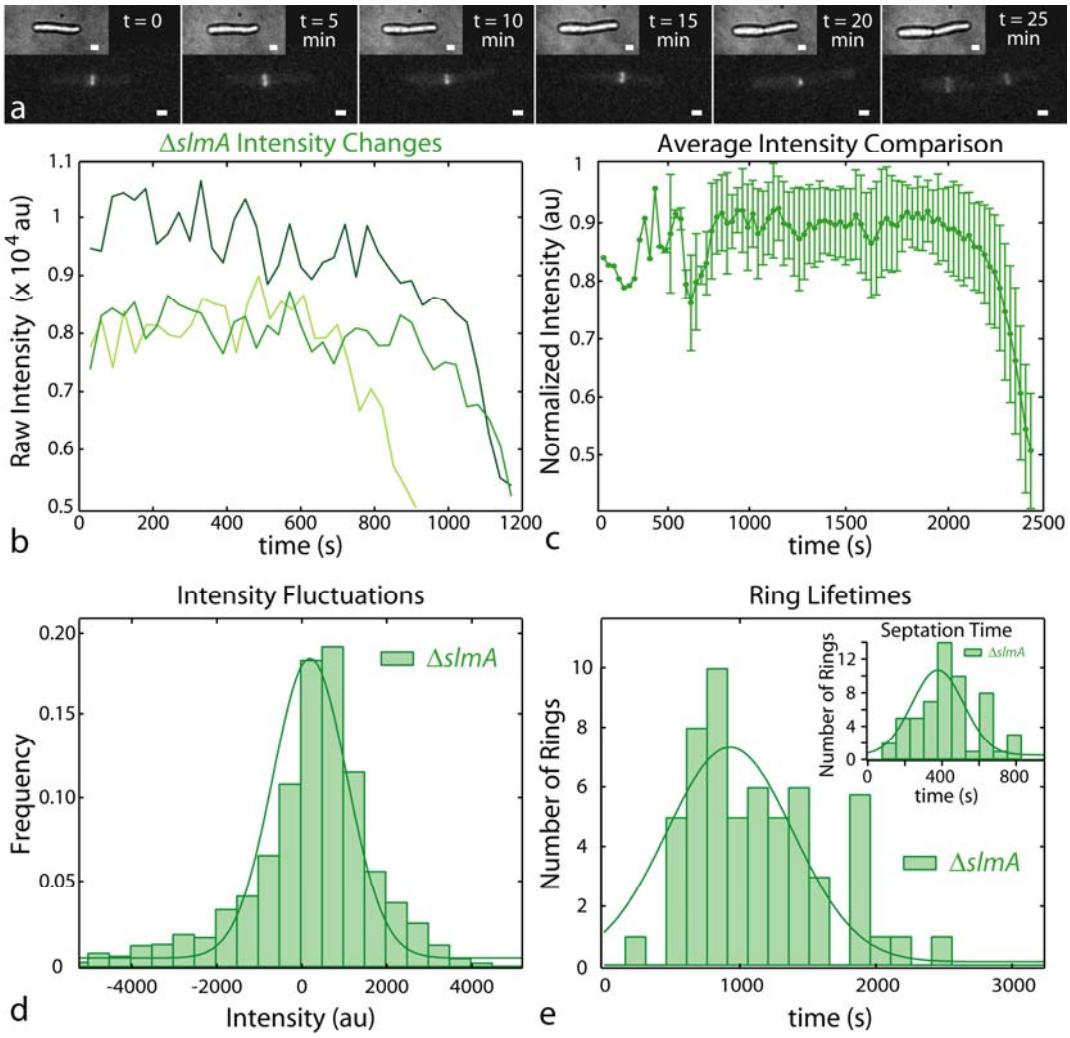

Figure 4-8. Conventional time-lapse imaging of *ΔslmA* cells expressing FtsZ-GFP. **(a)** Z-rings in *ΔslmA* cells exhibit no phenotypic changes in comparison to wildtype cells, with each cell having an individual Z-ring that constricts as the cell divides. **(b)** Examples of three Z-ring intensity trajectories show constant Z-ring intensity followed by decrease in intensity as the ring disassembles. **(c)** All trajectories were normalized and aligned such that ring assembly occurs at the same point in time (N = 58 cells). **(d)** Z-ring intensity fluctuations and ring lifetimes are very similar to wildtype (σ = 1225 ± 53 au and μ = 926 ± 66 sec respectively) **(e)**. Septation time is similar to both wildtype and *ΔminCDE* cells (μ = 377 ± 24). *ΔslmA* cells were induced at 50 μM IPTG. Scale bars are 1 μm.

The E. coli divisome matures in two steps. The first step involves assembly of the Z-ring at mid-cell, followed by the recruitment of the machinery which generates new cell wall material. Removal of the Min system leads to larger Z-ring intensity fluctuations which probably lengthens the time required for the divisome to mature and thus explains increased ring lifetimes (Figure 4-6g).

Lack of the Min system leads to delocalization of Z-ring intensity which could produce 'aborted constrictions.' These events appear to 'trick' the cells into initiating septation at regions containing Z-rings. However, during septation, the Z-ring depolymerizes ceasing the completion of cytokinesis. It is possible that without Min localizing FtsZ to a single location, there is an increased likelihood that as FtsZ subunits are exchanged in the Z-ring, they will not return to the ring, eventually leading to complete Z-ring disassembly. However, it is also possible that these rings started to form around unsegregated DNA, and SlmA depolymerized the rings prior to cytokinesis in an effort to retain intact chromosomes.

Surprisingly, larger fluctuations in Z-ring intensity, do not affect bulk growth rates (as measured in [58]) or septation times. This suggests that septation is robust to large FtsZ concentration fluctuations, and that Z-ring intensity is not necessarily correlated with mid-cell curvature.

Previous studies have attributed increases in FtsZ density during division to lateral interactions between FtsZ subunits (Figure 4-1d) [21]. Instead, our results suggest that it is the Min system that leads to increases in FtsZ concentration during division, and Z-rings in Δ*minCDE* cells appear to steadily lose FtsZ concentration. This result is consistent with the model in which straight filaments anchored to the membrane hydrolze GTP altering their preferred conformation which exerts a force on the membrane as the protofilaments bend (Figure 4-1c). Since GTP hydrolysis facilitates Z-ring disassembly, this model would suggest that force generation leads to decreases in FtsZ concentration. The Min system increases FtsZ concentration at mid-cell which could compensate for loss of subunits during division, enhancing the likelihood that FtsZ will return to the ring after hydrolysis.

Force generation in this manner, may also explain why super-resolution images of the Z-ring exhibit non-uniform distributions of FtsZ intensity. It is possible that at the sites of GTP hydrolysis, FtsZ-GDP causes fragmentation within protofilaments as it leaves the ring.

Our results are consistent with the existing model that force generation is caused by filament bending (Figure 4-1c). In the wildtype case, FtsZ protofilaments are anchored to the membrane, and bend after GTP hydrolysis. As subunits leave the ring, the Min system is used to localize FtsZ concentration to mid-cell, increasing the likelihood that FtsZ subunits that are removed, will return to the ring after binding GTP (Figure 4-9a). When the Min system is removed, FtsZ local concentration is

decreased as many positions within the cell are available for Z-ring assembly. However, as long as sufficient FtsZ is present to localize the remainder of the divisome, cytokinesis proceeds as normal (Figure 4-9b). These results are consistent with the emerging picture in biology that stochastic processes, such as Z-ring assembly and disassembly can lead to robust outcomes like cell division.

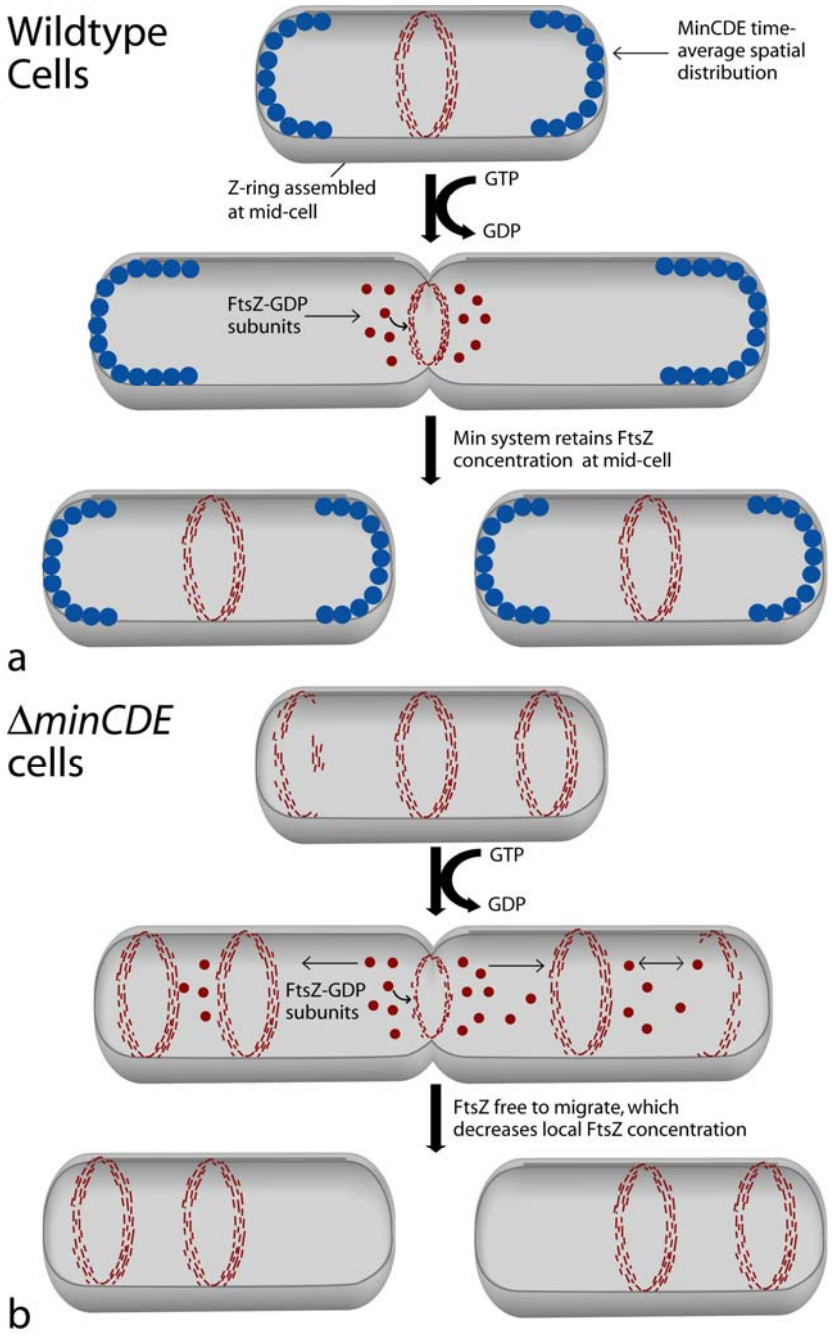

Figure 4-9. Model for force generation during cell division. FtsZ assembles into short straight protofilaments. During Z-ring assembly the protofilaments are anchored to the membrane. After GTP hydrolysis, the subunits bend, exerting a force on the membrane. GTP hydrolysis promotes protofilament disassembly removing FtsZ subunits from the ring. **(a)** In wildtype cells, the Min system localizes FtsZ to mid-cell, such that there is a higher local concentration for during FtsZ subunit exchange, which maintains Z-ring intensity for most of division. **(b)** FtsZ in

cells lacking the Min system is free to diffuse along the length of the cells, and form rings in regions lacking the nucleoid. Therefore, during GTP hydrolysis, as FtsZ leaves the ring, the subunits may travel to other parts of the cell, decreasing Z-ring intensity as the ring constricts.

4.4 Materials and Methods

Bacterial Strains and Plasmids.

All strains are derivatives of MC4100, a wild-type *E. coli* K-12 strain. The FtsZ-GFP fusion strain is EC448 (FtsZ-GFP/Ampicillin) [1, 21, 46], which expresses endogenous levels of unlabeled FtsZ as well as a single genomic copy of FtsZ-GFP under the control of a modified lac promoter [46]. ZapA fusions were expressed in a strain lacking the genomic copy of ZapA. Strains containing ZapA fusions contain the pJat plasmid [59], which contains the arabinose transporter gene (*araE*) under a constitutive promoter to increase the homogenous expression from the arabinose promoter. pJat is gentamicin resistant. ZapA fusions were expressed from the inducible arabinose promoter on the low-copy plasmid pBAD (Invitrogen) containing a pBR322-derived origin, the ampicillin resistance gene (*bla*), and the a*raC* gene for positive regulation of the arabinose promoter. pALM1002, pALM10002 contain *EGFP-zapA*, *mMaple- zapA* gene fusions respectively.

Construction of plasmids.

All fusions to ZapA consist of the fluorescent protein followed by 23 amino acids LQELSRGHGTGSTGSGSSELQGS encoding a PstI and SacI site followed by a 15 amino acid linker (SRGHGTGSTGSGSSE) followed by a PstI site and BamHI site prior to the entire *zapA* gene (residues 1- 110), and a terminal Glu-Phe encoding an EcoRI site.

Plasmid pALM10000 was constructed by PCR amplification of the monomeric *Maple* gene from the pBAD/HisB plasmid containing mMaple using 5'GCTCGACCATGGtGAGCAAGG3'and 5'CCAAGCTTCGAACTGCAGCTTGTACAGCTC3'. These PCR products were subcloned into plasmid pBAD (Invitrogen) using the NcoI and PstI sites. The N-terminal plasmid leader sequence was removed by digestion with NcoI and religation. Plasmid pALM1000 was constructed by PCR amplification of EGFP from the pTrcHis2-EGFP plasmid using the primers 5'GGAGGAATAAACCATGGTGAGCAAG3' and 5'CGTAAGCTTCCTGCAGCTTGTACAGCTCG3'. This PCR product was subcloned into pALM7000 using the NcoI and PstI sites.

Photoactivatable fluorescent fusions to ZapA were constructed by first synthesizing the entire *ZapA* gene (DNA2.0) with a 45 bp linker coding for a TCTCGAGGTCACGGTACTGGTTCTACTGGTTCTGGTTCTTCTGAG amino acid

linker before the gene. To remove the PstI site from the gene, residue 87 of the *ZapA* gene was mutated from CAG to CAA which did not change the amino acid sequence. The synthesized gene was flanked with SacI and EcoRI restriction sites which were used to subclone the gene into pALM1000, pALM7000, and pALM10000 to create pALM1002 (GFP-ZapA), and pALM10002 (mMaple-ZapA).

Strain Construction

MC4100 Δ*zapA* and EC448 Δ*SlmA* were made by P1 transduction from the Keio collection strains JW 2878-1 (Δ*zapA::kan*), and JW5641-1 (Δ*SlmA::kan*). These deletion strain retain the native start codon and the last 18 C-terminal nucleotides to minimize polar effects on downstream gene expression [60]. When cured of kanamycin resistance, the Keio deletion strains retain a translatable scar sequence in-frame with the deleted gene initiation codon and its C-terminal 18-nucleotide coding region. This scar sequence is expected to produce a 34-residue scar peptide with an N-terminal Met, 27 scar-specific residues, and six C-terminal gene-specific residues. ZapA mutant strains were cured of resistances using plasmid pCP20 as described in Cherepanov and Wackernagel [61]. EC448 Δ*minCDE::kan* was made from P1 transduction from JS964 (Δ*minCDE::kan*) [62].

***E. coli* cell culture.**

ZapA mutant strains were grown overnight in LB at 30°C with aeration. Day cultures were inoculated by diluting overnight cultures 1:500 into fresh Luria Broth growth media with appropriate antibiotics (Amp and Gent) at 30°C with aeration until they reached an OD_{600} 0.4–0.6. Protein expression was induced by 0.002% arabinose for 3 hrs. Media and temperature were chosen to obtain the highest expression levels of properly folded proteins [63]. EC448 and its derivatives were grown overnight in LB at 30°C with aeration. Day cultures were inoculated by diluting overnight cultures 1:100 into fresh Luria Broth growth media with appropriate antibiotics at 30°C with aeration until they reached an OD_{600} 0.4–0.6. Protein expression was induced at 10-250 μM IPTG for 1 hour. For timelapse imaging, EC448 and its derivatives were grown as described above, however cells were grown in Rich-Defined Media (RDM) [64] supplemented with 0.2% glucose rather than LB.

SIM sample preparations and imaging.

Cells were harvested by centrifugation at 2,000 *g* for 15 minutes. The outer

membrane of the *E. coli* was fluorescently labeled with 10 ng/μL FM4-64 (Invitrogen) diluted in M9 (1.05% M9 salts (Amresco) supplemented with 2 mM $MgSO_4$, 0.1 mM $CaCl_2$ and 0.4% glycerol) for 5 minutes. Cells were washed twice with M9 media and resuspended in fresh M9 media. 20 uL of 1.5% low-melt agar (Apex) dissolved in M9 media was deposited on a 25 mm × 75 mm single shallow depression slide (Boreal Northwest) flanked by two pieces of double stick tape and allowed to air dry. 0.5 μL of cells labeled with FM4-64 were deposited on the top of the agar and sandwiched between a 22 mm^2 #1.5 microscope coverslip (Fisherbrand), and imaged immediately.

SIM imaging was performed on the Deltavision|OMX V3.0 (Applied Precision Inc, Issaquah, WA) containing 405 nm, 488nm, 514 nm, 593 nm and 642 nm laser lines [65]. The samples were imaged with a 100× 1.40 NA oil objective and using 488 nm and 594 nm excitation. The fluorescence emission was split by channel, filtered and imaged using a dedicated custom monochrome 20 MHz camera with Sony ICX285 ER progressive scan CCD using 5 – 60 ms exposures. Acquisition was controlled by the OMXN controller software (Applied Precision Inc, Issaquah, WA) while reconstructions were made with the OMX specific SoftWoRx v4.5.0 software package (Applied Precision Inc., Issaquah, WA). 3D reconstructions were obtained in 125 nm steps. Data was analysed using a combination of imageJ, SoftWoRx v 4.5.0 (Applied Precision Inc, Issaquah, WA) and custom built Matlab scripts (MathWorks).

(f-)PALM/STORM sample preparations.

Cells were fixed harvested by centrifugation at 2,000 *g* for 15 minutes. Cells were resuspended in 2.8% paraformaldehyde with 0.04% gluteraldehyde (Electron Microscopy Sciences) in PBS (pH 7.4) for 10 minutes. Cells were washed twice with PBS and resuspended in fresh PBS. #1.5 Lab-TekII 8-well chambers (Nalge Nunc International) were covered with 200 μL 0.1% w/v poly-L-lysine for 15 min then rinsed with water. Cells were added and spun onto coverslips at 2,000 *g* for 10 min. For inner membrane and FtsZ labeling, the outer membrane of the cells was removed by adding 200 uL of 4 μg/mL lysozyme diluted in GTE buffer (50 mM glucose, 25 mM Tris, pH 7.5, 10 mM EDTA , pH 8.0) for 10 minutes at room temperature [66]. This step was omitted for outer membrane labeling. The cells were rinsed with 3x with 200 uL of 1X PBS. 3% BSA in PBS was used as blocking buffer and added to the cells for 15 minutes at room temperature. Primary antibody towards either FtsZ (a kind gift from W. Margolin) or GFP (abcam #ab290) were diluted in 3% BSA in PBS (1:100, or 1:1000 respectively) and added to the cells for 2 hours at room temperature with gentle shaking. Cells were rinsed 3x in 1X PBS for 10 minutes each. If necessary,

secondary antibodies labelled with Cy3 and Alexa 647, or Alexa405/Alexa647 were diluted in 3% BSA in PBS (1:1000 dilution) and added to the cells for 30 minutes at room temperature with gentle shaking. Samples were rinsed 3x with 1X PBS for 10 minutes. Cells were post-fixed with 2.8% paraformaldehyde + 0.04% gluteraldehyde for 10 minutes at room temperature. Cells were rinsed 3x with 1X PBS and resuspended in fresh PBS for imaging.

(f-)PALM/STORM imaging.

PALM imaging was performed according to Greenfield *et al.* [67] on an Olympus IX71 inverted microscope equipped with a 100×, 1.40 NA objective (Olympus). 405 nm and 561 nm laser light was delivered to the microscope through free space. 488 nm light was delivered via a mercury lamp with appropriate excitation and emission filters. Single-molecule fluorescence signals generated during acquisition were separated from the activation and excitation light using appropriate filter sets [68, 69] within the microscope and passed to an electron-multiplying charge-coupled device (CCD) camera running at approximately 20 Hz (50 ms exposures). Movie acquisition times were dependent on the regions of highest labeled-protein density. Activation intensity was increased slowly such that a given diffraction-limited spot contained no activated proteins > 90% of the time. This is necessary to ensure that only one protein is activated at a time in a single diffraction-limited spot. The localization and image-rendering algorithms used in this work have been previously described [35, 36]. Briefly, images were filtered and proteins were identified as signals that contained counts larger than four standard deviations above background. Proteins that became dark, but reappeared within five frames, were counted as the same protein. Photon distributions were obtained from proteins emitting at least 300 photons. Only proteins that emitted at least 150 photons were counted. Sample drift was corrected by previously described algorithms [35, 70]. Data analysis were done using custom Matlab scripts (Mathworks), as described by Greenfield *et al.* [67], and custom IDL software [69].

Conventional epi-fluorescence time-lapse imaging.

Cells were grown in rich-defined media as described above. Cells were harvested at 2,000 *g* for 2.5 minutes and resuspended in 50 uL of RDM and 5 μL of a 1:100 dilution of 0.5 μm poly-styrene beads. 0.5 μL of the mixture was added to a 1.5% low-melt agar plug (Apex) dissolved in rich-defined media deposited in a Coverwell Imaging Chamber Gasket (Invitrogen C-18161) sandwiched between a 24

x 60 mm² #1.5 microscope coverslip (Fisherbrand), and imaged immediately at 30 degrees using a 100× 1.40 NA oil objective mounted to a Nikon TE2000 microscope. The temperature was maintained using an objective heater. Brightfield and Fluorescence images were taken every 30 seconds using an Andor (South Windsor, CT) iXon camera controlled by custom software. Polystyrene beads were used for focusing. To reduce photodamage, from the 175 W Xenon bulb (Lambda light source; Sutter Instruments, Novato, CA), the FtsZ-GFP was imaged using a YFP filter cube, which did not appear to affect cell growth. Data was analysed using a combination of imageJ and custom Matlab scripts (Mathworks).

4.5 References

1. Dajkovic A, Lutkenhaus J: Z Ring as Executor of Bacterial Cell Division. *Journal of Molecular Microbiology and Biotechnology* 2006, 11:140-151.

2. Goehring NW, Beckwith J: Diverse Paths to Midcell: Assembly of the Bacterial Cell Division Machinery. *Current Biology* 2005, 15:R514-R526.

3. Harry E, Monahan L, Thompson L, Kwang WJ: Bacterial Cell Division: The Mechanism and Its Precison. In *International Review of Cytology*. Academic Press; 2006, Volume 253:27-94.

4. Margolin W: FtsZ and the division of prokaryotic cells and organelles. *Nat Rev Mol Cell Biol* 2005, 6:862-871.

5. Adams DW, Errington J: Bacterial cell division: assembly, maintenance and disassembly of the Z ring. *Nat Rev Micro* 2009, 7:642-653.

6. Erickson HP, Anderson DE, Osawa M: FtsZ in Bacterial Cytokinesis: Cytoskeleton and Force Generator All in One. 2010, 74:504-528.

7. Lowe J, Amos LA: Tubulin-like protofilaments in Ca2+-induced FtsZ sheets. *EMBO J* 1999, 18:2364-2371.

8. de Boer P, Crossley R, Rothfield L: The essential bacterial cell-division protein FtsZ is a GTPase. *Nature* 1992, 359:254-256.

9. Cordell SC, Robinson EJH, Lowe J: Crystal structure of the SOS cell division inhibitor SulA and in complex with FtsZ. *Proceedings of the National Academy of Sciences* 2003, 100:7889-7894.

10. Chen Y, Erickson HP: Rapid in Vitro Assembly Dynamics and Subunit Turnover of FtsZ Demonstrated by Fluorescence Resonance Energy Transfer. *Journal of Biological Chemistry* 2005, 280:22549-22554.

11. Huecas S, Andreu JM: Polymerization of nucleotide-free, GDP- and GTP-bound cell division protein FtsZ: GDP makes the difference. *FEBS Letters* 2004, 569:43-48.

12. Huecas S, Schaffner-Barbero C, Garcia W, Yebenes H, Palacios JM, Diaz JF, Menendez M, Andreu JM: The Interactions of Cell Division Protein FtsZ with Guanine Nucleotides. *Journal of Biological Chemistry* 2007, 282:37515-37528.

13. Mingorance J, Tadros M, Vicente M, GonzÃ¡lez JM, Rivas G, VÃ©lez M: Visualization of Single Escherichia coli FtsZ Filament Dynamics with Atomic Force Microscopy. *Journal of Biological Chemistry* 2005, 280:20909-20914.

14. Rueda S, Vicente M, Mingorance J: Concentration and Assembly of the Division Ring Proteins FtsZ, FtsA, and ZipA during the Escherichia coli Cell Cycle. *Journal of Bacteriology* 2003, 185:3344-3351.

15. Anderson DE, Gueiros-Filho FJ, Erickson HP: Assembly Dynamics of FtsZ Rings in Bacillus subtilis and Escherichia coli and Effects of FtsZ-Regulating Proteins. *Journal of Bacteriology* 2004, 186:5775-5781.

16. Erickson HP, Taylor DW, Taylor KA, Bramhill D: Bacterial cell division protein FtsZ assembles into protofilament sheets and minirings, structural homologs of tubulin polymers. *Proceedings of the National Academy of Sciences* 1996, 93:519-523.

17. Popp D, Iwasa M, Narita A, Erickson HP, Maéda Y: FtsZ condensates: An in vitro electron microscopy study. *Biopolymers* 2009, 91:340-350.

18. Romberg L, Simon M, Erickson HP: Polymerization of FtsZ, a Bacterial Homolog of Tubulin. *Journal of Biological Chemistry* 2001, 276:11743-11753.

19. Yu X-C, Margolin W: Ca2+-mediated GTP-dependent dynamic assembly of bacterial cell division protein FtsZ into asters and polymer networks in vitro. *EMBO J* 1997, 16:5455-5463.

20. Osawa M, Anderson DE, Erickson HP: Reconstitution of Contractile FtsZ Rings in Liposomes. *Science* 2008, 320:792-794.

21. Lan G, Daniels BR, Dobrowsky TM, Wirtz D, Sun SX: Condensation of FtsZ filaments can drive bacterial cell division. 2009, 106:121-126.

22. Ma X, Ehrhardt D, Margolin W: Colocalization of cell division proteins FtsZ and FtsA to cytoskeletal structures in living Escherichia coli cells by using green fluorescent protein. 1996, 93:12998-13003.

23. Sun Q, Margolin W: FtsZ Dynamics during the Division Cycle of LiveEscherichia coli Cells. *Journal of Bacteriology* 1998, 180:2050-2056.

24. Niu L, Yu J: Investigating Intracellular Dynamics of FtsZ Cytoskeleton with Photoactivation Single-Molecule Tracking. *Biophysical Journal* 2008, 95:2009-2016.

25. Thanedar S, Margolin W: FtsZ Exhibits Rapid Movement and Oscillation Waves in Helix-like Patterns in Escherichia coli. 2004, 14:1167-1173.

26. Stricker J, Maddox P, Salmon ED, Erickson HP: Rapid assembly dynamics of the Escherichia coli FtsZ-ring demonstrated by fluorescence recovery after photobleaching. *Proceedings of the National Academy of Sciences* 2002, 99:3171-3175.

27. Li Z, Trimble MJ, Brun YV, Jensen GJ: The structure of FtsZ filaments in vivo suggests a force-generating role in cell division. 2007, 26:4694-4708.

28. Fu G, Huang T, Buss J, Coltharp C, Hensel Z, Xiao J: In Vivo Structure of the E. coli FtsZ-ring Revealed by Photoactivated Localization Microscopy (PALM). *PloS one* 2010, 5:e12680.

29. Biteen JS, Goley ED, Shapiro L, Moerner WE: Three-Dimensional Super-Resolution Imaging of the Midplane Protein FtsZ in Live Caulobacter crescentus Cells Using Astigmatism. *ChemPhysChem* 2012, 13:1007-1012.

30. Jennings PC, Cox GC, Monahan LG, Harry EJ: Super-resolution imaging of the bacterial cytokinetic protein FtsZ. *Micron* 2010, 42:336-341.

31. Erickson HP: Modeling the physics of FtsZ assembly and force generation. *Proceedings of the National Academy of Sciences* 2009, 106:9238-9243.

32. Lu C, Reedy M, Erickson HP: Straight and Curved Conformations of FtsZ Are Regulated by GTP Hydrolysis. *Journal of Bacteriology* 2000, 182:164-170.

33. Horger I, Velasco E, Rivas G, Velez M, Tarazona P: FtsZ Bacterial Cytoskeletal Polymers on Curved Surfaces: The Importance of Lateral Interactions. *Biophysical Journal* 2008, 94:L81-L83.

34. Horger I, Velasco E, Mingorance J, Rivas G, Tarazona P, Velez M: Langevin computer simulations of bacterial protein filaments and the force-generating mechanism during cell division. *Physical Review E* 2008, 77:11902.

35. Betzig E, Patterson GH, Sougrat R, Lindwasser OW, Olenych S, Bonifacino JS, Davidson MW, Lippincott-Schwartz J, Hess HF: Imaging Intracellular Fluorescent Proteins at Nanometer Resolution. *Science* 2006, 313:1642-1645.

36. Rust MJ, Bates M, Zhuang X: Sub-diffraction-limit imaging by stochastic optical reconstruction microscopy (STORM). *Nat Meth* 2006, 3:793-796.

37. Hess ST, Girirajan TPK, Mason MD: Ultra-High Resolution Imaging by Fluorescence Photoactivation Localization Microscopy. 2006, 91:4258-4272.

38. Gustafsson MG: Surpassing the lateral resolution limit by a factor of two using structured illumination microscopy. *Journal of microscopy* 2000, 198:82-7.

39. Gustafsson MGL, Shao L, Carlton PM, Wang CJR, Golubovskaya IN, Cande WZ, Agard DA, Sedat JW: Three-Dimensional Resolution Doubling in Wide-Field Fluorescence Microscopy by Structured Illumination. *Biophysical Journal* 2008, 94:4957-4970.

40. Donnert G, Keller J, Wurm CA, Rizzoli SO, Westphal V, Schonle A, Jahn R, Jakobs S, Eggeling C, Hell S: Two-Color Far-Field Fluorescence Nanoscopy. *Biophysical Journal* 2007, 92:L67-L69.

41. Loose M, Kruse K, Schwille P: Protein Self-Organization: Lessons from the Min System. *Annual Review of Biophysics* 2011, 40:315-336.

42. Lutkenhaus J: Assembly Dynamics of the Bacterial MinCDE System and Spatial Regulation of the Z Ring. *Annual Review of Biochemistry* 2007, 76:539-562.

43. McEvoy AL, Greenfield D, Bates M, Liphardt J: Q&A: Single-molecule localization microscopy for biological imaging. *BMC biology* 2010, 8:106.

44. Schermelleh L, Heintzmann R, Leonhardt H: A guide to super-resolution fluorescence microscopy. 2010, 190:165-175.

45. Gustafsson MGL: Nonlinear structured-illumination microscopy: wide-field fluorescence imaging with theoretically unlimited resolution. *Proceeding of the National Academy of Science* 2005, 102:13081-13086.

46. Weiss DS, Chen JC, Ghigo JM, Boyd D, Beckwith J: Localization of FtsI (PBP3) to the septal ring requires its membrane anchor, the Z ring, FtsA, FtsQ, and FtsL. *Journal of bacteriology* 1999, 181:508-20.

47. Galli E, Gerdes K: FtsZ-ZapA-ZapB interactome of Escherichia coli. *Journal of bacteriology* 2012, 194:292-302.

48. Small E, Marrington R, Rodger A, Scott DJ, Sloan K, Roper D, Dafforn TR, Addinall SG: FtsZ polymer-bundling by the Escherichia coli ZapA orthologue, YgfE, involves a conformational change in bound GTP. *Journal of molecular biology* 2007, 369:210-21.

49. Hess Girirajan T, Mason M S: Ultra-High Resoluion Imaging by Fluorescence Photoactivation Localization Microscopy. *Biophysical Journal* 2006, 91:4258-4272.

50. Bates M, Jones SA, Zhuang X: *in Imaging : a laboratory manual (eds Yuste, R.)*. Cold Spring Harbor, N.Y.: Cold Spring Harbor Laboratory Press; 2011:547-576.

51. Varma A, Young KD: In Escherichia coli, MreB and FtsZ direct the synthesis of lateral cell wall via independent pathways that require PBP 2. *Journal of bacteriology* 2009, 191:3526-33.

52. Monahan LG, Robinson A, Harry EJ: Lateral FtsZ association and the assembly of the cytokinetic Z ring in bacteria. *Molecular microbiology* 2009, 74:1004-17.

53. Blaauwen TD, Buddelmeijer N, Mirjam EG, Hameete CM, Nanninga N: Timing of FtsZ Assembly in Escherichia coli Timing of FtsZ Assembly in Escherichia coli. *Society* 1999, 181.

54. Adler HI, Fisher WD, Cohen A, Hardigree AA: Miniture Escherichia coli Cells Deficient in DNA. *PNAS* 1966, 6:321-326.

55. Bernhardt TG, de Boer P a J: SlmA, a nucleoid-associated, FtsZ binding protein required for blocking septal ring assembly over Chromosomes in E. coli. *Molecular cell* 2005, 18:555-64.

56. Cho H, McManus HR, Dove SL, Bernhardt TG: Nucleoid occlusion factor SlmA is a DNA-activated FtsZ polymerization antagonist. *Proceedings of the National Academy of Sciences of the United States of America* 2011, 108:3773-8.

57. Wu LJ, Errington J: Coordination of cell division and chromosome segregation by a nucleoid occlusion protein in Bacillus subtilis. *Cell* 2004, 117:915-25.

58. Akerlund T, Bernander R, Nordström K: Cell division in Escherichia coli minB mutants. *Molecular microbiology* 1992, 6:2073-83.

59. Khlebnikov a, Datsenko K a, Skaug T, Wanner BL, Keasling JD: Homogeneous expression of the P(BAD) promoter in Escherichia coli by constitutive expression of the low-affinity high-capacity AraE transporter. *Microbiology (Reading, England)* 2001, 147:3241-7.

60. Baba T, Ara T, Hasegawa M, Takai Y, Okumura Y, Baba M, Datsenko K a, Tomita M, Wanner BL, Mori H: Construction of Escherichia coli K-12 in-frame, single-gene knockout mutants: the Keio collection. *Molecular systems biology* 2006, 2:2006.0008.

61. Cherepanov PP, Wackernagel W: Gene disruption in Escherichia coli : T c R and K m R cassettes with the option of Flp-catalyzed excision of the antibiotic-resistance determinant. *Structure* 1995, 158:9-14.

62. Pichoff S, Vollrath B: Deletion analysis of gene minE which encodes the topological specificity factor of cell division in Escherichia coil. *Molecular Microbiology* 1995, 18:321-329.

63. Iafolla M a J, Mazumder M, Sardana V, Velauthapillai T, Pannu K, McMillen DR: Dark proteins: effect of inclusion body formation on quantification of protein expression. *Proteins* 2008, 72:1233-42.

64. Neidhardt FC, Bloch PL, Smith DF: Culture medium for enterobacteria. *Journal of bacteriology* 1974, 119:736-47.

65. Cogger VC, McNerney GP, Nyunt T, DeLeve LD, McCourt P, Smedsrod B, Le Couteur DG, Huser TR: Three dimensional structured illumination microscopy of liver sinusoidal endothelial cell fenestrations. *Journal of Structural Biology* 2010, 171:382-388.

66. Addinall SG, Bi E, Lutkenhaus JOE: FtsZ Ring Formation in fts Mutants. *Microbiology* 1996, 178:3877-3884.

67. Greenfield D, McEvoy AL, Shroff H, Crooks GE, Wingreen NS, Betzig E, Liphardt J: Self-organization of the Escherichia coli chemotaxis network imaged with super-resolution light microscopy. *PLoS biology* 2009, 7:e1000137.

68. Shroff Galbriath, C., Galbraith, J., White, H., Gillette, J., Olenych, S., Davidson, M., Betzig, E. H: Dual-color supperresolution imaging of genetically expressed probes within individual adhesion complexes. *Proceeding of the National Academy of Science* 2007, 104:20308-20313.

69. Bates M, Huang B, Dempsey GT, Zhuang X: Multicolor Super-Resolution Imaging with Photo-Switchable Fluorescent Probes. *Science* 2007, 317:1749-1753.

70. Huang B, Wang W, Bates M, Zhuang X: Three-Dimensional Super-Resolution Imaging by Stochastic Optical Reconstruction Microscopy. *Science* 2008, 319:810-813.

Chapter 5

mMaple: A Photoconvertible Fluorescent Protein for Use in Multiple Conventional and Super-resolution Imaging Modalities

5.1 Summary

Recent developments in optical microscopy allow specific labels to be imaged with nanometer scale resolution. These different "super-resolution" imaging approaches require fluorescent probes with distinct and seemingly incompatible properties. Here, we report an engineered photoconvertible fluorescent protein (pcFP) variant, designated mMaple, that is well suited for use in multiple, complementary super-resolution imaging modalities, specifically structured illumination microscopy (SIM) and single-molecule localization microscopy, e.g. PALM (photoactivated localization microscopy) and STORM (stochastic optical reconstruction microscopy). We empirically demonstrate the versatility of mMaple by obtaining super-resolution images of protein organization in both bacterial and mammalian cells. Compared to alternative pcFPs, mMaple has higher photoconversion contrast, improved photostability of the green state, and a dramatic increase in the steady state intracellular protein concentration. This latter property is evident in the 7-fold increase in the number of proteins observed for mMaple relative to mEos2 when expressed under identical conditions in *Escherichia coli*. mMaple thus enables fast live-cell ensemble imaging and yet provides outstanding high precision single molecule localization.

5.2 Introduction

A new generation of fluorescence microscopes is capable of imaging with nanometer-scale resolution. These "super-resolution" microscopes are now commercially available and poised to become standard fixtures in imaging facilities and laboratories worldwide [1, 2]. Single-molecule localization techniques such as photoactivated localization microscopy (PALM) [3], stochastic optical reconstruction microscopy (STORM) [4], and fluorescence-PALM (f-PALM) [5] (collectively referred to as (f-)PALM/STORM) provide information on the positions of many individual fluorophores within the sample at high precision, producing an image with high resolution (~ 25 nm laterally [3–5] and ~10 – 50 nm axially [6–8]) and enabling sub-diffraction limit imaging of cellular ultrastructure and quantitative analysis of protein distributions [9]. The very highest localization precisions are most readily achieved for thin samples in proximity to the coverslip, however this limitation has been circumvented in certain implementations [8, 10]. The requirement to sequentially read out fluorophore positions, one by one, limits the rate at which (f-)PALM/STORM images are acquired. The highest resolutions have been obtained in fixed samples [3–7, 11, 12] but technical improvements now allow living samples to

be characterized, albeit at effective frame rates on the second(s) timescale [13, 14].

By contrast, SIM and STED provide relatively high-speed image acquisition [15, 16] and also achieve sub-diffraction limit image resolution. The spatial resolution of linear SIM is physically limited to twice that of the confocal microscope (i.e., ~125 nm laterally and ~250 nm axially) [17, 18], while STED obtains diffraction-unlimited resolution, achieving 40 – 70 nm resolution in three dimensions for biological samples labeled with fluorescent dyes and proteins, depending on the specific implementation [19–22]. Characterization of live-cell protein dynamics is more tractable with these techniques; however, the highest resolutions have been obtained during fixed cell imaging [17, 18, 20, 23, 24]. Since each super-resolution implementation has its own advantages, multiple imaging modalities would ideally be used in concert for a given sample, thereby allowing investigators to watch dynamic structures assemble and move, or characterize the detailed structure of a fixed sample, without concern for FP-dependent perturbations in fusion protein localization, dynamics, folding efficiency, or expression level.

5.3 Results and Discussion

To date, there has been little progress towards developing and validating a single FP variant for use in multiple super-resolution imaging modalities. This may be attributed to different super-resolution imaging approaches requiring fluorescent probes with distinct and seemingly incompatible properties. (f-)PALM/STORM requires probes that can be switched with high contrast between two spectrally distinct states, such as photoactivatable FPs [25, 26], photoswitchable FPs [27], photoconvertible pcFPs [28–32] and organic dyes [12, 33, 34]. By contrast, SIM and STED are compatible with conventional fluorophores (e.g., enhanced green FP (EGFP) and yellow FP (YFP)) and for these methods, high fluorophore brightness and photostability are necessary for the highest resolutions. In all cases, when compared to conventional imaging techniques, super-resolution microscopy requires increased brightness and photostability of fluorescent probes.

Here we report a new green-to-red pcFP variant, known as mMaple, whose brightness and switching contrast make it a highly applicable fluorescent label for both (f-)PALM/STORM and SIM. To improve the previously reported mClavGR2 pcFP [32], we first replaced a sequence of 5 residues (residues 220 – 224; HSGLP) near the C-terminus with the corresponding residues (RNSTD) from the close homologue mTFP1 [35]. This modification was done out of concern that the HSGLP sequence, which forms part of the dimer interface in related *Anthozoa* FPs [36], could potentially cause a weak tendency to dimerize. Starting from this modified mClavGR2 variant,

we undertook 4 additional rounds of protein optimization by creating libraries of many thousands of genetic variants and then performing photoconversion-based screening in the context of bacterial colonies[32]. Colonies that exhibited both high brightness and an improved ratio of red fluorescence after photoconversion to green fluorescence before photoconversion were considered 'winners' of a given round of screening. In the final round of optimization, the winners of all previous rounds were genetically shuffled[37]. Screening of this final library led to the identification of two similar variants that retain many of the key traits of mClavGR2 (Figure 5-2; Table 5-1), including a monomeric structure at high concentrations, yet provide an improved ratio of red-to-green fluorescence during photoconversion. These two variants, designated as mMaple and mClavGR3, are equivalent to mClavGR2 with the HSGLP to RNSTD replacement and either A145V/G171S/G225S or A145V/Y173H/G225S, respectively.

Protein name	State	λ_{ex} (nm)	λ_{em} (nm)	ε[a]	Φ	Brightness[b]	pK_a
mMaple	green	489	505	15 (59)	0.74	11	8.2
	red	566	583	30	0.56	17	7.3
mClavGR3	green	489	505	13 (58)	0.70	9	8.2
	red	566	583	28	0.57	16	7.3
mClavGR2	green	488	504	19 (60)	0.77	15	8.0
	red	566	583	32	0.54	17	7.3
mEos2	green	506	519	78 (95)	0.43	34	5.6[c]
	red	573	584	39	0.35	14	6.4[c]

Table 5-1. Properties of mMaple and related variants.

[a]Extinction coefficent (mM^{-1} cm^{-1}) at peak absorbance wavelength in PBS (pH 7.4). Value in parentheses was determined at pH 10. [b]Product of ε and Φ in mM^{-1} cm^{-1}. For comparison, the brightness of EGFP and mCherry are 34 mM^{-1} cm^{-1} and 16 mM^{-1} cm^{-1}, respectively [37]. [c]Data from McKinney *et al.*[31].

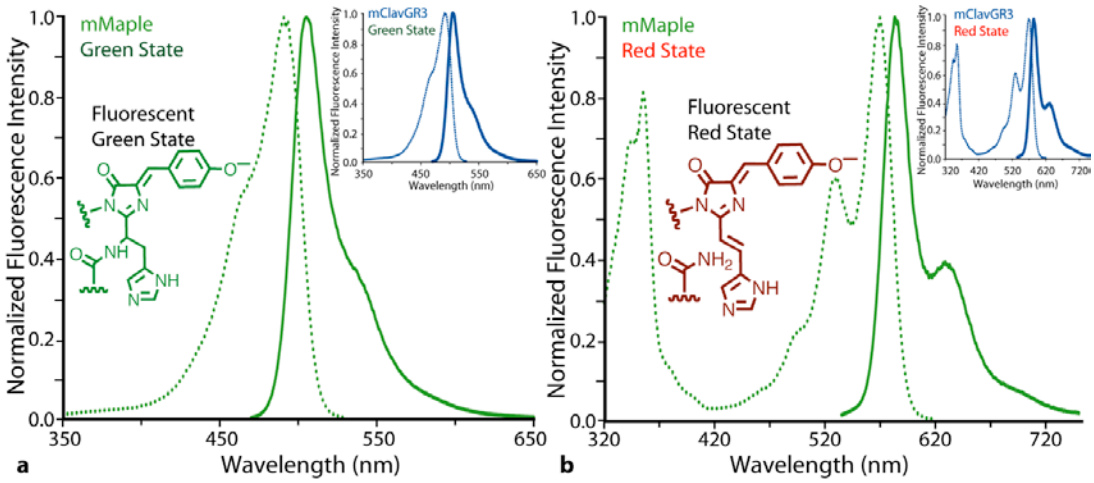

Figure 5-2. Spectral characterization of mMaple and mClavGR3. (**a**) Excitation and emission spectra of the pre-photoconversion green state of mMaple and mClavGR3 (inset). (**b**) Excitation and emission spectra of the post-photoconversion red state of mMaple and mClavGR3 (inset).

In vitro characterization revealed that the primary difference between mMaple, mClavGR3, and the earlier mClavGR2 variant is a shift in the ground state equilibrium of the green state chromophore from the phenolate form (absorbance λ_{max} = 489 nm) towards the phenol form (absorbance λ_{max} = 380 nm) (Figure 5-3a). This shift is attributed to an increase in the apparent pK_a of the green state chromophore from 8.0 to 8.2 (Table 5-1; Figure 5-4). The increased population of the phenol form explains the improved photoconversion contrast of mMaple (Figure 5-3b), since it is excitation of the phenol form that initiates the green-to-red photoconversion. Critically, the post-conversion red state retains the same pK_a as mClavGR2 (7.3), so the population of the red fluorescent phenolate form remains unchanged (Table 5-1). We speculate that the A145V mutation is primarily responsible for the shift of the green state pK_a, since position 145 is located immediately adjacent to the tyrosine-derived phenolate moiety of the chomophore. Although it does not directly interact with the chromophore, the bulkier side chain of valine may stabilize the protonated state by decreasing the solvent accessibility of the chromophore. Notably, position 145 is occupied by Pro in all other pcFPs except Kaede[28], which has Ala at this position. The effect of the additional mutations is currently unclear, as they are relatively remote from the chromophore. In terms of the rate of chromophore maturation, protein folding efficiency, and rate of photobleaching, mMaple behaves similarly to its mClavGR2 precursor (Figures 5-5—5-7; Table 5-8). Relative to mEos2, both mMaple and mClavGR2 exhibit a substantial improvement in the apparent photostability of the green state under widefield imaging conditions (14× and 15× at 11.4 mW/cm², respectively) (Figures 5-6, 5-7) and a substantially improved folding efficiency *in vivo* (Figures 5-5b,c).

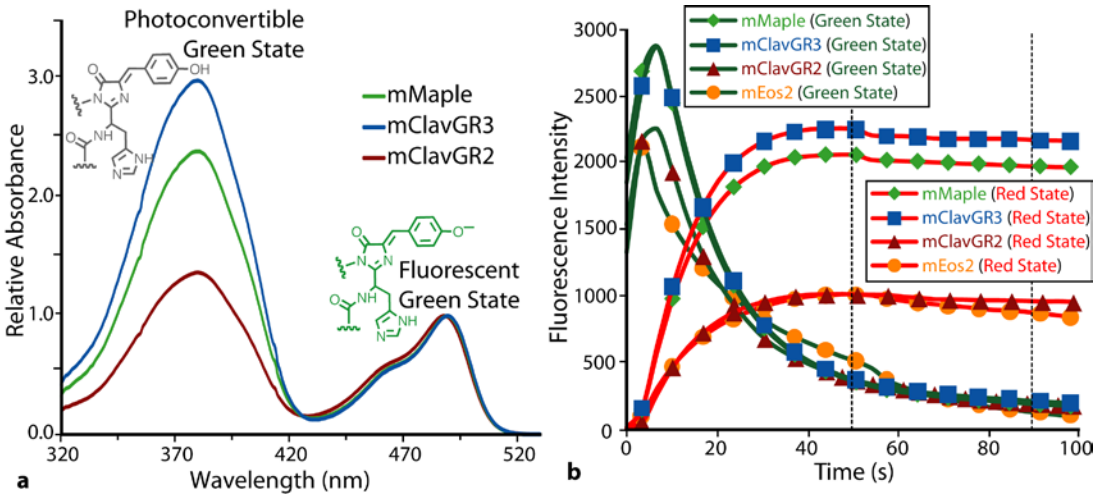

Figure 5-3. ***In vitro*** **characterization of mClavGR2 and its improved variants.** (**a**) Absorbance spectra of mClavGR2 (red line), mMaple (green line), and mClavGR3 (blue line). Absorbance spectra are normalized to absorbance at 488 nm or 489 nm. (**b**) Photoconversion from the green state (green lines) to the red state (red lines) of mMaple (diamonds), mClavGR3 (squares), mClavGR2 (triangles), and mEos2 (circles). The red-to-green contrast has been calculated at 47 s and 91 s (indicated with vertical dotted lines). At 47 s the contrast is 5.3 for mMaple, 5.5 for mClavGR3, 2.1 for mClavGR2, and 1.8 for mEos2. At 91 s the contrast is 10.8 for mMaple, 10.2 for mClavGR3, 4.7 for mClavGR2, and 6.9 for mEos2.

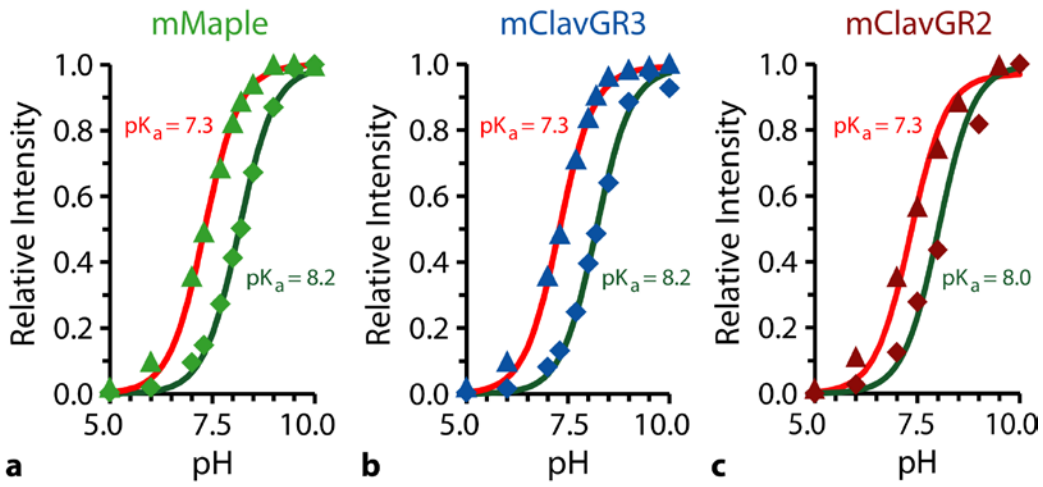

Figure 5-4. pH titrations of pcFP variants. For each variant the fluorescent intensity at pH values ranging from 5 to 10 was determined by diluting purified protein into concentrated buffer adjusted to the appropriate pH. For the green state (green line, diamond symbols), the λ_{ex} = 440 nm and the λ_{em} = 530 nm. For the red state (red line, triangle symbols), the λ_{ex} = 540 nm and the λ_{em} = 630 nm. (**a**) mMaple. (**b**) mClavGR3. (**c**) mClavGR2.

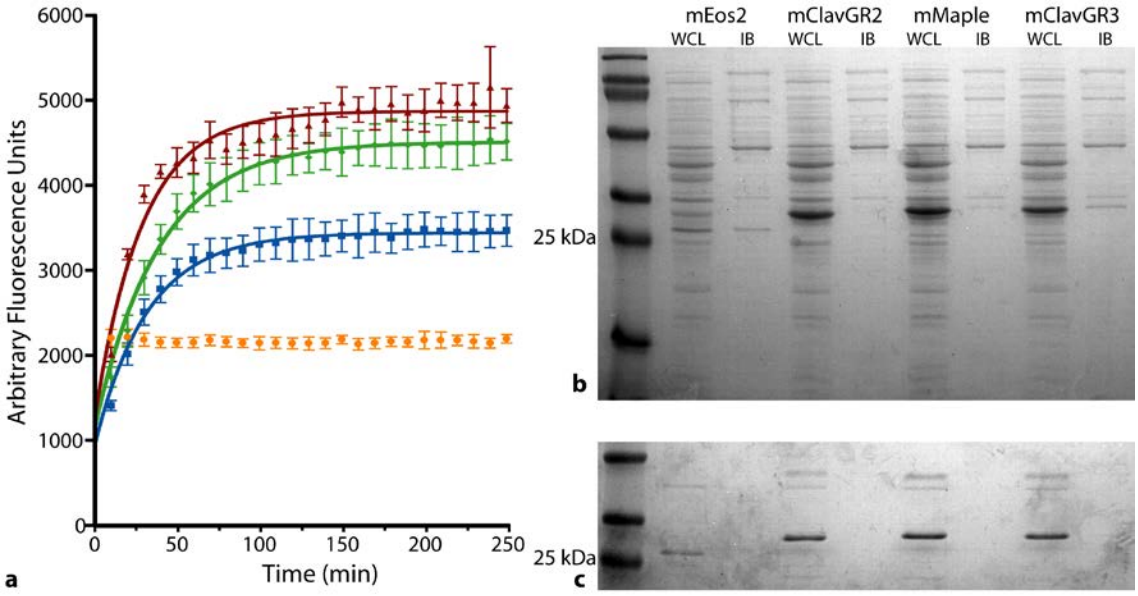

Figure 5-5. Expression and maturation of new pcFPs expressed in *E. coli*. (**a**) Maturation of mClavGR variants and mEos2 at 37 °C. The maturation profiles of mClavGR2 (dark red), mMaple (green), and mClavGR3 (blue) can be fit as monoexponential curves with time constants of 29 min, 39 min and 32 min, respectively. Under the conditions of this experiment, mEos2 (orange) is approximately 50% as bright as mMaple and, in agreement with our previous results{Hoi 2010}, appears to have fully matured prior to the initial measurement. Each curve represents the average of six independent measurements and error bars represent standard deviations. (**b**) SDS-PAGE of the soluble and insoluble fractions of *E. coli* expressing pcFPs described in this work. Lane 1 is the protein ladder. For each construct, one lane corresponds to the whole cell lysate (WCL) and the other lane corresponds to protein from inclusion bodies (IB). The relative intensity of FP bands in the WCL and IB fractions, respectively, are: 17 and 7 for mEos2; 100 and 0 for mClavGR2; 113 and 0 for mMaple; and 77 and 18 for mClavGR3. Overall, mMaple shows the highest expression and folding efficiency with 100% of the protein in the soluble fraction, while mEos2 has the lowest expression and folding efficiency with 29% of the total expressed protein located in the IB fraction. (**c**) The same samples as in (**b**), following purification by Ni^{2+}/NTA affinity chromatography.

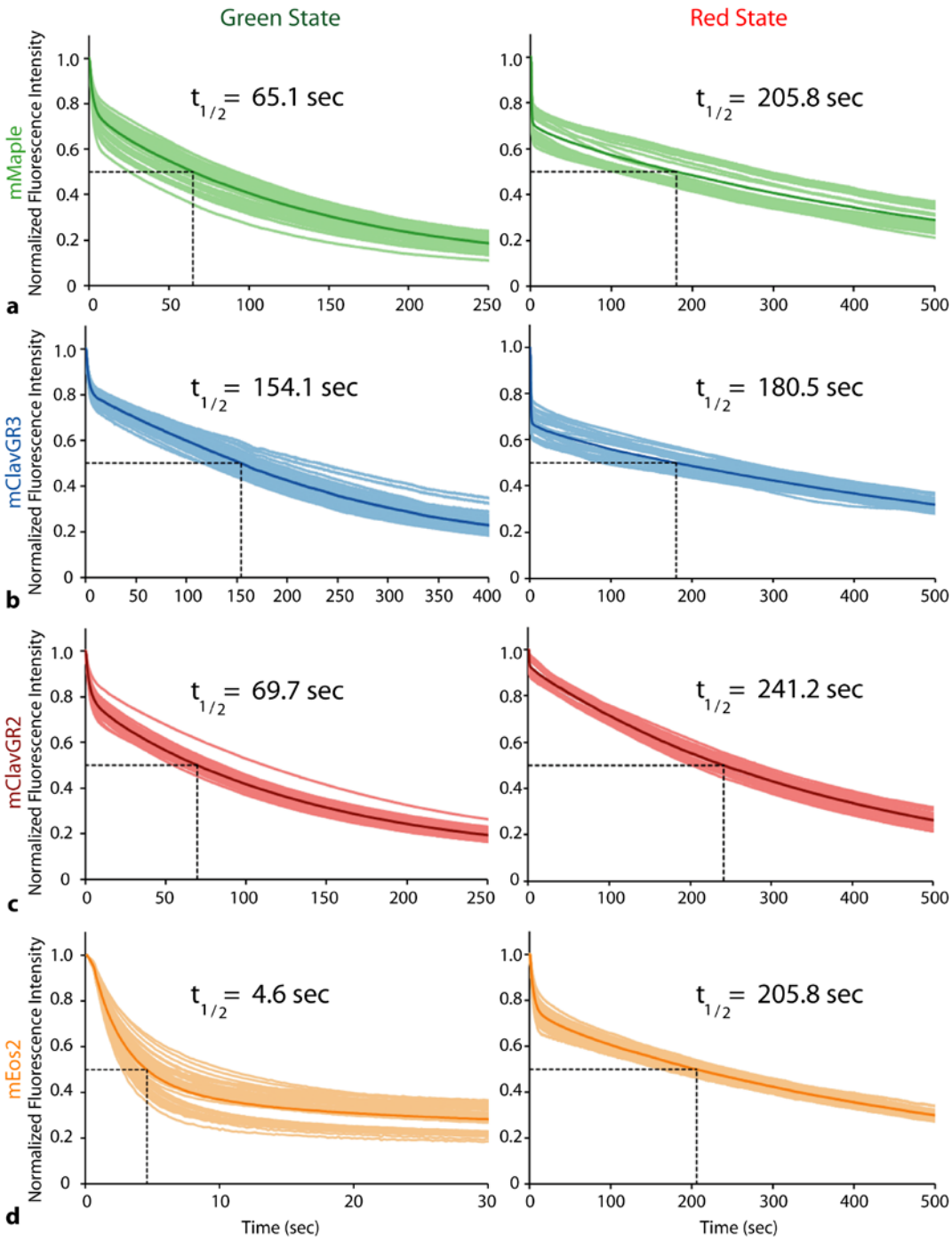

Figure 5-6. Widefield imaging photobleaching curves for pcFP-H2B fusions in live cells. Photobleaching curves of the green state (left panels) and the red state (right panels) of pcFPs under widefield condition. Each curve represents the photobleaching behavior of an individual cell and the darker colored curve is the average. Average time when the fluorescence intensity of the green states (left panels) decreased to half of the initial intensity are 65.1 sec for mMaple (**a**) (45 cells),

154.1 sec for mClavGR3 (**b**) (52 cells), 69.7 sec for mClavGR2 (**c**) (42 cells), and 4.6 sec for mEos2 (**d**) (48 cells). The average time for the red state is 180.3 sec for mMaple (**a**) (36 cells), 180.5 sec for mClavGR3 (**b**) (38 cells), 241.2 sec for mClavGR2 (**c**) (35 cells), and 205.8 sec for mEos2 (d) (49 cells). Values have been tabulated in Table 5-8.

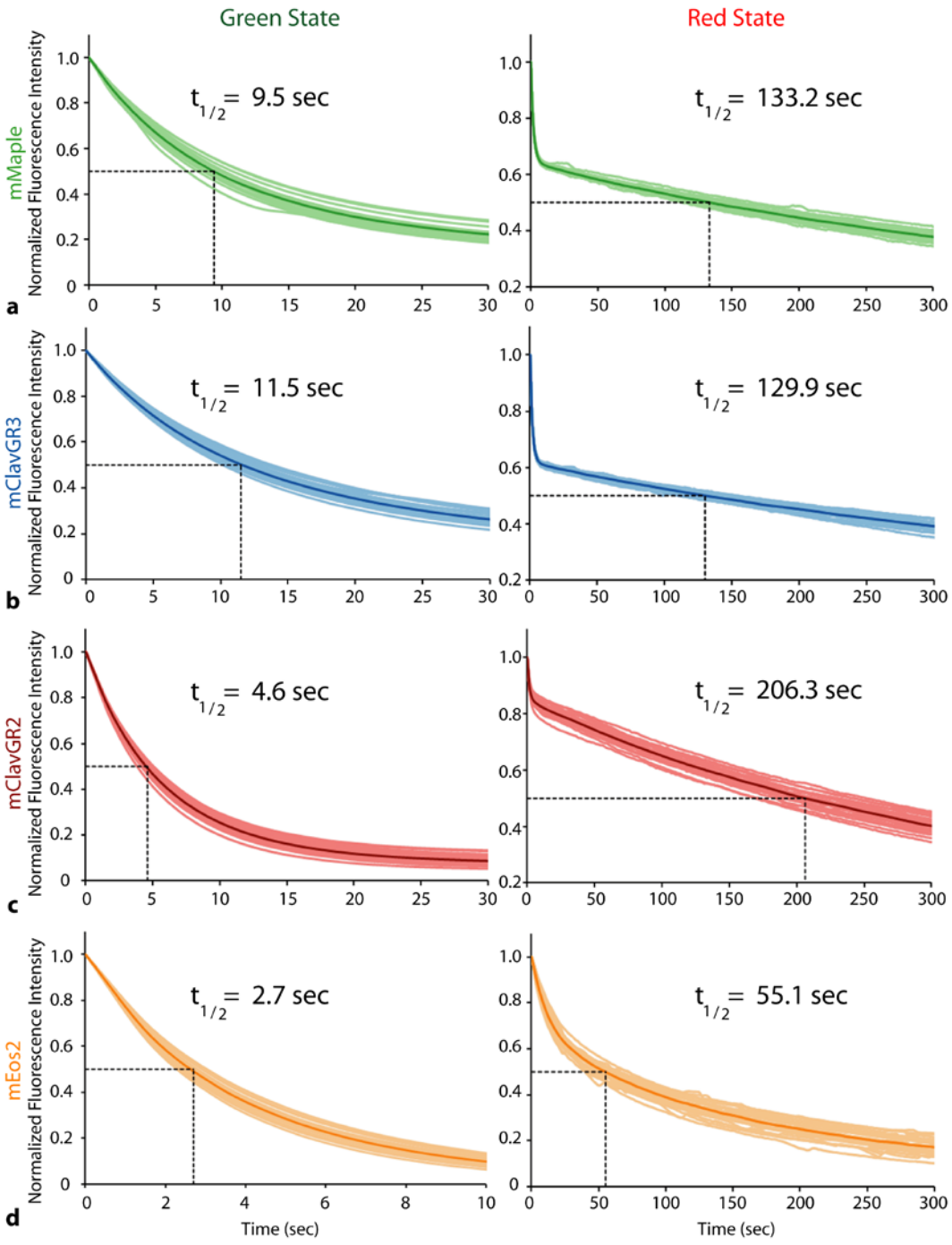

Figure 5-7. Confocal imaging photobleaching curves for pcFP-H2B fusions in live cells. Photobleaching curves of the green states (left panels) and the red states (right panels) of pcFPs under confocal condition. Each curve represents the photobleaching behavior of an individual cell and the dark colored curve is the average. Average time for the green state fluorescence intensity to decrease to half of the initial intensity are 9.4 sec for mMaple (**a**) (22 cells), 11.5 sec for mClavGR3 (**b**) (30 cells), 4.6

sec for mClavGR2 (**c**) (30 cells), and 2.7 sec for mEos2 (**d**) (28 cells). The average time for the red state fluorescence intensity to decrease by half is 133.2 sec for mMaple (**a**) (27 cells), 129.9 sec for mClavGR3 (**b**) (25 cells), 206.3 sec for mClavGR2 (**c**) (23 cells) and 55.1 sec for mEos2 (**d**) (25 cells). Values have been tabulated in Table 5-8.

Protein name	State	Time to bleach to 50% of initial intensity (s)	
		Widefield imaging conditions[a]	Confocal imaging conditions[b]
mMaple	green	65.1	9.4
	red	180.3	133.2
mClavGR3	green	154.1	11.5
	red	180.5	129.9
mClavGR2	green	69.7	4.6
	red	241.2	206.3
mEos2	green	4.6	2.7
	red	205.8	55.1

Table 5-8. Characterization of photobleaching rates for pcFP-H2B fusions in live cells.

[a]Widefield photobleaching of both states was performed at an output power of 11.4 mW/cm². [b]Confocal photobleaching of both states was performed at an output power of 120 μW. All photobleaching curves are provided in Supplementary Fig. S6 and S7. We have previously reported [32] widefield (at 202.6 mW/cm² and 489.9 mW/cm² for green and red, respectively) and confocal (at 100 μW for both green and red) photobleaching times for mClavGR2 and mEos2 using units of "time to photobleach from 1000 to 500 photons/second/molecule". We have since observed that the relative order of photobleaching half-times for different variants can change as a function of power. Accordingly, the numbers provided here are only relevant for the output power at which they were measured.

To quantify the performance of mMaple relative to mEos2 [31] and mClavGR2 for super-resolution imaging applications, we prepared plasmids encoding fusions to the *Escherichia coli* chemotaxis protein CheW under control of an L-arabinose inducible promoter. This model system is useful for characterizing fluorescent fusion proteins due to a number of important advantages including titratable expression levels, a sensitive functional assay, and a characteristic pattern of dense protein localizations at the cell poles [9]. When expressed in a *cheW* knockout strain, each pcFP-CheW fusion recovers the strain's chemotaxis ability to approximately 65% that of wildtype swarming (Figure 5-9). Imaging the green state fluorescence of the Δ*cheW E. coli* strains transformed with each of the CheW fusions revealed that all constructs exhibited the correct localization pattern, but the mMaple construct was notable for its exceptional brightness relative to both mEos2 and EGFP, while maintaining the correct localization pattern at high concentrations (Figures 5-10a,b; Figure 5-11a). Consideration of only the inherent *in vitro* properties of mMaple (Table 5-1) did not provide an explanation for the apparent improvement of the *in vivo* brightness, so we began to suspect that mMaple exhibits substantially higher folding efficiency or is reaching higher intracellular concentrations than EGFP or other pcFPs under investigation.

The high apparent brightness of the green state of mMaple prompted us to attempt 3-dimensional SIM reconstructions of live *E. coli* expressing either mMaple-CheW or GFP-CheW (Figures 5-10c-e). To produce images of similar quality, the GFP-CheW construct was expressed at 100× higher induction, which is consistent with the optimal induction levels for swarming for both constructs (Figure 5-9). Attempts to acquire analogous data sets with mEos2 were unsuccessful due to rapid photobleaching of the green state (Figures 5-6, 5-7; Table 5-8). To ensure that the usefulness of mMaple for SIM imaging was not limited to this construct, we processed SIM data sets for mMaple-*α*-actinin in fixed human testicular embryonal carcinoma (NT2) cells and obtained quality reconstructions with the expected localization pattern (Figure 5-10f). We also attempted SIM imaging of mClavGR3-paxillin expressed in NT2 cells, and found that the green state was bright and photostable enough to obtain satisfactory reconstructions (Figure 5-11d). However, the mClavGR3 signal was somewhat dimmer than that of mMaple (though brighter than both mClavGR2 and mEos2) and images with quality comparable to those of mMaple were not obtained.

To characterize mMaple's post-photoconversion red fluorescent state, we imaged *E. coli* and mammalian cells expressing pcFP fusions using (f-)PALM/STORM. (f-)PALM/STORM images have the added benefit of allowing for quantification of the number of pcFPs observed, perhaps giving insight into why mMaple appears brighter than other pcFPs *in vivo*. To quantify the number of

proteins observed for each construct, we imaged fixed Δ*cheW E. coli* expressing CheW fusions to mMaple, mClavGR3, mClavGR2, or mEos2 at optimal induction levels using a custom built (f-)PALM/STORM microscope [38]. In all 4 cases, composite images revealed that the subcellular CheW distribution could be constructed from localizing hundreds of single proteins per cell (Figure 5-12b; Figure 5-11b,c). The mean number of photons emitted by each construct in the red state were similar, allowing for similar localization precision for all constructs [39] (Figure 5-12c; Figure 5-13). Consistent with our results from SIM imaging, mMaple (and mClavGR3) fusions expressed in mammalian cells enabled the acquisition of (f-)PALM/STORM images that, as expected, were judged to be of equal quality to images obtained with mEos2 (Figures 5-12d,e; Figure 5-11e).

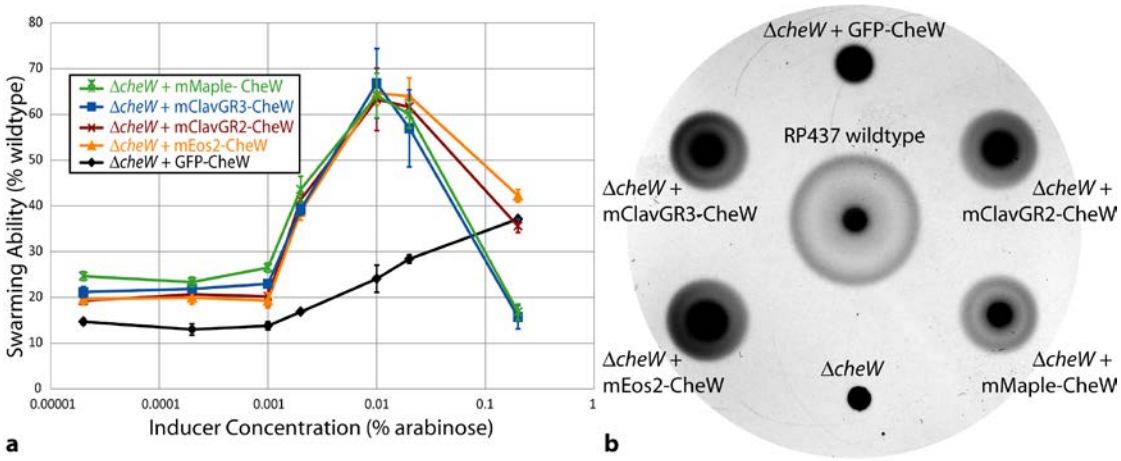

Figure 5-9. Swarm plate assays to assess the function of CheW fusions. Approximately 2 μl of Δ*cheW E. coli* transformed with a plasmid encoding a FP-CheW fusion were placed on T-broth soft agar swarm plates. The ability for the *E. coli* to undergo chemotaxis was assessed by measuring the diameter of the swarm ring 5 h after the bacteria were placed on the agar at 30 °C. The Δ*cheW* strain has no apparent swarm ring and strain RP437 exhibits the wild-type swarm ring. Interestingly, fusions with all of the pcFPs used in this work are able to rescue the swarming phenotype more effectively than the analogous GFP fusion. (**a**) Swarming ability as a percentage of wild-type for bacteria expressing mMaple, mClavGR3, mClavGR2, mEos2, or GFP fused to CheW. Excessively high concentrations of CheW can disrupt swarming ability, and thus the size of swarm rings will decrease at high inducer concentration{Sanders 1989}. Error bars are standard error, N = 3 measurements. (**b**) Image of a representative agar plate (0.01% L-arabinose concentration) showing swarm rings for each of the constructs mentioned above.

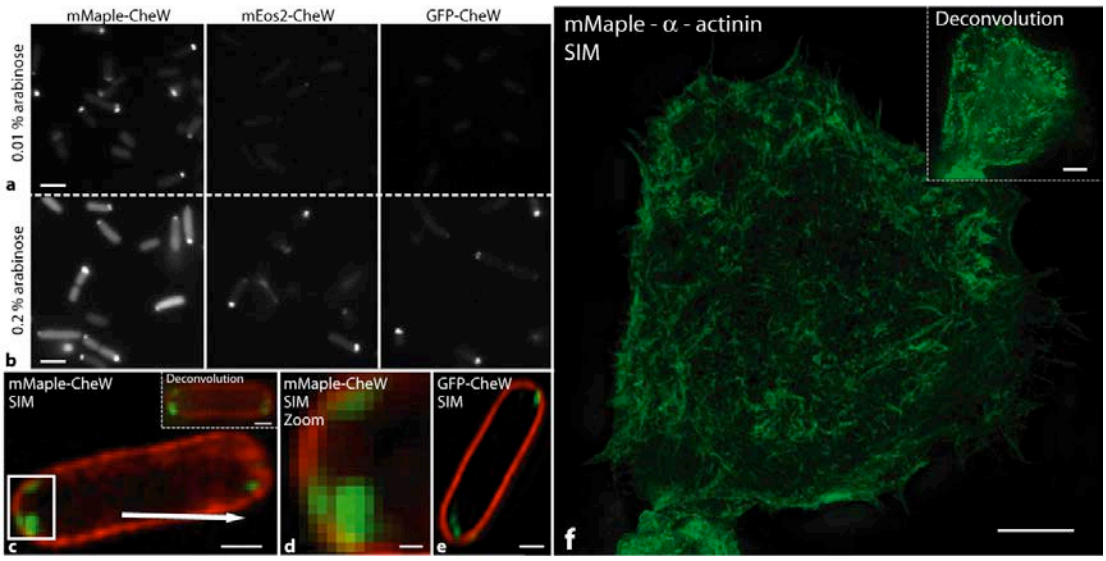

Figure 5-10. mMaple has improved *in vivo* brightness and enables 3D-SIM reconstructions *E. coli* was transformed with plasmids encoding CheW fusion proteins and cultures were induced with (**a**) 0.01% L-arabinose and (**b**) 0.2% L-arabinose for 3 h at 30 °C and then imaged using 488 nm excitation. Note the brightness of the cells expressing mMaple fusions and the large percentage of cells with the correct polar localization pattern. (**c**) Δ*cheW E.coli* expressing mMaple-CheW and a zoom (**d**) of the polar region of the cell denoted by the boxed region in (**c**). (**e**) One 125 nm slice of the 3D-SIM reconstruction of a Δ*cheW E. coli* expressing GFP-CheW. Red represents fluorescence of the membrane-specific dye FM4-64 and green represents FP fluorescence. 2D projection of 3D-SIM reconstruction of mMaple-*α*-actinin (**f**) expressed in a human testicular embryonal carcinoma (NT2) cells. The resolution of the SIM reconstruction is approximately 125 nm laterally (in x and y) and 250 nm axially (in z), with 125 nm step sizes in z. The diffraction-limited deconvolution image is included for comparison in the dotted-line boxed region with a step size of 250 nm.

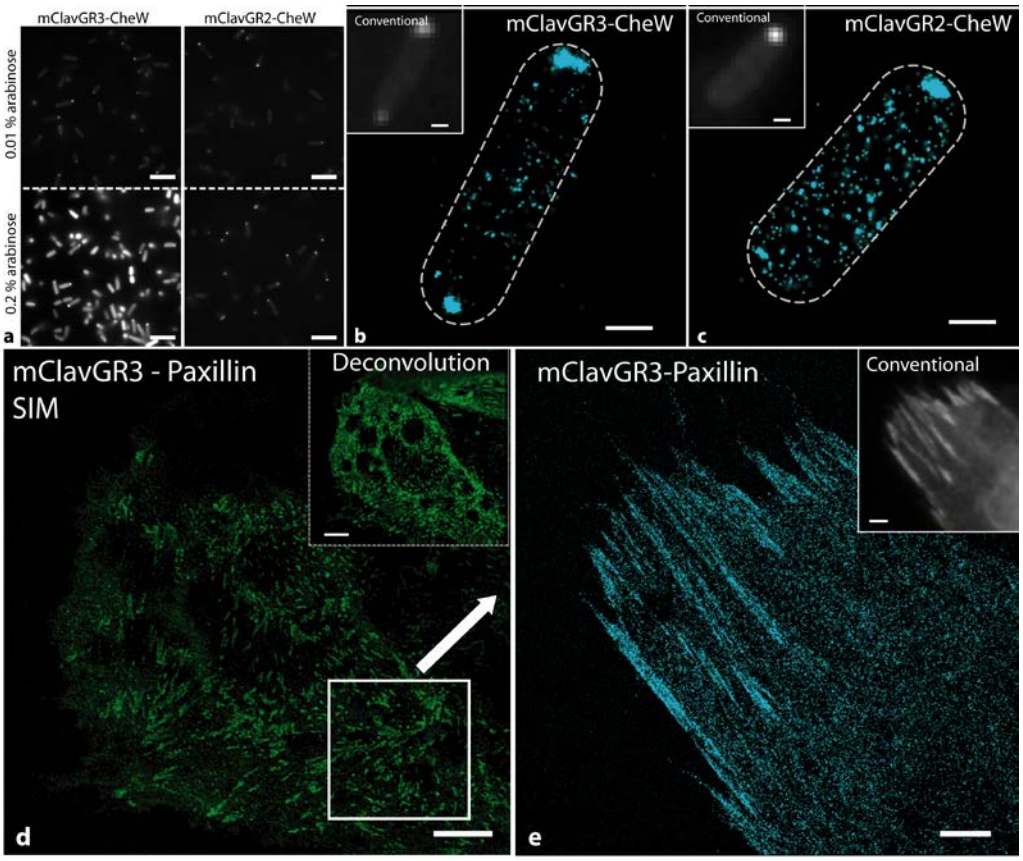

Figure 5-11. Imaging of mClavGR3 and mClavGR2 fusions in *E. coli* and mammalian cells. *E. coli* was transformed with plasmids encoding CheW fusion proteins and cultures were induced with (**a**) 0.01% L-arabinose and 0.2% L-arabinose for 3 h at 30 °C and then imaged using 488 nm excitation. (**b**,**c**) Images of Δ*cheW E.coli* expressing CheW fusion proteins at arabinose concentrations optimal for swarming. Images contain (**b**) 2133 mClavGR3-CheW localizations and (**c**) 694 mClavGR2-CheW localizations. (**d**) 2D projection of 3D-SIM reconstruction of mClavGR3-paxillin expressed in a human testicular embryonal carcinoma (NT2) cells. A diffraction-limited deconvolution image is included for comparison in the dotted-line boxed regions with a step size of 250 nm. Note that the larger z step size causes additional fluorescence signal to be included from deeper into the cell. (**e**) (f-)PALM/STORM image of mClavGR3-paxillin expressed in a human testicular embryonal carcinoma (NT2) cell. Scale bars are 2 μm (**a**), 500 nm (**b**,**c**) and 5 μm (**d**,**e**).

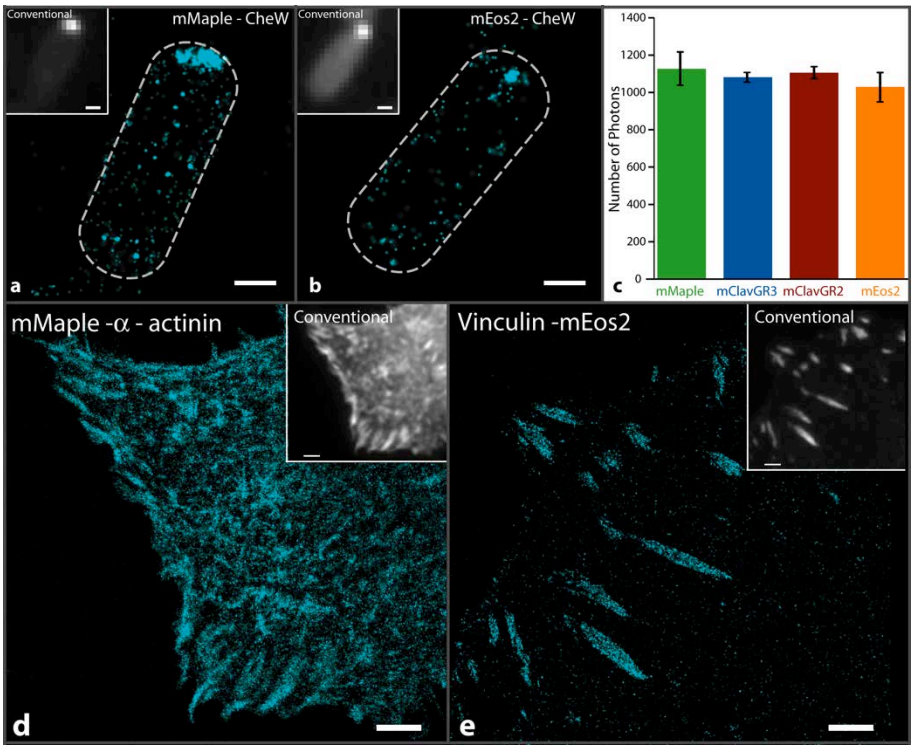

Figure 5-12. (f-)PALM/STORM characterization of mMaple and mEos2. (**a**,**b**) Images of Δ*cheW E.coli* expressing CheW fusion proteins at L-arabinose concentrations optimal for swarming. Images contain (**a**) 1086 mMaple localizations and (**b**) 229 mEos2 localizations. (**c**) The mean number of photons emitted by each construct (error is standard error, N = 3 independent measurements from distributions consisting of 4,000 – 32,000 localizations). (**d**,**e**) Images of mammalian cells expressing mMaple-α-actinin (**c**) and vinculin-mEos2 (**d**). Conventional epi-fluorescence images of the green state of the pcFP are shown in the white boxes in (**a**,**b**,**d**,**e**).

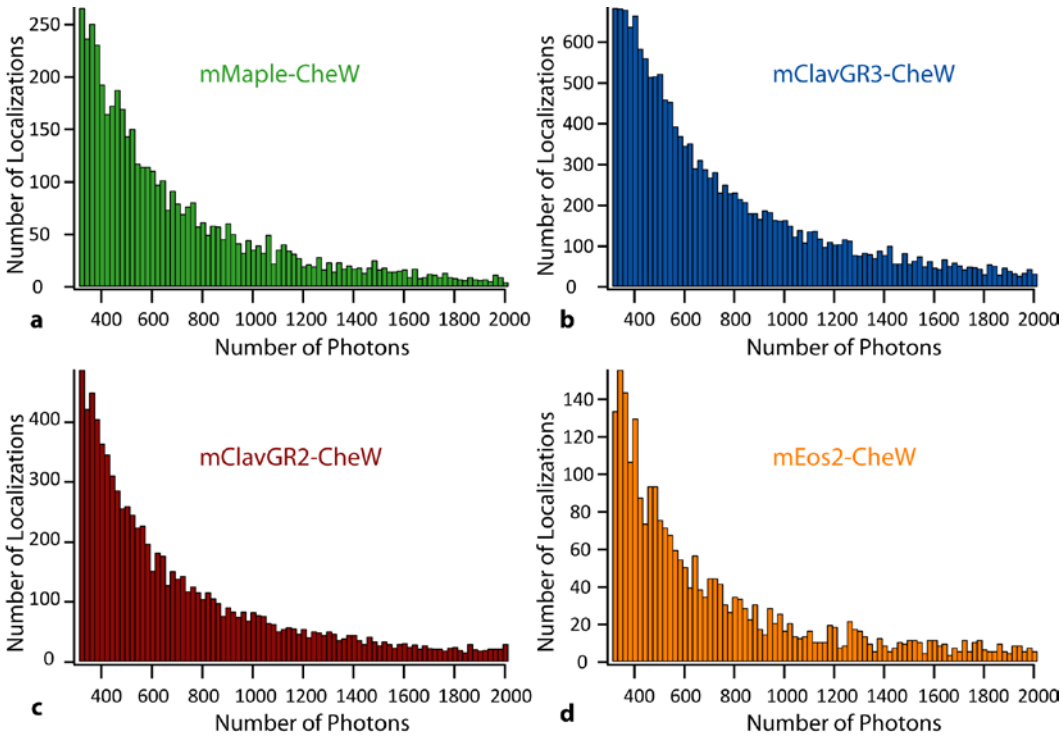

Figure 5-13. Number of photons emitted by pcFPs fused to CheW. Representative distributions of the number of photons emitted in the red fluorescent state by CheW fusions to (**a**) mMaple (**b**) mClavGR3, (**c**) mClavGR2 and (**d**) mEos2. Only localizations emitting more than 300 photons were included.

The most striking difference among the pcFPs was that mMaple reliably provided more protein localizations than mEos2 or mClavGR2 per cell (3.4× and 2.3×, respectively) under identical growth and imaging conditions. At native expression levels, each cell should contain approximately 6000 CheW proteins [40]. However, since the depth of field of the objective restricts the observable proteins to the bottom ~40% of the cell, approximately 2400 CheW proteins should be imaged. On average, we observe 927 ± 547 mMaple-CheW localizations (N = 45 cells), 895 ± 467 mClavGR3-CheW localizations (N = 52 cells), 396 ± 181 mClavGR2-CheW localizations (N = 48 cells), and 269 ± 113 mEos2-CheW localizations (N = 38 cells) per cell (Figure 5-14). Therefore, the number of observable mMaple-CheW localizations is more consistent with native levels of CheW expression than either mClavGR2 or mEos2, though they are being expressed at the same level. To ensure that the higher number of localizations is not fusion specific, we imaged each pcFP inside fixed wildtype *E. coli* with no binding partner (Figures 5-15a-b; left panels). In this case, we obtain approximately 10× the number of localizations per cell for mMaple expressing cells (3497 ± 1641) relative to mEos2 expressing cells (209 ± 86) (Figure 5-15c).

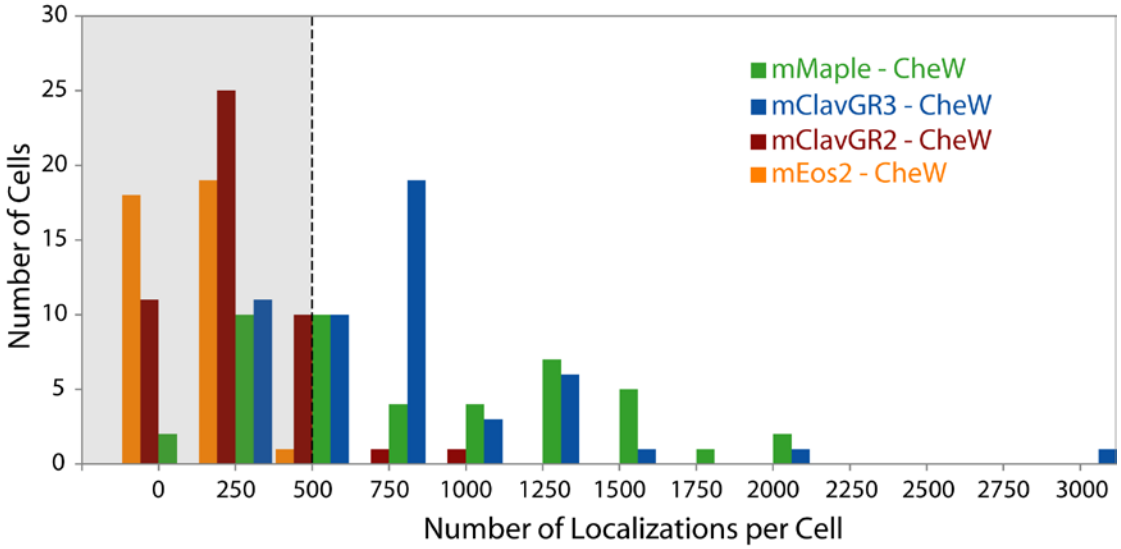

Figure 5-14. Number of localizations for pcFPs fused to CheW. Distribution of the number of localizations observed for Δ*cheW E. coli* cells containing CheW fusions to mMaple, mClavGR3, mClavGR2, and mEos2. Greater than 96% of cells expressing either mEos2- or mClavGR2-CheW fusions have less than 500 localizations (boxed region), whereas greater than 50% of cells expressing either mMaple or mClavGR3 CheW fusions have more than 500 localizations.

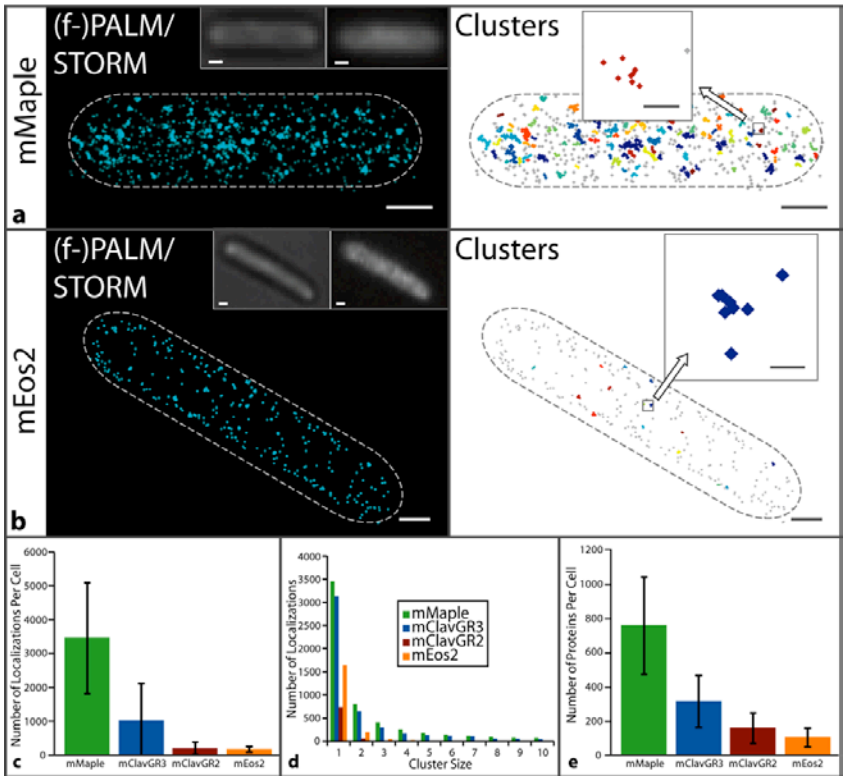

Figure 5-15. (f-)PALM/STORM characterization of the number of observed localizations and proteins per cell. (a,b) (f-)PALM/STORM images of fixed *E. coli* expressing cytoplasmic (**a**) mMaple (*N* = 1696 localizations), or (**b**) mEos2 (*N* = 472 localizations). Localizations are represented as normalized 2D Gaussian peaks with widths given by their theoretical localization precisions (left panels) and plotted as small markers grouped into clusters with adjacent spacing of 30 nm or less (right panels). Individual protein localizations are shown in grey whereas closely spaced localizations (< 30 nm) are grouped into clusters of the same colour (right panels). The bright field and conventional fluorescence images are shown for comparison (left panels, left and right inset respectively). (**c**) Average number of localizations per cell for each cytoplasmically expressed pcFP. (**d**) The distribution of cluster sizes (< 30 nm interlocalization spacing) for cytoplasmically expressed pcFPs. (**e**) Average number of cytoplasmically expressed proteins per cell. Rather than counting each localization as a single molecule, we count each cluster of localizations (localizations spaced < 30 nm) as a single protein. The dotted lines in (**a,b**) denote the *E. coli* cell boundary. Scale bars are 500 nm and 50 nm (zooms). Zooms in (**a**,**b**) show possible reversible photoswitching events of single proteins. Error is the standard deviation (N = 20 cells (mMaple), N = 24 cells (mClavGR3), N = 17 cells (mClavGR2), N = 16 cells (mEos2)). The large error bars are primarily due to variation in protein expression between cells.

It has recently been reported that the red fluorescent state of mEos2 can undergo multiple cycles of reversible photoswitching into a long-lived dark state [41]. This effect is important to consider for accurate protein counting measurements using (f-)PALM/STORM images [9, 41, 42]. Our bulk *in vitro* studies demonstrate that mMaple (and mClavGR2 and mClavGR3) also exhibits reversible photoswitching of the red state (Figure 5-16). Such an effect could cause individual proteins to be counted multiple times, artificially inflating the number observed.

To investigate how reversible photoswitching may contribute to the number of observed localizations per cell, we used a previously described clustering algorithm[9] to group closely spaced protein localizations (< 30 nm interlocalization spacing, Figure 5-15a-b; right panels), and asked whether they were better explained as reversible switching of a single protein or irreversible bleaching of multiple proteins. Analysis of the (f-)PALM/STORM images of *E. coli* with cytoplasmically expressed pcFPs revealed that 56% of mMaple, 61% of mClavGR3, and over 80% of both mClavGR2 and mEos2 localizations did not have a second localization within 30 nm (Figure 5-15d; Figure 5-17). To further quantify possible reversible switching events, we purified and biotinylated mMaple and mEos2 proteins and imaged single proteins immobilized on a streptavidin-coated slide in PBS using (f-)PALM/STORM (Figure 5-18a,b). We once again grouped closely spaced protein localizations into clusters (< 30 nm interlocalization spacing) and obtained cluster size distributions for mMaple, mEos2, and the negative control in which no proteins had been added (Figure 5-18c). The background subtracted cluster size distributions for each pcFP revealed that approximately 35% of mMaple localizations and 65% of mEos2 localizations were observed as single localizations (Figure 5-18d). We conclude that, under these imaging conditions, the red fluorescent state of mMaple has a higher propensity to reversibly photoswitch than mEos2.

We next asked if reversible photoswitching could account for the differences in the number of localizations observed in *E. coli* containing different cytoplasmically expressed pcFPs. Accordingly, we reassessed the (f-)PALM/STORM images of cytoplasmic pcFPs by counting both isolated localizations and clusters of localizations (< 30 nm interlocalization spacing) as single proteins. Using this counting procedure we obtain an average number of proteins per cell for mMaple (765 ± 283) that is approximately 7× higher than for mEos2 (109 ± 55) (Figure 5-15e). Based on this result, we conclude that mMaple is able to reach higher steady state intracellular concentration of properly folded proteins compared to other pcFPs. The higher concentration of mMaple may reflect more efficient protein folding and, possibly, a decreased rate of protein turnover *in vivo*.

In conclusion, we have demonstrated that mMaple has a fortuitous combination of traits that make it useful for standard fluorescence, SIM, and (f-)PALM/STORM

imaging with performance in both super-resolution modalities that meets or exceeds that of current alternatives. We expect that this new variant will be of great utility as it allows the dynamics of protein complexes to be characterized *in vivo* with increased spatial resolution and good temporal resolution, and also allows the precise localization of the same fusion proteins to be determined with (f-)PALM/STORM. In addition, mMaple motivates a new generation of FPs that exploit the orthogonal advantages of various imaging modalities.

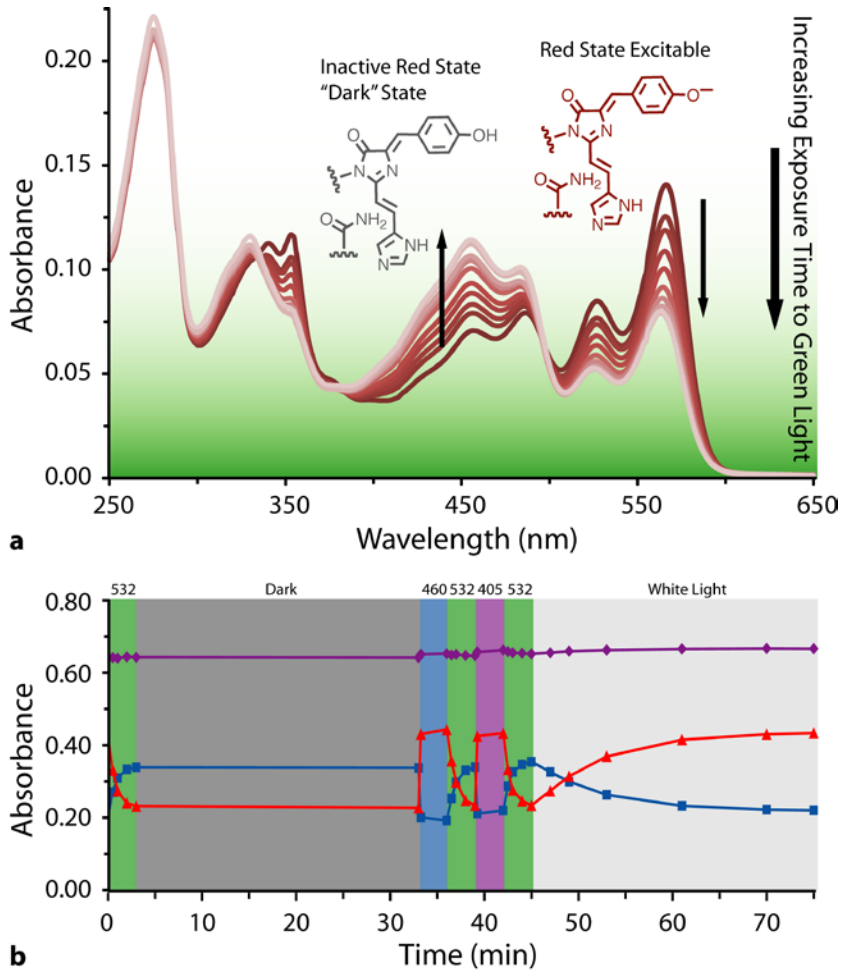

Figure 5-16. Reversible photoswitching of photoconverted (red) mMaple. (**a**) Photoconverted mMaple can be further photoconverted to a "dark" non-fluorescent state by illumination with green light. (**b**) The dark state of the photoconverted mMaple reversibly photoswitches back to the red fluorescent state as seen by changes in the absorbance spectra in response to different light sources. The absorbance at 280 nm (purple line, corresponding to total protein concentration), the absorbance at 457 nm (blue line, corresponding to the dark post-conversion red state) and the absorbance at 566 nm (red line, corresponding to the red fluorescent state of the protein) are plotted. As the protein is exposed to 532 nm light, the protein is switched from the red state to the dark state (green regions), which can be re-excited by 460 nm light (blue region), 405 nm light (violet region) and white light (light grey region). No absorbance changes were observed if the protein was kept in the dark (dark grey region). Similar results were obtained for mClavGR2 and mClavGR3.

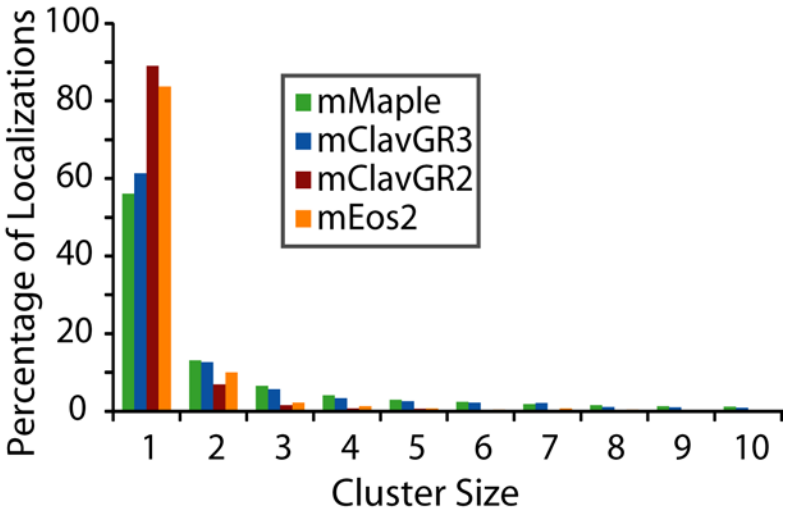

Figure 5-17. Cluster analysis of pcFP localizations. The percentage of localizations grouped into clusters (< 30 nm interlocalization spacing) for cytoplasmically expressed pcFPs. Over 50% of mMaple and mClavGR3 and over 80% of mClavGR2 and mEos2 proteins do not have a second localization within 30 nm.

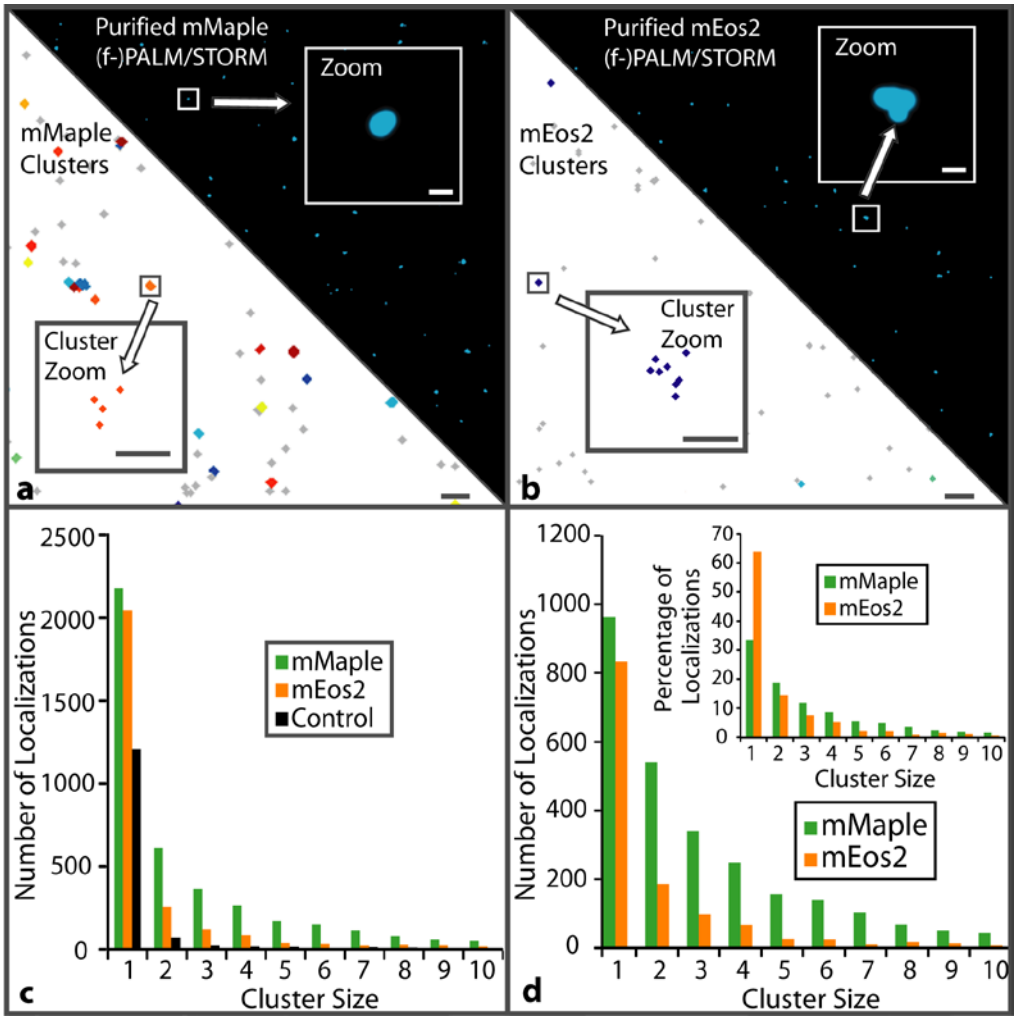

Figure 5-18. (f-)PALM/STORM analysis of purified pcFPs. (**a**,**b**) Composite images of purified (**a**) mMaple and (**b**) mEos2 proteins immobilized on a coverslip. Localizations are represented as normalized 2D Gaussian peaks (right half) and represented as single localizations and clustered markers (< 30 nm interlocalization spacing) (left). Scale bars are 2 μm and 50 nm (zooms). (**c**) Cluster size distribution for purified mMaple and mEos2 as well as a no protein control. (**d**) False-positive corrected cluster size distributions for purified mMaple and mEos2 demonstrate that mMaple is approximately twice as likely to reactivate as mEos2. (**inset**) Percentage of false-positive corrected localizations found to be in clusters for purified pcFPs. 35% of mMaple and 65% of mEos2 do not have a second localization within 30 nm.

5.4 Materials and Methods

General Methods and Materials

Primers were purchased from Integrated DNA Technologies (Coralville, IA) or Elim Biopharmaceuticals Inc. (Hayward, CA). The sequences of all primers used in this work are provided at the end of the Supplementary Methods section. Plasmid and linear DNA purifications were performed using QIAprep spin miniprep or QIA gel extraction kits (Qiagen). All restriction enzymes were purchased from New England Biolabs. PCR amplifications were carried out using the PfuUltraII Fusion HS polymerase (Stragene) of Pfu polymerase (Fermentas). Sequencing reactions were performed using the BigDye Terminator v3.1 Cycle Sequencing Kit (Applied Biosystems) or with custom sequencing primers and analyzed at either the University of Alberta Molecular Biology Service Unit or UC Berkeley DNA Sequencing Facility. Mass spectrometry (MS) was performed by the MS Facility in the Department of Chemistry, University of Alberta.

Engineering of improved mClavGR variants

A two-step PCR procedure was used to introduce the 220-224 HSGLP -> RNSTD modification into mClavGR2. In the first step, the gene encoding mClavGR2 [32] was PCR amplified with the reverse primer1 and forward primer2. The resulting PCR product was used as the template for a second PCR amplification with forward primer2 and reverse primer3, which yielded the full length FP gene. As with all gene libraries for screening and single genes for large scale expression, purification, and *in vitro* characterization, the full length gene was digested by Xho1 and EcoR1 and ligated with T4 ligase (Invitrogen) into similarly digested pBAD/His B vector. To create a gene library with all possible residues at position 173, the template gene was subjected to two separate PCR amplifications: one with forward primer4 and reverse primer3 and one with forward primer2 and reverse primer5. The PCR products were combined and the full length gene assembled by overlap extension [43]. Creation of randomly mutated and gene shuffled libraries was carried out as previous described [32]. Following ligation, electrocompetent *E. coli* strain DH10B (Invitrogen) was transformed and plated on LB/agar plates supplemented with ampicillin (0.1 mg/ml) and L-arabinose (0.02%). For library screening, plates were incubated for 14 h at 37 °C prior to inspection.

The screening setup and general protocol was been previously described [32]. Briefly, Petri dishes harboring colonies of *E. coli* transformed with a gene library were imaged to record their initial green fluorescence intensity. The plate was then subjected to illumination from a dense array of 405 nm LEDs. The red fluorescence

intensity of the same dish was recorded after photoconversion. Digital fluorescence images were then processed to acquire both the green and red fluorescence intensity of each colony. In an effort to more effectively identify variants that exhibited rapid photoconversion, the illumination (i.e., photoconversion) time of the colony libraries was decreased from 20 min to 10 min. Colonies that exhibit both high brightness and an improved ratio of red fluorescence after photoconversion to green fluorescence before photoconversion are considered 'winners' of a given round of screening and served as templates for the following round of library generation.

***In vitro* characterization of mMaple and mClavGR3**

Protein purification was carried out as previously reported [35]. The protein was exchanged into PBS (pH 7.4) buffer unless otherwise indicated. Molar extinction coefficients (ε) of the green states were measured by the alkali denaturation method and then used as reference to measure ε for the red states. To determine the ε of the red states, the pcFPs were photoconverted using 405 nm LED array until the red absorbance peak reached a maximum. Fluorescence quantum yields (Φ) were determined using fluorescein in 10 mM NaOH (Φ = 0.95){Brannon 1978} and Rhodamine 6G in ethanol (Φ = 0.94) as standards. All absorption measurement was acquired on a DU-800 UV-visible spectrophotometer (Beckman). All fluorescence spectra were recorded on a QuantaMaster spectrofluorimeter (Photon Technology International) and have been corrected for the detector response. For determination of the pH dependence, purified protein in PBS was diluted 1:50 into a series of pH-adjusted citrate saline (pH ≤ 8) or sodium phosphate (pH > 8) buffers in a 96-well black clear bottom plate (Corning). Fluorescence was measured using a Safire2 plate reader (Tecan).

To measure the maturation profiles of mMaple, mClavGR variants and mEos2, *E. coli* transformed with pBAD/His B plasmids bearing the encoding cDNA was cultured overnight. The culture was diluted to an OD_{600} of 0.6, purged with argon for 20 min, sealed with a rubber septum, and incubated for another 1 h to allow thorough consumption of the residue oxygen. L-Arabinose (0.025%) was then added via a syringe with needle to induce expression of the FPs. After 4 h of incubation with shaking at 37 °C, the cultures were transferred to an ice bath for 10 min and maintained at 4 °C. Cells were centrifuged at 8000 rpm for 2 min, and cell pellets were lysed using vacuum-degassed B-PER II (Pierce) and incubated at room temperature for 10 min. The lysate was then centrifuged at 12,500 rpm for 5 min, and the supernatant was diluted 10 times into PBS (pH 7.4). Fluorescence maturation was monitored at 37 °C using a Safire2 plate reader (Tecan).

To evaluate the expression level of mMaple, mClavGR variants and mEos2, *E. coli* transformed with pBAD/His B plasmids bearing the encoding cDNA was cultured overnight. The culture was diluted to an OD_{600} of 0.6 in a total volume of 4 mL and L-arabinose (final concentration 0.02%) was added to induce the expression of the FPs. After 2 h growing at 37 °C with shaking, the cells were collected, lysed with 50 μL of B-PER (Pierce), and centrifuged to separate the soluble proteins from insoluble material. An aliquot of the supernatant was taken for later SDS-PAGE analysis. The cell pellet was rinsed once with B-PER and once with 2 M urea. The pellet was then redissolved in 100 μL 8 M urea and centrifuged at 12000 rpm for 10 min. An aliquot of the supernatant was taken for later SDS-PAGE analysis. Both the supernatant from the lysate and the supernatant from the pellet extract were further purified by Ni^{2+}/NTA-conjugated beads and all samples were analyzed by SDS-PAGE. The intensity of the bands was analyzed using ImageQuant RT ECL (General Electric).

Bacterial strains and plasmids for *E. coli* imaging

Strains containing CheW fusions are derivatives of RP437, a chemotactic wild-type *E. coli* K-12 strain. CheW fusions were expressed in a strain lacking the genomic copy of CheW. All other strains are derivatives of MG1655, a wild-type *E. coli* K-12 strain. Strains derived from MG1655 contain the pJat plasmid [44], which contains the L-arabinose transporter gene (*araE*) under a constitutive promoter to increase the homogenous expression from the L-arabinose promoter. pJat is gentamicin resistant. All proteins were expressed from the inducible L-arabinose promoter on the low-copy plasmid pBAD (Invitrogen) containing a pBR322-derived origin, the ampicillin resistance gene (*bla*), and the a*raC* gene for positive regulation of the L-arabinose promoter. pALM1000 contains the EGFP gene only, pALM7000 contains the mEos2 gene only, pALM9000 contains the mClavGR2 gene only, pALM10000 contains the mMaple gene only, and pALM11000 contains the mClavGR3 gene only.

RP437 Δ*cheW* was made by P1 transduction from the Keio collection strains JW1876 (Δ*cheW::kan*). The deletion in this strain was constructed to minimize polar effects on downstream gene expression by retaining the native start codon and the last 18 C-terminal nucleotides [45].

Construction of plasmids for expression of CheW fusion constructs

All fusions to CheW consist of the FP followed by the entire *cheW* gene (residues 1 – 167), and a terminal Glu-Phe encoding an EcoRI site. Plasmid pALM7000 was constructed by PCR amplification of the monomeric *Eos2* gene from

the plasmid pRSETa_mEos2 (Addgene plasmid 20341) using primer6 and primer7, which contain NcoI and BamHI sites, respectively. The PCR product was inserted into plasmid pBAD (Invitrogen) according to the manufacturer's instructions. The N-terminal plasmid leader sequence was removed by digestion with NcoI and religation. pALM9000 was constructed by PCR amplification of the monomeric *ClavGR2* gene from the plasmid pmClavGR2-C1 using primer8 and primer9 containing NcoI and PstI sites, respectively. The PCR product was subcloned into pALM7000 using the NcoI and PstI sites. pALM10000 and pALM11000 was constructed by PCR amplification of the monomeric *Maple* (pALM10000) and *ClavGR3* (pALM11000) genes from the pBAD/HisB plasmid containing either mMaple or mClavGR3 using primer10 and primer11. These PCR products were subcloned into pALM7000 using the NcoI and PstI sites. Plasmid pALM1000 was constructed by PCR amplification of EGFP from the pTrcHis2-EGFP plasmid using primer12 and primer13. This PCR product was subcloned into pALM7000 using the NcoI and PstI sites.

Fusions of pcFPs with CheW were constructed by PCR amplification of *cheW* from strain RP437 using primer14 and primer15, and cloned into the PstI and EcoRI sites of pALM1000, pALM7000, pALM9000, pALM10000, pALM11000, immediately after the FP gene to create pALM1001, pALM7001, pALM9001, pALM10001 and pALM11001 that contain *EGFP-cheW*, *mEos2-cheW*, *mClavGR2-cheW*, *mMaple-cheW* and *mClavGR3-cheW* gene fusions respectively.

Construction of plasmids for expression in mammalian cells

Plasmids for expression of pcFP fusions in mammalian cells were constructed using C1 and N1 (Clontech™-style) cloning vectors. The pcFP cDNA was amplified with a 5′ primer encoding an AgeI site and a 3′ primer encoding either a BspEI (for a C1-type vector) or NotI (for a N1-type vector) site for C-terminal and N-terminal fusions (with regards to the FP), respectively. Purified and digested PCR products were ligated into similarly digested EGFP-C1 and EGFP-N1 cloning vector backbones to provide a set of cloning vectors. To generate α-actinin, paxillin, and histone H2B fusion vectors, the appropriate cloning vector and previously assembled EGFP fusion vectors were digested, either sequentially or doubly, with the appropriate enzymes and ligated together after gel purification as previously described [35].

All plasmid DNA for transfection was prepared using the Plasmid Maxi kit (QIAGEN, Valencia, CA). To ensure proper localization, pcFP fusion proteins were characterized by transfection of HeLa cells (CCL2 line; ATCC, Manassas, VA) using Effectene (QIAGEN) and ~ 1 μg plasmid DNA. Transfected cells were grown on

coverslips in DMEM/F12, fixed after 48 hours, and mounted with Gelvatol. Epifluorescence images were taken with a Nikon 80i microscope using widefield illumination and a FITC filter set. Visual inspection confirmed that the localization of each protein was consistent with the expected pattern.

Determination of photoconversion rate and photoconversion contrast

HeLa S3 cells were cultured in a 50:50 mixture of Ham's F-12 and Dulbecco's modified Eagle's medium (Invitrogen) supplemented with 12.5% fetal bovine serum (FBS). The cells were then seeded onto 35 mm Delta-T imaging dishes for live cell imaging under an atmosphere of 5% CO_2. Cells were transfected in culture medium with Effectene (Qiagen) and 1 μg of purified plasmid DNA encoding the pcFP fused with human histone H2B. At 24 hours post-transfection, samples received fresh media and were imaged live. All photoconversion efficiency measurements were performed on an Olympus FV1000 confocal microscope with an Olympus PLAPO 60× oil-immersion objective (NA = 1.4). FluoView software (Olympus) was used for microscope control and image acquisition, and Simple PCI software (Hammamatsu) was used for image analysis. The 488 nm argon and 543 nm helium-neon laser lines (Melles Griot) were used with a 405/488/543 dichroic mirror to excite the green and red forms of each protein. Emission was collected in two channels spanning 500 – 533 nm (488 nm laser) and 550 – 660 nm (543 nm laser). For photoconversion, a 405 nm diode laser line (Olympus Simultaneous scanner unit) was used with the same dichroic for stimulation. Cells were imaged at a scan speed of 4.0 μs/pixel and were stimulated with the Simultaneous Scanner at a speed of 2.0 μs/pixel. Each experiment was performed with a pinhole size of 600 μm.

A single relatively bright nucleus was selected for imaging and both the red and green fluorescence channels were imaged while the entire nucleus was stimulated using the 405 nm Simultaneous Scanner. The average intensity at each time point for a region-of-interest within the nucleus was determined in software for each of 10 independent experiments and the average value was plotted as a function of time. To assess the rate of photoconversion, the time at which red fluorescence reached half of its maximum value was determined. Photoconversion contrast was calculated as the ratio of red fluorescence intensity (arbitrary units) to green fluorescence intensity (arbitrary units) immediately after red fluorescence had reached a maximum and near the end of the experimental time course.

Determination of photobleaching rates

Laser-scanning confocal and widefield microscopy photobleaching experiments utilized HeLa S3 cells expressing fusions of pcFP fused with human histone H2B, as described above for the photoconversion experiments. Nuclei with similar size and fluorescence intensity were chosen for photobleaching experiments. For laser-scanning confocal photobleaching an Olympus FV1000 was used to first image the cells at a low magnification to ensure cell vitality. The microscope was set to a zoom of 8×, a photomultiplier voltage of 500V, and an offset of 12%, with a scan time of 4 μs/pixel. Cells were photobleached utilizing an Olympus PLAPO 60× oil-immersion objective (NA = 1.4) using either a 488 nm (green state) or a 543 nm (red state) laser line that was maintained at an output power of 120 μW using a FieldMax II-TO (Coherent) power meter. The fluorescence signal was collected in two channels spanning 500 – 522 nm (488 nm laser) and 550 – 660 nm (543 nm laser). A 405 nm diode laser line was used to photoconvert the protein.

For widefield photobleaching experiments, transfected HeLa S3 cells in a Bioptechs Delta-T imaging chamber were imaged on a Nikon TE2000 inverted microscope equipped with a 40× dry objective (Nikon Plan Fluorite NA = 0.85) and an X-Cite exacte light source (Lumen Dynamics). To ensure the same power levels were used for each filter set, a Newport 1918-C optical power meter was used at the objective to measure the illumination intensity. Power was moderated using neutral density filters contained in the lamp. Regions of the dish containing 10 – 20 nuclei were photobleached for 3000 frames at a 100 ms exposure time with no delay. Images were collected using a QImaging Retiga EXi camera (Photometrics). Photoconversion was conducted using an Omega QMax Blue filter set. Photobleaching was conducted using a Chroma FITC-HYQ cube (green species) and a Semrock TRITC-A-000 cube (red species) at a power of 11.4 mW/cm^2. The raw data was collected using NIS-Elements software (Nikon) and analyzed with Simple PCI software (Hamamatsu).

***E. coli* cell culture conditions for imaging**

Strains derived from RP437 were grown overnight in T-broth (1% w/v Difco Bacto-Tryptone (Becton Dickinson and Company), and 0.5% w/v NaCl (Fisher-Scientific) (pH 7.0)) at 30°C with aeration. Day cultures were inoculated to an optical density at 600 nm (OD_{600}) of approximately 0.01 into T-broth with appropriate antibiotics at 30°C with aeration until they reached an OD_{600} 0.1 – 0.3. Protein expression was induced by adding 0.01% or 0.02% L-arabinose for 3 – 8 hrs, as indicated. Strains derived from MG1655 were grown overnight in LB at 30°C with aeration. Day cultures were inoculated by diluting overnight cultures 1:500 into fresh Luria Broth growth media with appropriate antibiotics (Amp and Gent) at 30°C with

aeration until they reached an OD_{600} 0.4 – 0.6. Protein expression was induced by either 0.002% or 0.0002% L-arabinose for 3 hrs. Media and temperature were chosen to obtain the highest expression levels of properly folded proteins [29, 31, 32, 46].

Swarm plate assay

To assess the functionality of chemotaxis fusion proteins, 2 μl of stationary-phase cells were spotted on soft-agar swarm plates and incubated at 30°C for 5 h. Wild-type RP437 *E. coli* cells were compared with a CheW deletion strain and CheW deletion strains with fluorescently tagged CheW fusion proteins (cells used for imaging). All complemented strains contain plasmids derived from pBAD (pBAD TOPO-TA Invitrogen), which confers ampicillin resistance and is L-arabinose inducible. Swarm plates contain 0.3% agar (Becton-Dickinson) in T-broth supplemented with varying concentrations of L-arabinose. Cells were grown in tryptone broth with appropriate antibiotics at 30°C prior to spotting on swarm plates.

Sample preparation and imaging protocol for SIM

Cells were harvested by centrifugation at 2,000 *g* for 15 minutes. The outer membrane of the *E. coli* was fluorescently labeled with 10 ng/μL FM4-64 (Invitrogen) diluted in M9 (1.05% M9 salts (Amresco) supplemented with 2 mM $MgSO_4$, 0.1 mM $CaCl_2$ and 0.4% glycerol) for 5 minutes. Cells were washed twice with M9 media and resuspended in fresh M9 media. 20 uL of 1.5% low-melt agar (Apex) dissolved in M9 media was deposited on a 25 mm × 75 mm single shallow depression slide (Boreal Northwest) flanked by two pieces of double stick tape and allowed to air dry. 0.5 μL of cells labeled with FM4-64 were deposited on the top of the agar and sandwiched between a 22 mm^2 #1.5 microscope coverslip (Fisherbrand).

SIM imaging was performed on the Deltavision|OMX V3.0 (Applied Precision Inc, Issaquah, WA) containing 405 nm, 488nm, 514 nm, 593 nm and 642 nm laser lines{Cogger 2010}. The sample was imaged with a 100× 1.40 NA oil objective with 1.514 or 1.516 index immersion oil. Eukaryotic cells were imaged with 488 nm excitation and *E. coli* cells were imaged with 488 nm and 594 nm excitation. The fluorescence emission was split by channel, filtered and imaged using a dedicated custom monochrome 20 MHz camera with Sony ICX285 ER progressive scan CCD using 5 – 60 ms exposures. Acquisition was controlled by the OMXN controller software (Applied Precision Inc, Issaquah, WA) while reconstructions were made with the OMX specific SoftWoRx v4.5.0 software package (Applied Precision Inc., Issaquah, WA). 3D reconstructions were obtained in 125 nm steps.

Sample preparation and imaging protocol for PALM

Cells were fixed harvested by centrifugation at 2,000 *g* for 15 minutes. Cells were resuspended in 2 – 4% paraformaldehyde (Electron Microscopy Sciences) with 0.1 – 0.2% gluteraldehyde (Electron Microscopy Sciences) in PBS (pH 7.4) for 10 minutes. Cells were washed twice with PBS and resuspended in fresh PBS. #1.5 Lab-TekII 8-well chambers (Nalge Nunc International) were covered with 200 μL 0.1% w/v poly-L-lysine for 15 min then rinsed with water. Cells were added and spun onto coverslips at 2,000 *g* for 10 min. The sample were then rinsed with PBS and left in fresh PBS for imaging.

PALM imaging was performed according to Greenfield *et al.* [9] on an Olympus IX71 inverted microscope equipped with a 100×, 1.40 NA objective (Olympus). 405 nm and 561 nm laser light was delivered to the microscope through free space. 488 nm light was delivered via a mercury lamp with appropriate excitation and emission filters. Single-molecule fluorescence signals generated during acquisition were separated from the activation and excitation light using appropriate filter sets [12, 47] within the microscope and passed to an electron-multiplying charge-coupled device (CCD) camera running at approximately 20 Hz (50 ms exposures). Movie acquisition times were dependent on the regions of highest labeled-protein density. Activation intensity was increased slowly such that a given diffraction-limited spot contained no activated proteins > 90% of the time. This is necessary to ensure that only one protein is activated at a time in a single diffraction-limited spot. Image generation and data analysis were done using custom Matlab scripts (Mathworks), as described by Greenfield et al.[9], and custom IDL software [12].

The localization and image-rendering algorithms used in this work have been previously described [3, 4]. Briefly, images were filtered and proteins were identified as signals that contained counts larger than four standard deviations above background. Proteins that became dark, but reappeared within five frames, were counted as the same protein. Photon distributions were obtained from proteins emitting at least 300 photons. In the case of the *E. coli* strains, only proteins that emitted at least 150 photons were counted, for mammalian cell PALM images, only proteins that emitted 400 photons or more were included. Sample drift was corrected by previously described algorithms [3, 6].

Single protein localizations were grouped into clusters using a tree-clustering algorithm [9]. Proteins spaced less than 30 nm apart from each other are considered to be part of the same cluster, where clusters contain 2 or more proteins. 30 nm interlocalization spacing was chosen because it is twice the mean localization precision for these pcFPs [9, 39].

Sample preparation and imaging protocol for purified protein PALM experiments

mMaple and mEos2 were purified as described above and then biotinylated using EZ-Link Sulfo-NHS-Biotin (Pierce) following the manufacturer's instruction. This biotinylation kit would provide a spacer about 22.4 Å between the pcFP and the biotin module. The spectral profile of absorbance, excitation and emission of the pcFPs were measured and found to remain unchanged. The number of labeled biotins per pcFP molecule was determined to be a distribution that ranged from 7-13, based on MALDI-MS.

Single biotinylated pcFPs were immobilized on an glass coverslip by incubating the slide with 1.0 mg/mL biotinylated bovine serum albumin (b-BSA, Sigma) solution for 30 sec, followed by 0.25 mg/mL streptavidin (Invitrogen) and then biotinylated pcFPs at approximately 0.6 μM in PBS, which were sonicated prior to addition. To correct for drift, 200 nm yellow-green beads (Molecular Probes) diluted in PBS were added to the chamber and immobilized using a buffer containing 10 mM Tris, pH 7.5, 50 mM NaCl and 50 mM $MgCl_2$. The slide was rinsed with PBS prior to the addition of each reagent.

Single pcFPs were imaged in PBS using continuous activation and excitation using 405 nm and 561 lasers for 10,000 frames at constant laser power. To determine the degree of false positive events observed during imaging, a sample chamber containing only PBS and fiduciary markers was imaged. PALM images were reconstructed and drift corrected as described above.

To determine the degree of reversible photoswitching, closely spaced molecules were grouped, resulting in a cluster size distribution for each pcFP as well as the negative control. The distribution obtained from the negative control was subtracted from the resulting pcFP distributions to remove the population of false positives resulting from events unrelated to pcFP fluorescence.

List of primers

primer1: 5′-CAGCTCGTCCATGCCGTCGGTGGAGTTGCGGGCCACGGCGTG-3′

primer2: 5′-GCAGGTGAGTAACTCGAGCATGGTGAGCAAGG-3′

primer3: 5′-GCCGAATTCTTACTTGTACAGCTCGTCCAT-3′

primer4: 5′-NNKCGCTGCGACTTCCGCACCTA-3′

primer5: 5′-AAGTCGCAGCGMNNGTGGCCGCCGCC-3′

primer6: 5′-GGATCCATGGGGGCGATTAAGCCAGAC-3′

primer7: 5′-CAAGCTTCTTAGGATCCTCGTCTGGCATTGTCAGGC-3′

primer8: 5′-CCGGTCGCCACCATGGTGAGCAAGG-3′

primer9: 5′-GAGATCTGAGCTGCAGCTTGTACAGCTCG3′

primer10: 5′-GCTCGACCATGGTGAGCAAGG-3′

primer11: 5′-CCAAGCTTCGAACTGCAGCTTGTACAGCTC-3′

primer12: 5′-GGAGGAATAAACCATGGTGAGCAAG-3′

primer13: 5′-CGTAAGCTTCCTGCAGCTTGTACAGCTCG-3′

primer14: 5′-AAAGGTCTGCAGATGACCGGTATGACGAATGTAAC-3′

primer15: 5′-TCGGGAGAATTCCGCCACTTCTGACG-3′

5.5 References

1. Hell SW: Far-Field Optical Nanoscopy. *Science* 2007, 316:1153-1158.

2. Schermelleh L, Heintzmann R, Leonhardt H: A guide to super-resolution fluorescence microscopy. 2010, 190:165-175.

3. Betzig E, Patterson GH, Sougrat R, Lindwasser OW, Olenych S, Bonifacino JS, Davidson MW, Lippincott-Schwartz J, Hess HF: Imaging Intracellular Fluorescent Proteins at Nanometer Resolution. *Science* 2006, 313:1642-1645.

4. Rust MJ, Bates M, Zhuang X: Sub-diffraction-limit imaging by stochastic optical reconstruction microscopy (STORM). *Nat Meth* 2006, 3:793-796.

5. Hess Girirajan T, Mason M S: Ultra-High Resoluion Imaging by Fluorescence Photoactivation Localization Microscopy. *Biophysical Journal* 2006, 91:4258-4272.

6. Huang B, Jones SA, Brandenburg B, Zhuang X: Whole-cell 3D STORM reveals interactions between cellular structures with nanometer-scale resolution. *Nat Meth* 2008, 5:1047-1052.

7. Shtengel G, Galbraith JA, Galbraith CG, Lippincott-Schwartz J, Gillette JM, Manley S, Sougrat R, Waterman CM, Kanchanawong P, Davidson MW, Fetter RD, Hess HF: Interferometric fluorescent super-resolution microscopy resolves 3D cellular ultrastructure. *Proceedings of the National Academy of Sciences* 2009, 106:3125-3130.

8. Vaziri A, Tang J, Shroff H, Shank CV: Multilayer three-dimensional super resolution imaging of thick biological samples. *Proceedings of the National Academy of Sciences* 2008, 105:20221-20226.

9. Greenfield D, McEvoy AL, Shroff H, Crooks GE, Wingreen NS, Betzig E, Liphardt J: Self-organization of the Escherichia coli chemotaxis network imaged with super-resolution light microscopy. *PLoS biology* 2009, 7:e1000137.

10. York AG, Ghitani A, Vaziri A, Davidson MW, Shroff H: Confined activation and subdiffractive localization enables whole-cell PALM with genetically expressed probes. *Nat Meth* , 8:327-333.

11. Huang B, Wang W, Bates M, Zhuang X: Three-Dimensional Super-Resolution Imaging by Stochastic Optical Reconstruction Microscopy. *Science* 2008, 319:810-813.

12. Bates M, Huang B, Dempsey GT, Zhuang X: Multicolor Super-Resolution Imaging with Photo-Switchable Fluorescent Probes. *Science* 2007, 317:1749-1753.

13. Jones SA, Shim S-H, He J, Zhuang X: Fast, three-dimensional super-resolution imaging of live cells. *Nat Meth* , 8:499-505.

14. Shroff H, Galbraith CG, Galbraith JA, Betzig E: Live-cell photoactivated localization microscopy of nanoscale adhesion dynamics. *Nat Meth* 2008, 5:417-423.

15. Lefman J, Scott K, Stranick S: Live, video-rate super-resolution microscopy using structured illumination and rapid GPU-based parallel processing. *Microscopy and microanalysis : the official journal of Microscopy Society of America, Microbeam Analysis Society, Microscopical Society of Canada* 2011, 17:191-6.

16. Kner P, Chhun BB, Griffis ER, Winoto L, Gustafsson MGL: Super-resolution video microscopy of live cells by structured illumination. *Nat Meth* 2009, 6:339-342.

17. Gustafsson MG: Surpassing the lateral resolution limit by a factor of two using structured illumination microscopy. *Journal of microscopy* 2000, 198:82-7.

18. Gustafsson MGL, Shao L, Carlton PM, Wang CJR, Golubovskaya IN, Cande WZ, Agard DA, Sedat JW: Three-Dimensional Resolution Doubling in Wide-Field Fluorescence Microscopy by Structured Illumination. *Biophysical Journal* 2008, 94:4957-4970.

19. Hein B, Willig KI, Hell SW: Stimulated emission depletion (STED) nanoscopy of a fluorescent protein-labeled organelle inside a living cell. *Proceedings of the National Academy of Sciences* 2008, 105:14271-14276.

20. Schmidt R, Wurm CA, Jakobs S, Engelhardt J, Egner A, Hell SW: Spherical nanosized focal spot unravels the interior of cells. *Nat Meth* 2008, 5:539-544.

21. Willig KI, Kellner RR, Medda R, Hein B, Jakobs S, Hell SW: Nanoscale resolution in GFP-based microscopy. *Nature Methods* 2006, 3:721-723.

22. Rankin BR, Moneron G, Wurm C a, Nelson JC, Walter A, Schwarzer D, Schroeder J, Colón-Ramos D a, Hell SW: Nanoscopy in a living multicellular organism expressing GFP. *Biophysical journal* 2011, 100:L63-5.

23. Donnert G, Keller J, Wurm CA, Rizzoli SO, Westphal V, Schonle A, Jahn R, Jakobs S, Eggeling C, Hell S: Two-Color Far-Field Fluorescence Nanoscopy. *Biophysical Journal* 2007, 92:L67-L69.

24. Donnert G, Keller J, Medda R, Andrei MA, Rizzoli SO, Lu R, Jahn R, Eggeling C, Hell SW: Macromolecular-scale resolution in biological. *Most* 2006.

25. Patterson GH, Lippincott-Schwartz J: A photoactivatable GFP for selective photolabeling of proteins and cells. *Science (New York, N.Y.)* 2002, 297:1873-7.

26. Subach FV, Patterson GH, Manley S, Gillette JM, Lippincott-schwartz J, Verkhusha VV: Photoactivatable mCherry for high-resolution two-color fluorescence microscopy. *Nature Methods* 2009, 6:153-160.

27. Ando R, Mizuno H, Miyawaki A: Regulated fast nucleocytoplasmic shuttling observed by reversible protein highlighting. *Science (New York, N.Y.)* 2004, 306:1370-3.

28. Ando R, Hama H, Yamamoto-Hino M, Mizuno H, Miyawaki A: An optical marker based on the UV-induced green-to-red photoconversion of a fluorescent protein. *Proceedings of the National Academy of Sciences of the United States of America* 2002, 99:12651-6.

29. Wiedenmann Ivanchenko, S., Oswald, F., Schmitt, F., Rocker, C., Salih, A., Spindler, K., Niehaus, G. U. J: EosFP, a fluorescent marker protein with UV-inducible green-to-red fluorescence conversion. *Proceeding of the National Academy of Science* 2004, 101:15905-15910.

30. Habuchi S, Tsutsui H, Kochaniak AB, Miyawaki A, van Oijen AM: mKikGR, a monomeric photoswitchable fluorescent protein. *PloS one* 2008, 3:e3944.

31. Mckinney SA, Murphy CS, Hazelwood KL, Davidson MW, Looger LL: A bright and photostable photoconvertible fluorescent protein. *Nature Methods* 2009, 6:131-133.

32. Hoi H, Shaner NC, Davidson MW, Cairo CW, Wang J, Campbell RE: A monomeric photoconvertible fluorescent protein for imaging of dynamic protein localization. *Journal of molecular biology* 2010, 401:776-91.

33. Heilemann M, van de Linde S, Mukherjee A, Sauer M: Super-resolution imaging with small organic fluorophores. *Angewandte Chemie (International ed. in English)* 2009, 48:6903-8.

34. Lee H-lu D, Lord SJ, Iwanaga S, Zhan K, Xie H, Williams JC, Wang H, Bowman GR, Goley ED, Shapiro L, Twieg RJ, Rao J, Moerner WE: Superresolution imaging of targeted proteins in fixed and living cells using photoactivatable organic fluorophores. *Journal of the American Chemical Society* 2010, 132:15099-101.

35. Ai H-wang, Henderson JN, Remington SJ, Campbell RE: Directed evolution of a monomeric, bright and photostable version of Clavularia cyan fluorescent protein: structural characterization and applications in fluorescence imaging. *The Biochemical journal* 2006, 400:531-40.

36. Henderson JN, Remington SJ: Crystal structures and mutational analysis of amFP486, a cyan fluorescent protein from Anemonia majano. *Proceedings of the National Academy of Sciences of the United States of America* 2005, 102:12712-7.

37. Shaner NC, Steinbach PA, Tsien RY: A guide to choosing fluorescent proteins. *Nature Methods* 2005, 2.

38. Bates M, Jones SA, Zhuang X: *in Imaging : a laboratory manual (eds Yuste, R.)*. Cold Spring Harbor, N.Y.: Cold Spring Harbor Laboratory Press; 2011:547-576.

39. Thompson Larson, D. R., Webb, W. RE: Precise nanometer localization analysis for individual fluorescent probes. *Biophysical Journal* 2002, 82:2775-2783.

40. Li Hazelbauer, G. M: Cellular stoichiometry of the components of the chemotaxis signaling complex. *Journal of Bacteriology* 2004, 186:3687-3694.

41. Annibale, Paolo, Scarselli, M., Kodiyan, A., Radenovic A: Photoactivatable Fluorescen Protein mEos2 Displays Repeated Photoactivation after a Long-Lived Dark State in Red Photoconverted Form. *Journal of Physical Chemistry Letters* 2010, 1:1506-1510.

42. Annibale P, Vanni S, Scarselli M, Rothlisberger U, Radenovic A: Identification of clustering artifacts in photoactivated localization microscopy. *Nature Methods* 2011, 8:7-8.

43. Zha HZ& W: In vitro "sexual" evolution through the PCR-based staggered extension process (StEP). *Nature Protocols* 2006, 1:1865 - 1871.

44. Khlebnikov a, Datsenko K a, Skaug T, Wanner BL, Keasling JD: Homogeneous expression of the P(BAD) promoter in Escherichia coli by constitutive expression of the low-affinity high-capacity AraE transporter. *Microbiology (Reading, England)* 2001, 147:3241-7.

45. Baba T, Ara T, Hasegawa M, Takai Y, Okumura Y, Baba M, Datsenko K a, Tomita M, Wanner BL, Mori H: Construction of Escherichia coli K-12 in-frame, single-gene knockout mutants: the Keio collection. *Molecular systems biology* 2006, 2:2006.0008.

46. Iafolla M a J, Mazumder M, Sardana V, Velauthapillai T, Pannu K, McMillen DR: Dark proteins: effect of inclusion body formation on quantification of protein expression. *Proteins* 2008, 72:1233-42.

47. Shroff H, Galbraith CG, Galbraith JA, White H, Gillette J, Olenych S, Davidson MW, Betzig E: Dual-color superresolution imaging of genetically expressed probes within individual adhesion complexes. *Proceedings of the National Academy of Sciences* 2007, 104:20308-20313.

Chapter 6

Conclusion and Perspectives

6.1 Conclusion and Perspectives

Cellular spatial organization is important for proper protein function. Mislocalization of cellular components can lead to disruptions in processes such as cell growth, signaling, transport, and motility. Aberrant spatial organization has been implicated in pathologies such as cancer [1]. Therefore, cells must develop mechanisms that robustly position their constituents as well as maintain this arrangement as cells exchange and renew their components.

To examine cellular spatial organization, biologists often use a variety of microscopy techniques to simply look at cells. Electron microscopy (EM) allows for nanometer resolution of cellular organization. However, EM requires sample fixation and robust protein labeling strategies have yet to be developed [2]. To examine dynamic processes in living cells, light microscopy, is often used. By introducing genetically encoded fluorescently tagged proteins into cells, it is possible to observe the movements of proteins as they perform functions [3]. A significant disadvantage of light microscopy is its spatial resolution (limited by diffraction to ~250 nm laterally, and ~500 nm axially). Therefore, it can be difficult to directly observe dynamic processes involving closely spaced proteins.

Until the last couple of decades, it was thought that the resolution limit diffraction imposes on light microscopy was insurmountable. However, recent developments in microscopy have led to a number of clever strategies capable of combining the powerful labeling strategies employed by fluorescence imaging with unprecedented spatial resolution. These 'super-resolution' imaging tools are capable of surpassing the diffraction limit of light microscopy by as much as ten times, producing images with nanometer scale resolution (reviewed in [4–8]).

All of these super-resolution techniques have something in common; they all require the spatial confinement of excited fluorophores. This can be done either by stochastically activating photoswitchable fluorophores ((f-)PALM/STORM) [9–11], or by applying a spatial light patterning (SIM/STED) [12, 13] to the sample. This concept has been generally referred to as reversible saturable (or switchable) optical fluorescence transitions between two states (RESOLFT) [4], and has recently been implemented [14].

Traditional super-resolution imaging techniques often require high laser intensities to image biological samples. In the case of PALM/STORM based methods, high intensities are required to bleach fluorophores quickly thereby increases imaging speeds [7, 15]. In the case of STED, increasing the intensity of the STED beam decreases the excitation volume, increasing the spatial resolution of the resulting images. Though all of these methods have demonstrated live-cell imaging

[16–19], the required light intensity and imaging speed in not always ideal for capturing the dynamics of biological systems.

As the field of super-resolution imaging matures, future developments are likely to lead to methods with increased imaging speeds and as well as methods that expose samples to lower light intensities. The recent implementation of RESOLFT [14], is a movement in this direction. RESOLFT combines STED-based imaging with photoswitchable fluorophores. Rather than rely on high laser intensities to spatially restrict the excited fluorophores, RESOLFT utilizes the inherent photophysics of photoswitchable fluorophores, which can be switched to their 'off' state with much lower light intensities than before.

To facilitate the implementation of RESOLFT a new fluorescent protein was developed with switching properties compatible with this technique [14]. In general, super-resolution imaging methods are currently 'probe-limited'. Unlike conventional fluorescent proteins (e.g. GFP, YFP), which have had nearly twenty years of evolution to become very powerful tools for fluorescence microscopy, photoswitchable fluorescent proteins are constantly being developed and improved [20, 21]. Though many new photoactivatable fluorescent proteins have been developed [22–27] (reviewed in [21]), there are currently few spectrally distinct photoswitchable fluorescent proteins, making dual-labeling difficult. Additionally, many photoswitchable fluorescent proteins have poor contrast between their 'on' and 'off' states making it difficult to localize individual molecules. These proteins are also often not very photostable, making it difficult to use these proteins in combination with other imaging modalities.

In Chapter 6, we describe the development of a new photoconvertible fluorescent protein, mMaple, that has a photostable green state useful for SIM imaging, yet is still capable of photoconversion with photophysics appropriate for high quality (f-)PALM/STORM imaging. With the development of new fluorophores, like mMaple, as well as new powerful labeling methods, we may see increased adoption of super-resolution techniques. These new tools may also facilitate the development of new imaging techniques, designed for fast live-cell imaging.

In this dissertation, we describe the application of super-resolution imaging techniques to two spatially organized systems in *E. coli*. In Chapters 2 and 3 of this dissertation, we examined the chemotaxis network in *E. coli* using (f-)PALM/STORM imaging. Bacteria, utilize chemotaxis receptors to locate favorable environments. Receptors cluster and localize to large sensory complexes found at the cell poles and future division sites [28–31]. In addition to observation of large polar clusters, (f-)PALM/STORM images of *E. coli* chemotaxis receptors revealed small receptor clusters spread throughout the bacterium. We showed that this observed spatial

pattern can be modeled with simple stochastic model involving only receptor-receptor interactions within a growing population of bacteria.

Small chemotaxis clusters spread throughout the bacteria were first observed using immunogold EM imaging [31]. However, it was the high labeling density allowed by (f-)PALM/STORM imaging, that provided more conclusive evidence that small clusters exist. Our (f-)PALM/STORM images are reminiscent of the model presented by Berg and Percell [32], which based solely on physical considerations of optimal receptor positioning, suggested that receptors should be evenly distributed throughout the cell. Additionally, *in vitro* data suggest that different densities of receptors have difference in kinase and methylation rates [33]. Currently, it is unknown whether small clusters enhance chemotaxis signaling or are simply an artifact of large cluster assembly. Future work will provide insights into the biological significance of small chemotaxis clusters.

The spatial arrangement of chemotaxis receptors can be explained by stochastic self-assembly. We show that this model can create and maintain dynamic patterns in biological membranes, without direct cytoskeletal involvement or active transport. Recent *in vitro* evidence has demonstrated that purified membrane-associated proteins can spontaneously self-assemble into complex, dynamic structures [34, 35]. Perhaps stochastic self-assembly is the simplest way for proteins to assemble into complex patterns within membranes without additional protein involvement. It will be interesting to see if other systems, including eukaryotic systems employ self-assembly mechanisms to position proteins.

Chapter 4 examines the *in vivo* structure of the *E.coli* Z-ring using multiple imaging modalities. We also monitor how this structure changes during cell division. Like, chemotaxis receptor clustering, the Z-ring seems to be stochastically assembled. This leads to Z-rings with non-uniform distributions of FtsZ around the circumference at mid-cell. Our super-resolution images are consistent with recent cryo-EM tomography images produced by Li *et al.* [36], which demonstrated that the Z-ring is composed of a series of short protofilaments, which may or may not interact.

As cell division proceeds, Z-ring intensity stays mostly constant within the ring, until it completely disassembles. Previous reports suggest that this leads to an increase in lateral interactions between FtsZ subunits, which drives mid-cell constriction [37, 38]. However, our data suggest that increases in FtsZ density during division can be attributed to a global regulator of FtsZ position, known as the Min system (reviewed by [39, 40]). The Min system is a negative regulator of FtsZ position, which through pole-to-pole oscillations, leads to increased FtsZ concentration at mid-cell.

Without the Min system, FtsZ concentration within the Z-ring more gradually decreases as the cell divides. Our results are consistent with an existing model for Z-ring force generation which attributes constriction to protofilament bending after GTP hydrolysis [41]. FtsZ-GTP has been shown to prefer a straight conformation, while FtsZ-GDP prefers a curved configuration [42]. FtsZ-GTP anchored to the membrane could hydrolyze GTP causing a conformational change within the protofilament which bends the membrane. GTP hydrolysis enhances protofilament disassembly, suggesting that as FtsZ creates a force on the membrane, it may lead to fragmentation of the Z-ring [43]. Removal of the Min system decreases local FtsZ concentration, increasing the probability that FtsZ will not return to the ring as subunits exchange. Though cells lacking Min have increased fluctuations in Z-ring intensity over time, the length of cytokinesis is similar to wildtype cells. This suggests that cell division is robust to large fluctuations in FtsZ concentration and Z-ring spatial organization.

Both of these spatially organized systems are examples of an emerging theme in biology, which suggests that instead of being static structures, protein complexes consist of subunits that are constantly interacting and exchanging, thus altering their large-scale spatial organization. To allow for robust outcomes in this ever-changing environment, cellular functions must have evolved to tolerate these fluctuations in protein configurations, or concentration. In the case of chemotaxis receptors, our model explains how a population of cells could maintain a normal cluster spatial pattern even if a parent cell is produced without chemotaxis clusters. In the case of removal of the Min system, large fluctuations in Z-ring intensity still produce viable offspring, on similar timescales as wildtype cells. These mechanisms lead to cell division, and proper signaling, even if the spatial patterns and cellular structures are not always identical.

Until recently, it was thought that bacteria are 'bags of enzymes' that lack internal organized structure. In the last ten years, we have started to appreciate that bacteria are highly spatially organized and this arrangement is important for cellular function. It is interesting to note that bacteria have proven to be useful model systems for studying a number of biological processes. Much of what we learned about DNA translation, transcription and replication was first discovered in bacterial cells. With the development of new imaging tools, such as super-resolution microscopy, it is now possible to investigate the fine structure within small cells that was previously obscured by diffraction. Perhaps, these novel techniques will allow us to start utilizing bacteria as a model system for spatial organization. Only time will tell whether models describing the spatial organization in bacterial cells, translate to their eukaryotic counterparts.

6.2 References

1. Davis JR, Kakar M, Lim CS: Expert Review Controlling Protein Compartmentalization to Overcome Disease. 2007, 24.

2. Kuo J: *Electron Microscopy: Methods and Protocols*. 2nd edition. Humana Press Inc.; 2007.

3. Murphy D: *Fundamentals of Light Microscopy and Electronic Imaging*. John Wiley & Sons, Inc.; 2001.

4. Hell SW: Microscopy and its focal switch. *Online* 2008:1-9.

5. Schermelleh L, Heintzmann R, Leonhardt H: A guide to super-resolution fluorescence microscopy. 2010, 190:165-175.

6. McEvoy AL, Greenfield D, Bates M, Liphardt J: Q&A: Single-molecule localization microscopy for biological imaging. *BMC biology* 2010, 8:106.

7. Dempsey GT, Wang W, Zhuang X: Handbook of Single-Molecule Biophysics. 2009:95-127.

8. Bates M, Jones SA, Zhuang X: *in Imaging : a laboratory manual (eds Yuste, R.)*. Cold Spring Harbor, N.Y.: Cold Spring Harbor Laboratory Press; 2011:547-576.

9. Betzig E, Patterson GH, Sougrat R, Lindwasser OW, Olenych S, Bonifacino JS, Davidson MW, Lippincott-Schwartz J, Hess HF: Imaging Intracellular Fluorescent Proteins at Nanometer Resolution. *Science* 2006, 313:1642-1645.

10. Rust MJ, Bates M, Zhuang X: Sub-diffraction-limit imaging by stochastic optical reconstruction microscopy (STORM). *Nat Meth* 2006, 3:793-796.

11. Hess ST, Girirajan TPK, Mason MD: Ultra-High Resolution Imaging by Fluorescence Photoactivation Localization Microscopy. 2006, 91:4258-4272.

12. Klar TA, Hell SW: Subdiffraction resolution in far-field fluorescence microscopy. *Opt. Lett.* 1999, 24:954-956.

13. Gustafsson MGL: Extended resolution fluorescence microscopy. *Current Opinion in Structural Biology* 1999, 9:627-628.

14. Grotjohann T, Testa I, Leutenegger M, Bock H, Urban NT, Lavoie-Cardinal F, Willig KI, Eggeling C, Jakobs S, Hell SW: Diffraction-unlimited all-optical imaging and writing with a photochromic GFP. *Nature* 2011, 478:204-8.

15. Shroff Galbriath, C., Galbraith, J., White, H., Gillette, J., Olenych, S., Davidson, M., Betzig, E. H: Dual-color supperresolution imaging of genetically expressed probes within individual adhesion complexes. *Proceeding of the National Academy of Science* 2007, 104:20308-20313.

16. Lefman J, Scott K, Stranick S: Live, video-rate super-resolution microscopy using structured illumination and rapid GPU-based parallel processing. *Microscopy and microanalysis : the official journal of Microscopy Society of America, Microbeam Analysis Society, Microscopical Society of Canada* 2011, 17:191-6.

17. Nagerl UV, Willig KI, Hein B, Hell SW, Bonhoeffer T: Live-cell imaging of dendritic spines by STED microscopy. *Proceedings of the National Academy of Sciences* 2008, 105:18982-18987.

18. Jones SA, Shim S-H, He J, Zhuang X: Fast, three-dimensional super-resolution imaging of live cells. *Nat Meth* , 8:499-505.

19. Shroff H, Galbraith CG, Galbraith JA, Betzig E: Live-cell photoactivated localization microscopy of nanoscale adhesion dynamics. *Nat Meth* 2008, 5:417-423.

20. Patterson G, Davidson M, Manley S, Lippincott-Schwartz J: Superresolution imaging using single-molecule localization. *Annual review of physical chemistry* 2010, 61:345-67.

21. Lippincott-Schwartz J, Patterson GH: Photoactivatable fluorescent proteins for diffraction-limited and super-resolution imaging. 2009, 19:555-565.

22. Wiedenmann Ivanchenko, S., Oswald, F., Schmitt, F., Rocker, C., Salih, A., Spindler, K., Niehaus, G. U. J: EosFP, a fluorescent marker protein with UV-inducible green-to-red fluorescence conversion. *Proceeding of the National Academy of Science* 2004, 101:15905-15910.

23. Mckinney SA, Murphy CS, Hazelwood KL, Davidson MW, Looger LL: A bright and photostable photoconvertible fluorescent protein. *Nature Methods* 2009, 6:131-133.

24. Hoi H, Shaner NC, Davidson MW, Cairo CW, Wang J, Campbell RE: A monomeric photoconvertible fluorescent protein for imaging of dynamic protein localization. *Journal of molecular biology* 2010, 401:776-91.

25. Habuchi S, Tsutsui H, Kochaniak AB, Miyawaki A, van Oijen AM: mKikGR, a monomeric photoswitchable fluorescent protein. *PloS one* 2008, 3:e3944.

26. Ando R, Hama H, Yamamoto-Hino M, Mizuno H, Miyawaki A: An optical marker based on the UV-induced green-to-red photoconversion of a fluorescent protein. *Proceedings of the National Academy of Sciences of the United States of America* 2002, 99:12651-6.

27. Ando R, Mizuno H, Miyawaki A: Regulated fast nucleocytoplasmic shuttling observed by reversible protein highlighting. *Science (New York, N.Y.)* 2004, 306:1370-3.

28. Kentner Sourjik, V. D: Spatial organization of the bacterial chemotaxis system. *Current Opinion in Microbiology* 2006, 9:619-624.

29. Sourjik, V, Berg H: Localization of components of the chemotaxis machinery of E. coli using fluorescent protein fusions. *Molecular Microbiology* 2000, 37:740-751.

30. Adler J: Chemotaxis in bacteria. *Annual Reviews of Biochemistry* 1975, 44:341-356.

31. Maddock Shapiro, L. J: Polar localization of the chemoreceptor complex in the E. coli cell. *Science* 1993, 259:1717-1723.

32. Berg Purcell, E. H: Physics of chemoreception. *Biophysical Journal* 1977, 20:193-219.

33. Besschetnova, Tatiana Y. Montefusco, David J. Asinas AE, Shrout AL, Antommattei FM, Weis RM: Receptor density balances signal stimulation and attenuation in membrane-assembled complexes. *PNAS* 2008, 105:12289-12294.

34. Osawa M, Anderson DE, Erickson HP: Reconstitution of Contractile FtsZ Rings in Liposomes. *Science* 2008, 320:792-794.

35. Loose M, Fischer-Friedrich E, Ries J, Kruse K, Schwille P: Spatial regulators for bacterial cell division self-organize into surface waves in vitro. *Science (New York, N.Y.)* 2008, 320:789-92.

36. Li Z, Trimble MJ, Brun YV, Jensen GJ: The structure of FtsZ filaments in vivo suggests a force-generating role in cell division. 2007, 26:4694-4708.

37. Horger I, Velasco E, Rivas G, Velez M, Tarazona P: FtsZ Bacterial Cytoskeletal Polymers on Curved Surfaces: The Importance of Lateral Interactions. *Biophysical Journal* 2008, 94:L81-L83.

38. Lan G, Daniels BR, Dobrowsky TM, Wirtz D, Sun SX: Condensation of FtsZ filaments can drive bacterial cell division. 2009, 106:121-126.

39. Loose M, Kruse K, Schwille P: Protein Self-Organization: Lessons from the Min System. *Annual Review of Biophysics* 2011, 40:315-336.

40. Lutkenhaus J: Assembly Dynamics of the Bacterial MinCDE System and Spatial Regulation of the Z Ring. *Annual Review of Biochemistry* 2007, 76:539-562.

41. Erickson HP: Modeling the physics of FtsZ assembly and force generation. *Proceedings of the National Academy of Sciences* 2009, 106:9238-9243.

42. Lu C, Reedy M, Erickson HP: Straight and Curved Conformations of FtsZ Are Regulated by GTP Hydrolysis. *Journal of Bacteriology* 2000, 182:164-170.

43. Erickson HP, Anderson DE, Osawa M: FtsZ in Bacterial Cytokinesis: Cytoskeleton and Force Generator All in One. 2010, 74:504-528.

Appendix I

Requirements for Functional Fusion Proteins

The addition of a fluorescent protein tag may affect the functionality of the original protein. This is especially true when the target protein forms many functional contacts with other proteins, such as the dense arrangement of chemotaxis receptors. Therefore it is important to measure functionality for each fusion protein. For example, we observe that Tar-tdEos is non-functional as measured by chemotaxis swarm plates, yet Tar-mEos is partially functional. In this case, tdEos may be too bulky to allow functional interactions between chemotaxis receptors. In general, tags must not sterically interfere with specific surfaces of the protein, including binding sites. The tag must not aggregate or form higher ordered structures such as dimers which may affect the function or location of the protein. Tags must fold properly and should not affect the folding or stability of the protein. Finally, tags must not target the protein for degradation or modification. Predicting whether a particular fusion protein will be functional is not yet possible, therefore it is necessary to test combinations of different photoactivatable proteins fused to either the N- or C-termini of proteins, with or without a linker.

Appendix II

Localization Precision and Nyquist Resolution for Eos Fusions

When the background noise is negligible compared to the signal, the error in the fitted position for a single protein is $\sigma_{(x,y)} = s/\sqrt{N}$, where s is the standard deviation of a Gaussian approximating the true point-spread function, and N is the total number of detected photons. Since N varies for different proteins (Figure A-1B,D), the localization error will also vary. We display PALM images with all proteins that have been localized to 40 nm or less, based on our signal-to-background analysis (Figure A-2). With this threshold, the mean localization error is 15 nm with 90% of Tar proteins localized between 4 and 31 nm and 90% of CheW proteins localized between 3 and 34 nm (Figure A-1A,C).

It is important to distinguish the localization precision of single proteins from the resolution of an image. Localization precision refers to how well the locations of individual proteins are known, whereas resolution is the ability to distinguish multiple proteins from each other. The Nyquist criterion offers a rigorous definition of resolution and specifies that, for any signal, the sampling interval must be smaller than half the desired resolution [1]. For a 2D PALM image, the Nyquist-defined spatial resolution is therefore related to the density of proteins: $\rho \geq (2/T)^2$, where T is the resolution (in nm) and ρ is the density of proteins localized to T or better (in nm^{-2}). The Nyquist resolution is highest for the densest regions of an image, which in our case, are the large polar clusters. These large clusters (> 100 fluorescent fusion proteins) each have a Nyquist resolution that varies from cluster to cluster depending on the density of labeled proteins and how well they are localized. These resolutions vary from 10 to 40 nm, with a mean resolution of 30 nm for Tar clusters and 24 nm for CheW clusters. For all large clusters, the mean Nyquist resolution is 27 nm with a standard deviation of 8 nm.

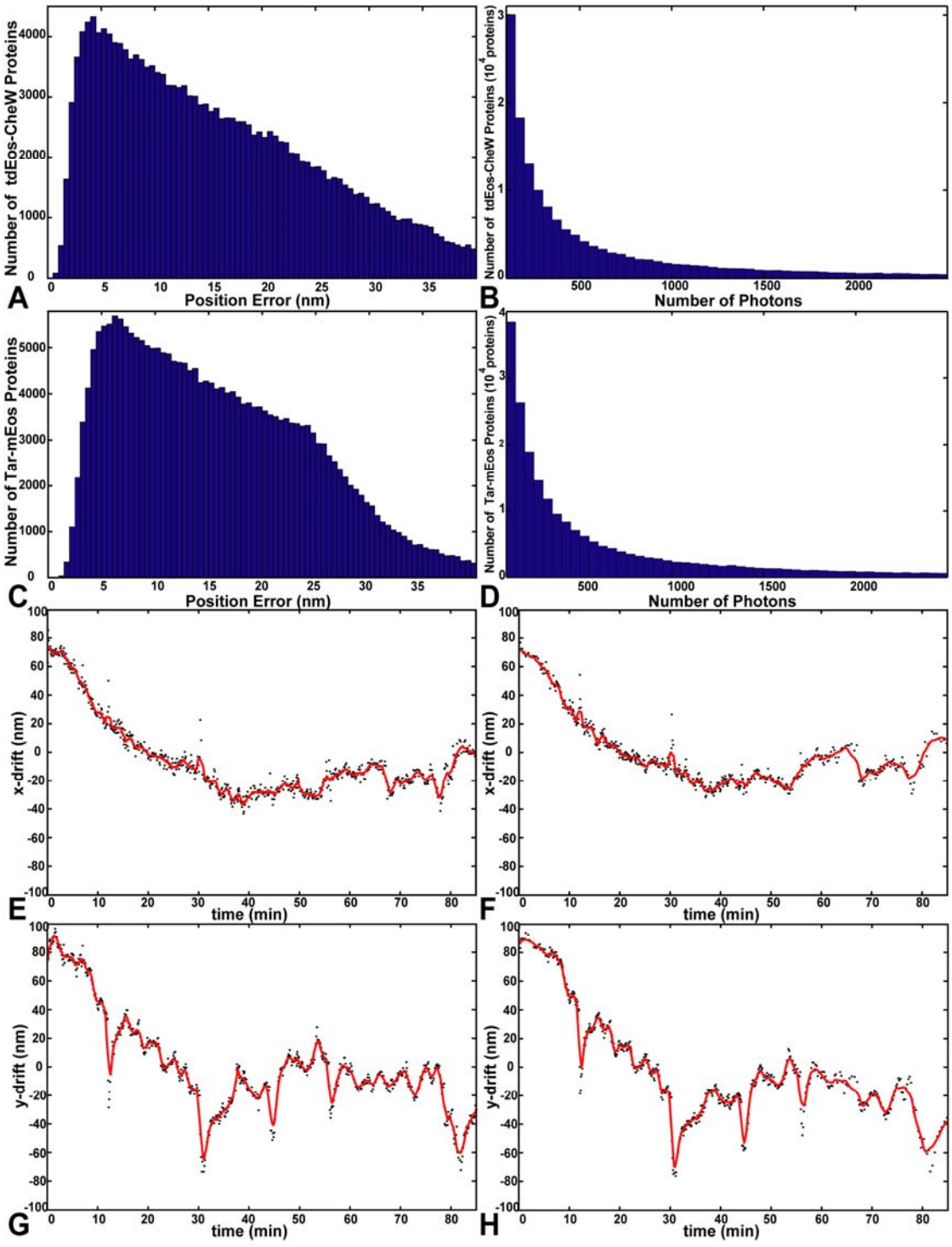
A
Number of tdEos-CheW Proteins
Position Error (nm)
B
Number of tdEos-CheW Proteins (10^4 proteins)
Number of Photons
C
Number of Tar-mEos Proteins
Position Error (nm)
D
Number of Tar-mEos Proteins (10^4 proteins)
Number of Photons
E
x-drift (nm)
time (min)
F
x-drift (nm)
time (min)
G
y-drift (nm)
time (min)
H
y-drift (nm)
time (min)

Figure A-1. Localization precision for fusion proteins and sample drift. (A) x and y positions of 225,016 CheW proteins from 130 cells were determined with an average Gaussian weighted error of 15 nm ± 9 nm. 90% of tdEos-CheW proteins positions were localized between 3-34 nm. **(B)** The number photons emitted from each tdEos-CheW protein. The mean number of photons emitted is 1465. **(C)** x and y position of 313,937 Tar proteins from 84 cells were determined with an average Gaussian weighted error of 15 nm. 90% of Tar-mEos proteins positions were localized between 4-31 nm. **(D)** The number of photons emitted from each Tar-mEos protein. The mean number of photons emitted is 947. **(E-H)** Example of sample drift over 85 minutes as measured simultaneously by two different 40 nm diameter Au nanoparticles. Each data point (black dot) represents a localized position after collection of 40,000 signal photons. Red line is the smoothed drift using a window of 10 nanoparticle positions. Using fiduciary markers we can correct for drift in protein location to a few nanometers (root-mean square error = 3.1 nm in x, 5.3 nm in y).

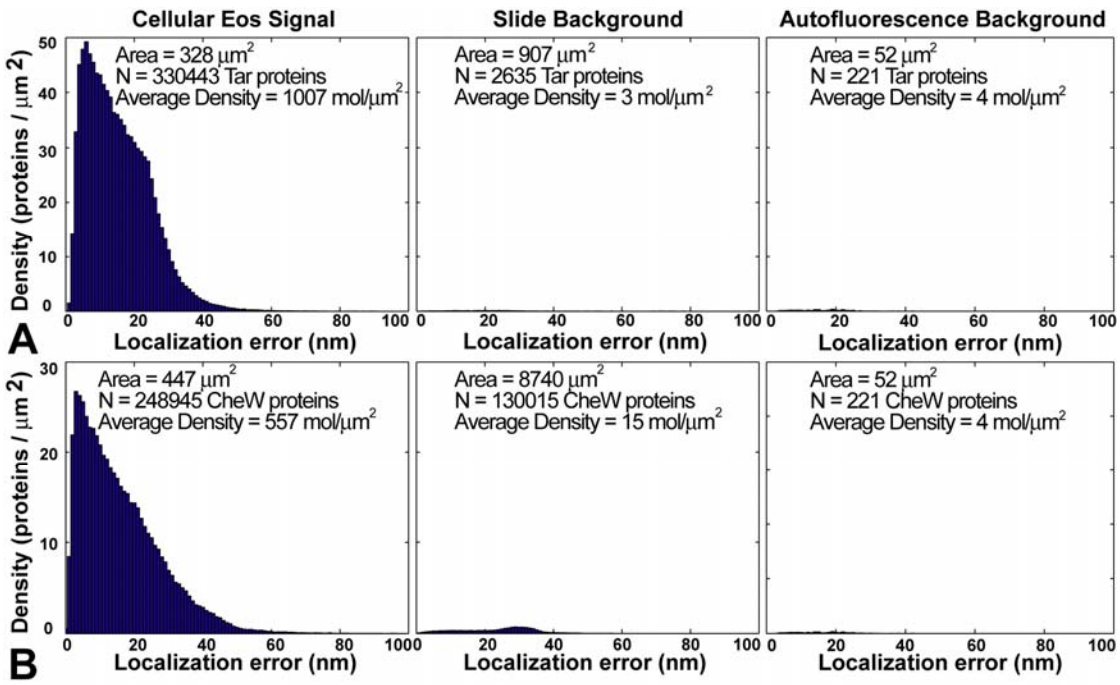

Figure A-2. Signal and background levels for Tar-mEos and tdEos-CheW proteins. **(A)** RP437 Δ*tar* + pALM6001 cells have a high average density of detected Tar-mEos proteins (1007 molecules/μm^2) (left). The number of falsely detected proteins from the media, coverslip or imaging conditions (middle panel) is 0.3% of the signal from the labeled cells. Falsely detected proteins were measured by counting the number of events in regions that do not contain cells. RP437 cells lacking fluorescent proteins were used to determine the number of falsely counted proteins due to cellular autofluorescence (right). The number of falsely detected Tar-mEos was 0.4% of the signal observed (left). **(B)** RP437 Δ*cheW* + pALM5001 also have a high average density of detected tdEos-CheW proteins (557proteins/μm^2) (left). The number of falsely detected CheW proteins from the media, coverslip, or imaging conditions (middle) is 2.6% of the signal from the labeled cells (left). The number of falsely detected CheW proteins due to cellular autofluorescence (right) is 0.7% of the signal observed from labeled cells (left). Background due to cellular autofluorescence or imaging conditions is minimal in comparison to the signal obtained from fluorescently labeled proteins. A threshold of 100 photons and a maximum localization error of 40 nm are used for all images to best discriminate signal from background. These parameters are expected to depend on the fluorescent protein, the type of cells imaged, the background, and whether cells are live or chemically fixed. Note middle and right panels for (A) and (B) show very few events, demonstrating low background.

Appendix III

Resolution Required to Observe Regular Protein Packing within Chemotaxis Clusters

Based on crystal structures of membrane receptors [2] and cryo-electron micrographs of arrays of receptors [3,4], chemotaxis receptors are believed to assemble into tightly packed arrays of trimers of dimers [5] or hedgerows of dimers [2]. To search for repeating arrays of proteins, we first plotted the position of each protein as the center of its 2D Gaussian representation observed in the PALM image. This leads to a representation of the PALM image in which proteins are located at their most likely position (Figure A-3B). We then examined these representations of dense clusters of Tar proteins and visually compared the images with two different models for how chemotaxis receptors arrange in the membrane (trimers of dimers [5] and hedgerow of dimers [3]). In each case, we did not observe any obvious arrays. We then compared radial distribution functions for clusters (example shown in Figure A-3C) to the radial distribution of the ideal trimers of dimers configuration (Figure A-3E top) as well as the ideal hedgerow of dimers arrangement (Figure A-3G top) and found that the peaks of the measured radial distribution functions did not match the peaks of the radial distribution functions for the ideal array in either case. There was considerable variation among the Tar clusters we examined, so we compared many individual cluster radial distribution functions to the two models. We also averaged the radial distribution function from > 100 lateral clusters imaged in TIR illumination to the two models but observed no convincing alignment of peaks.

To determine whether further analysis should be performed, we estimated the resolution required to distinguish between the two models. We performed Monte Carlo simulations in which the positions of proteins in the two models were randomly moved to simulate localization error. We added random offsets to the ideal protein position array for each model by sampling errors from a scaled version of our observed error distribution (see Figure A-1C). The position of the proteins as well as the radial distribution functions for simulations of σ = 1 nm and σ = 2 nm error for each model is shown (Figures A-3D-G). As the error in position of the protein increases, the ideal ordered array becomes difficult to observe. In the trimers of dimers model, σ = 1 nm of error is sufficient to obscure the array and the radial distribution function, such that neither coincides with the ideal model. The hedgerow of dimers model is distinguishable until σ = 3 nm of error in protein position, and has more obvious peaks in the radial distribution that correspond to the ideal model than in the trimers of dimers model. Our mean localization precision of 15 ± 9 nm is larger than our estimate of the required localization precision necessary to distinguish between the two models. With the invention of brighter genetically encoded fluorophores and ultra-low drift microscopes it may be possible to observe regular protein spacing in clusters, especially if clusters contain only one type of receptor.

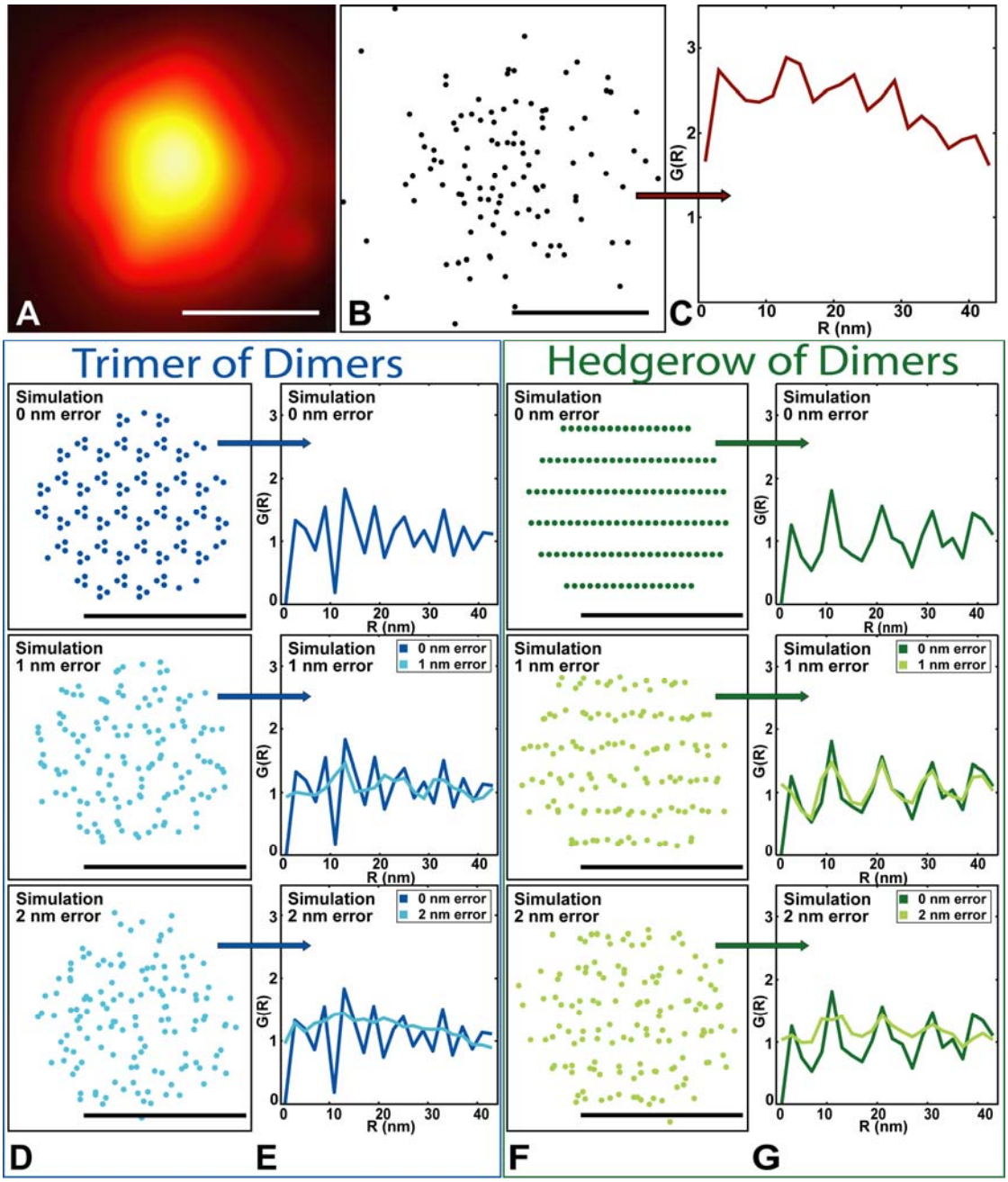
A
B
C
G(R)
R (nm)
Trimer of Dimers
Hedgerow of Dimers
Simulation
0 nm error
1 nm error
2 nm error
0 nm error
1 nm error
2 nm error
D
E
F
G

Figure A-3. Higher localization precision is necessary to observe regular protein packing within clusters. (A) PALM image of chemotaxis cluster (N = 133 Tar proteins). **(B)** Image of cluster in (A) with protein locations represented as single points rather than as Gaussian distributions representing the known error in the localization precision. **(C)** Radial distribution function for image in (B). **(D-G)** Monte Carlo simulations of chemoreceptors in the trimers of dimers (D-E) and hedgerow of dimers (F-G) models. **(D and F)** Top panel shows the locations of receptor dimers (dots) according to each model. When these dimers are convolved with simulated 1 nm and 2 nm errors (middle and bottom left respectively) it becomes increasingly difficult to observe the arrangement of chemoreceptors. Errors are drawn from our observed error distributions of Tar proteins (Appendix IV). **(E and G)** Top panel shows the radial distribution function for each model. Middle and bottom panels show radial distribution functions for the model convolved with 1 and 2 nm errors (colored lines). Note that the distance between Tar receptors in a homodimer (1-2 nm), is on the same order as distance between dimers, therefore we are also unable to detect receptor dimers. All scale bars are 50 nm.

Appendix IV

Quantification of PALM Signal Background

Even a 'bare,' extensively cleaned coverslip will fluoresce. Additional spurious fluorescence is introduced by the cell growth medium. To quantify our general false-positive rate, we subjected the areas between cells to the same analysis we did for the cells themselves. The cell-free regions should not contain any photoactivatable proteins. This false-positive rate was 3-15 events/μm^2.

To determine the additional background from cellular autofluorescence, we counted the number of falsely-detected proteins in cells lacking fluorescent proteins. We find this background to be 4 proteins/μm^2 above the 3-15 events/μm^2.

In cells *with* photoactivatable proteins, such as Tar-mEos and tdEos-CheW, we count hundreds or thousands of proteins per μm^2. By comparing these numbers, we find that our false-positive rate is 0.3-1.5% of the average density of Tar proteins, and 0.6-3% of the average density of CheW proteins per cell (Figure A-2). The background rate is this low because in PALM, non-photoactivatable background is bleached prior to image acquisition.

References for Appendices

1. Shannon CE (1949) Communication in the presence of noise. Proceedings of the Institute of Radio Engineers 37: 10-21.

2. Park S, Borbat P, Gonzalez-Bonet G, Bhatnage J, Pollard A, et al. (2006) Reconstruction of the chemotaxis receptor-kinase assembly. Nature Structural & Molecular Biology 13: 400-407.

3. Weis R, Hirai T, Chalah A, Kessel M, Peters P, et al. (2003) Electron microscopic analysis of membrane assemblies formed by the bacterial chemotaxis receptor Tsr. Journal of Bacteriology 185: 3636-3643.

4. Kim KK, Yokota H, Kim S-H (1999) Four-helical-bundle structure of the cytoplasmic domain of a serine chemotaxis receptor. Nature 400: 787-792.

5. Briegel A, Ding HJ, Li Z, Werner J, Gitai Z, et al. (2008) Location and architecture of the *Caulobacter crescentus* chemoreceptor array. Molecular Microbiology 69: 30-41.